Journal of Computational Physics 230 (2011) 2751–2793

Contents lists available at ScienceDirect

Journal of Computational Physics

journal homepage: www.elsevier.com/locate/jcp

A mass, energy, vorticity, and potential enstrophy conserving lateral boundary scheme for the shallow water equations using piecewise linear boundary approximations

G.S. Ketefian *, M.Z. Jacobson

Department of Civil and Environmental Engineering, Yang and Yamazaki Environment and Energy Building, Stanford University, Stanford, CA 94305-4020, United States

ARTICLE INFO

Article history:
Received 29 July 2010
Accepted 3 November 2010
Available online 24 November 2010

Keywords:
Shaved cell
Shallow water equations
Conservation
Energy
Potential enstrophy
Accuracy

ABSTRACT

A numerical scheme for treating fluid–land boundaries in inviscid shallow water flows is derived that approximates boundary profiles with piecewise linear segments (shaved cells) while conserving the domain-summed mass, energy, vorticity, and potential enstrophy. The new scheme is a generalization of a previous scheme that also conserves these quantities but uses stairsteps to approximate boundary profiles. Numerical simulations are carried out demonstrating the conservation properties and accuracy of the piecewise linear boundary scheme (the PLS) for inviscid flows and comparing its performance with that of the stairstep scheme (the STS). It is found that while both schemes conserve all four domain-summed quantities, the PLS generates depth and velocity fields that are one-half to one order more accurate than those generated by the STS, and it generates vorticity and potential vorticity fields that are at least as accurate as those generated by the STS and often more accurate. The higher accuracy of the PLS is due to its ability to generate smoother flow fields near boundaries of arbitrary shape.

1. Introduction

Quadratically conservative numerical schemes (i.e. schemes that conserve the domain sums of the energy and enstrophy or potential enstrophy) have been shown to be effective in eliminating nonlinear instabilities, controlling the accumulation of truncation errors in the smallest resolved scales, and reducing biases in the flow statistics in long-term simulations. Ketefian and Jacobson [1] (henceforth KJ09) present a brief review of the literature on such schemes. As they point out, one aspect of these schemes that has not been studied in detail is their application to domains with arbitrarily shaped fluid–land boundaries. For this reason, KJ09 developed a boundary scheme for the shallow water equations (SWEs) that conserves the domain-summed mass, energy, vorticity, and potential enstrophy in the presence of arbitrary boundaries. The scheme expands upon that of Arakawa and Lamb [2] (henceforth AL81), which conserves these quantities away from boundaries. Although KJ09 demonstrated that this scheme is an improvement (both in terms of its conservation properties and its accuracy) over several other boundary schemes, it has the disadvantage of using stairsteps to approximate boundary profiles. We consider the stairstep approximation a disadvantage because, as demonstrated in various studies [3–5], it is too crude an approximation of the boundary profile and thus can give rise to inaccurate solutions. In KJ09, this is reflected in the fact that the L_∞ error norms of the fluid depth h and the velocity components u and v fail to converge with decreasing grid size (see

* Corresponding author.
E-mail addresses: gsk@stanford.edu (G.S. Ketefian), jacobson@stanford.edu (M.Z. Jacobson).

0021-9991/$ - see front matter © 2010 Elsevier Inc. All rights reserved.
doi:10.1016/j.jcp.2010.11.008

Table 1 of KJ09 under "BVEM"), indicating that next to boundaries, these quantities are not converging. (Note that the L_∞ error norm of a quantity is equal to the largest absolute error in that quantity throughout the flow domain; see Appendix C.)

In atmosphere and ocean models that use the altitude coordinate (as opposed to the terrain-following σ coordinate) or that do not use unstructured grids, the solution to the stairstep problem has been to use shaved cells or partial steps (the latter being a special case of shaved cells; see, e.g. Fig. 4 of [3]) [3,4,6–8]. (In the literature, the shaved cell method is also referred to as the cut cell method, the embedded boundary method, and the Cartesian grid method; see [9].) Adcroft et al. [3] demonstrated for three test cases (advection of a scalar, large scale flow involving the topographic β effect, and flow over a Gaussian bump) that the shaved cell approximation is more accurate than the partial step approximation, which in turn is more accurate than the stairstep approximation. (Note that the latter is referred to in [3] as the full step approximation.) Similarly, Pacanowski and Gnanadesikan [4] found that their ocean model simulated topographic waves far more accurately with partial steps than with stairsteps, and Lu et al. [5] found partial steps to give a much more accurate solution than stairsteps in a simulation of channel flow with a sloping bottom. Other researchers have come to similar conclusions regarding shaved cells or partial steps and have incorporated them into their models. These include Steppeler et al. [7], Biastoch et al. [10], Skyllingstad and Wijesekera [11], Spall and Pickart [12], Kohl and Stammer [13], Gnanadesikan et al. [14], Menemenlis et al. [15], and Walko and Avissar [8].

Various authors have derived quadratically conservative schemes on non-rectangular and irregular grids (which can potentially be used to approximate boundary profiles more accurately than stairsteps). These include Sadourny et al. [16], Morton and Roe [17], Ringler and Randall [18,19], Bonaventura and Ringler [20], and Sommer and Névir [21]. However, none of these studies explicitly consider fluid–land boundaries. Studies that do consider boundaries include Salmon and Talley [22], Adcroft et al. [3], Perot [23], and Salmon [24,25]. Salmon and Talley [22] extend the mass, energy, vorticity, and enstrophy (but not potential enstrophy) conserving scheme of Arakawa [26] for 2D nondivergent flow to include concave and convex corners and boundaries situated at arbitrary angles. Adcroft et al. [3] use shaved cells to improve the representation of topography in a 3D incompressible ocean model. The finite-volume approach they use conserves mass, momentum, and energy but not vorticity, enstrophy, or potential enstrophy. Perot [23] derives discretizations of both the flux and rotational forms of the incompressible Navier–Stokes equations on unstructured grids and shows results from simulations in a bounded square domain. The discretization of the flux form conserves mass, momentum, and kinetic energy and the one of the rotational form conserves mass, kinetic energy, and vorticity (but neither conserves enstrophy or potential enstrophy). Finally, in [25], Salmon extends his mass, energy, vorticity, and potential enstrophy conserving scheme for the SWEs in unbounded domains [24] to domains with boundaries. He presents simulations of one dimensional (1D) flow in a channel and two dimensional (2D) flows in a square basin. In both cases, the boundaries are aligned with grid lines. No simulations are presented with arbitrarily shaped boundaries that cross the grid lines, but the paper states that "it would be easy in principle to adapt our method to a domain covered by arbitrarily shaped triangles" and points out that the equations for the scheme applied to triangular cells have been derived in part in [24]. One potential drawback of this scheme is the need to solve elliptic equations at each time step.

To improve on the accuracy of the stairstep boundary scheme of KJ09 (henceforth the STS) and to obtain depths and velocities that converge to the exact solution near boundaries, in this paper we use the shaved cell method to better approximate boundary profiles. In particular, we will derive a new scheme that uses piecewise linear line segments to approximate boundaries while maintaining all four conservation properties of the AL81 scheme. We will refer to this new boundary scheme as the piecewise linear scheme (PLS). The PLS is a generalization of the STS obtained by redefining some of the incremental grid distances and areas at and near boundaries in the STS. This generalization is performed in such a way that the conservation proofs in KJ09 for the STS remain valid for the PLS.

This paper is organized as follows. In Section 2, we briefly review the continuous SWEs and their conservation properties. In Section 3, we present the grid layout and variable arrangement used in the PLS, and in Section 4, we present the discrete equations. In Section 5, we discuss the conservation properties of the PLS, and in Section 6, we perform numerical tests to compare the conservation properties of the PLS with those of the STS. These tests indicate that both schemes conserve all four domain-summed quantities equally well. In Section 7, we perform grid refinement studies (GRSs) on a set of ten test cases to compare the accuracy of the PLS with that of the STS. These GRSs indicate that the PLS simulates the depth h and the velocity components u and v more accurately than the STS by 0.5 to 1 order in all test cases, and it simulates the vorticity ζ and potential vorticity q about as accurately as the STS in some cases and more accurately in the remaining cases. Finally, in Section 8, we summarize our results and present our conclusions.

2. Shallow water equations

The SWEs for flow on a flat plane or on the surface of a sphere can be expressed in 2D orthogonal curvilinear coordinates (ξ,η) as follows [27,1]:

$$\frac{\partial}{\partial t}\left(\frac{h}{mn}\right)+\frac{\partial}{\partial \xi}\left(\frac{hu}{n}\right)+\frac{\partial}{\partial \eta}\left(\frac{hv}{m}\right)=0 \tag{1}$$

$$\frac{\partial}{\partial t}\left(\frac{u}{m}\right)-\frac{hv}{m}q=-\frac{\partial}{\partial \xi}(K+\Phi)+\frac{S_\xi}{mh} \tag{2}$$

$$\frac{\partial}{\partial t}\left(\frac{v}{n}\right)+\frac{hu}{n}q=-\frac{\partial}{\partial \eta}(K+\Phi)+\frac{S_\eta}{nh} \tag{3}$$

(1) is the continuity equation, and (2) and (3) are the rotational or vector-invariant forms of the momentum equations [28,23]. h is the depth of the fluid layer, and u and v are the layer-averaged velocity components along curves of constant η and ξ, respectively, on the plane or sphere on which the flow evolves. q, K, and Φ are the potential vorticity, the kinetic energy per unit mass, and the geopotential, respectively, defined as $q = \zeta/h$, $K = (u^2 + v^2)/2$, and $\Phi = g(h + h_{\text{bath}})$. Here, ζ is the absolute vorticity, given by

$$\zeta = f + \zeta_{\text{rel}} \tag{4}$$

where f is the Coriolis parameter and ζ_{rel} is the relative vorticity, defined as

$$\zeta_{\text{rel}} = mn\left[\frac{\partial}{\partial\xi}\left(\frac{v}{n}\right) - \frac{\partial}{\partial\eta}\left(\frac{u}{m}\right)\right] \tag{5}$$

S_ξ and S_η are the ξ and η components of a momentum source (i.e. forcing) vector $\boldsymbol{S}$ and have units of stress. Also, $g = 9.81\ \text{m s}^{-2}$ is the gravitational acceleration, and $h_{\text{bath}}(\xi,\eta)$ is the height of the bathymetry measured from some reference surface. Finally, m and n are the inverse scale factors in the ξ and η directions, respectively. They are defined as follows. For a small change $d\xi$ in the ξ coordinate, m is the ratio of $d\xi$ to the corresponding change in physical distance ds_ξ along a curve of constant η, i.e. $m = d\xi/ds_\xi$. Similarly, $n = d\eta/ds_\eta$, where ds_η is the change in physical distance along a curve of constant ξ corresponding to a change $d\eta$ in the η coordinate. For example, in Cartesian coordinates $(\xi,\eta) = (x,y)$, $m = n = 1$; in cylindrical coordinates $(\xi,\eta) = (r,\theta)$, $m = 1$ and $n = 1/r$; and in spherical coordinates $(\xi,\eta) = (\lambda,\phi)$, $m = 1/(a\cos\phi)$ and $n = 1/a$ (where λ is longitude, ϕ is latitude, and a is the radius of the sphere on which the flow evolves).

We take (1)–(3) to be valid in a domain Ω_f in the $\xi\eta$ plane that is a subset of a rectangular domain Ω bounded by $\xi = \xi_{\min}$, $\xi = \xi_{\max}$, $\eta = \eta_{\min}$, and $\eta = \eta_{\max}$ (Fig. 1). Ω_f is the portion of Ω that consists of fluid (hence the "f" subscript). The rest of Ω consists of land bodies. We assume periodic boundary conditions along the edges of Ω. Thus, in effect, Ω is repeated infinitely many times in the $\xi\eta$ plane in both the ξ and η directions. Since the boundaries of land bodies are rigid walls, the no-flux condition must be enforced at such boundaries.

We can use (1)–(3) to derive the following evolution equations for the energy TE (where the "T" stands for "total", since we are considering the sum of the kinetic and potential energies), vorticity ζ, potential vorticity q, and potential enstrophy $\mathcal{P}$:

$$\frac{\partial}{\partial t}(\text{TE}) + \frac{\partial}{\partial\xi}\left[\frac{hu}{n}(K+\Phi)\right] + \frac{\partial}{\partial\eta}\left[\frac{hv}{m}(K+\Phi)\right] = \frac{1}{mn}(uS_\xi + vS_\eta) \tag{6}$$

$$\frac{\partial}{\partial t}\left(\frac{\zeta}{mn}\right) + \frac{\partial}{\partial\xi}\left(\frac{u}{n}\zeta\right) + \frac{\partial}{\partial\eta}\left(\frac{v}{m}\zeta\right) = \frac{1}{mn}S^{(\zeta)} \tag{7}$$

$$\frac{\partial q}{\partial t} + mu\frac{\partial q}{\partial\xi} + nv\frac{\partial q}{\partial\eta} = \frac{1}{h}S^{(\zeta)} \tag{8}$$

$$\frac{\partial}{\partial t}\left(\frac{\mathcal{P}}{mn}\right) + \frac{\partial}{\partial\xi}\left(\frac{u}{n}\mathcal{P}\right) + \frac{\partial}{\partial\eta}\left(\frac{v}{m}\mathcal{P}\right) = \frac{1}{mn}qS^{(\zeta)} \tag{9}$$

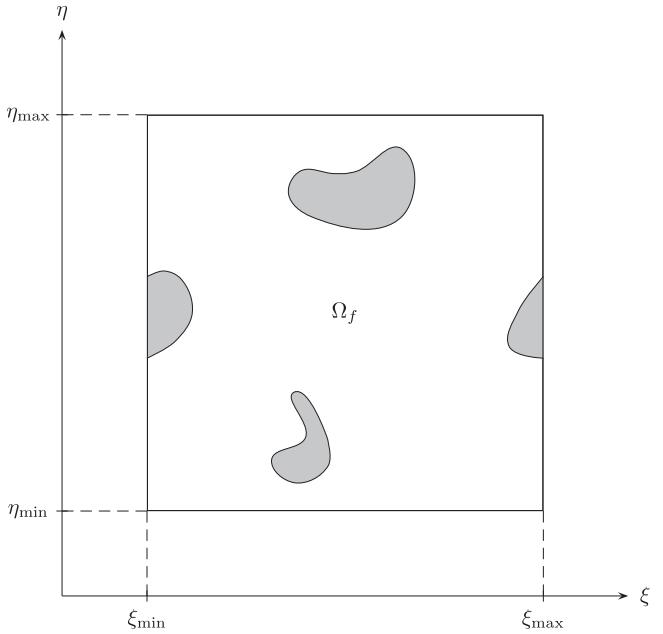

Fig. 1. Rectangular domain Ω in the $\xi\eta$ plane consisting of a fluid portion Ω_f and several land bodies of arbitrary shape. The shaded regions are land and the clear region is fluid. Periodic boundary conditions are assumed along the edges of Ω. The shallow water equations (1)–(3) are valid in Ω_f but not within the land bodies.

Here, TE and $\mathcal{P}$ are given by

$$\mathrm{TE} = \frac{1}{2}\frac{h}{mn}\left[(u^2+v^2) + g(h+2h_{\mathrm{bath}})\right]; \quad \mathcal{P} = \frac{1}{2}\frac{\zeta^2}{h} \tag{10}$$

and the vorticity source term $S^{(\zeta)}$ is given by

$$S^{(\zeta)} = mn\left[\frac{\partial}{\partial\xi}\left(\frac{S_\eta}{nh}\right) - \frac{\partial}{\partial\eta}\left(\frac{S_\xi}{mh}\right)\right] \tag{11}$$

Since the advective terms in (1), (6), (7) and (9) are in flux form, their integrals over Ω_f vanish. This is true whether or not Ω contains land bodies. Thus, in the absence of sources and sinks of momentum (i.e. when $S_\xi = S_\eta = 0$), the SWEs conserve the domain integrals of mass, energy, vorticity, and potential enstrophy.

3. Grid layout and variable arrangement

In this section, we describe the grid layout and the arrangement of the dependent variables on the grid, both for the STS and the PLS.

3.1. Grid layout

We discretize the rectangular region Ω in the $\xi\eta$ plane into I grid boxes in the ξ direction and J grid boxes in the η direction. Each grid box has size $\Delta\xi = (\xi_{\max} - \xi_{\min})/I$ in the ξ direction and size $\Delta\eta = (\eta_{\max} - \eta_{\min})/J$ in the η direction. The grid boxes are centered at coordinates (ξ_i, η_j), where $\xi_i = \xi_{\min} + (i - 1/2)\Delta\xi$ for $i = 1,\ldots,I$ and $\eta_j = \eta_{\min} + (j - 1/2)\Delta\eta$ for $j = 1,\ldots,J$. The eastern/western faces of these grid boxes (i.e. the faces that are parallel to lines of constant ξ) have ξ coordinates $\xi_{i+1/2} = \xi_{\min} + i\Delta\xi$ for $i = 0,\ldots,I$, and the northern/southern faces (i.e. the faces that are parallel to lines of constant η) have η coordinates $\eta_{j+1/2} = \eta_{\min} + j\Delta\eta$ for $j = 0,\ldots,J$. [We refer to the former as eastern/western faces and the latter as northern/southern faces because in the special case of spherical coordinates, $\xi = \lambda$ represents the east–west direction (longitude) and $\eta = \phi$ represents the north–south direction (latitude). This is of course not necessarily the case in other coordinate systems.] We will refer to the lines $\xi = \xi_{i+1/2}$ and $\eta = \eta_{j+1/2}$ in the $\xi\eta$ plane as the grid lines.

3.2. Variable arrangement away from boundaries

Away from fluid–land boundaries, we use the AL81 scheme to discretize the SWEs [2,1]. This scheme uses the staggered Arakawa C-grid. On this grid, h is defined at grid box centers [i.e. at coordinates (ξ_i, η_j)], u is defined at the midpoints of eastern/western box faces [i.e. at $(\xi_{i+1/2}, \eta_j)$], v is defined at the midpoints of northern/southern box faces [i.e. at $(\xi_i, \eta_{j+1/2})$], and ζ is defined at box corners [i.e. at $(\xi_{i+1/2}, \eta_{j+1/2})$].

When Ω contains land bodies, we can use either the stairstep scheme (STS) or the piecewise linear scheme (PLS) to approximate fluid–land boundary profiles. The variable arrangement in the STS is described in detail in KJ09, but for convenient comparison, we briefly summarize it below (Section 3.3). We then give a detailed description of the variable arrangement in the PLS (Section 3.4).

3.3. Variable arrangement in the STS

As described in KJ09, in the STS, a given grid box is assumed to consist either entirely of fluid or entirely of land. If half or more of the area of a grid box in the $\xi\eta$ plane lies in fluid, then, in the model, that box is assumed to consist entirely of fluid. Otherwise, it is assumed to consist entirely of land. This is shown in Fig. 2. We can see from this figure that in the STS, the model fluid–land boundaries always fall on grid box faces. As in the continuous equations, in the STS, the dependent variables h, u, v, and ζ are defined in fluid and at boundaries, but they are undefined in land. Note that in the STS, we do not need to make any modifications to the variable arrangement on the C-grid to account for the presence of land; whether a fluid grid box is far from boundaries or is adjacent to one, h is still defined at the box center, u is still defined at the midpoints of the eastern and western box faces, v is still defined at the midpoints of the northern and southern box faces, and ζ is still defined at the four box corners. We will refer to these locations, respectively, as h-points, u-points, v-points, and ζ-points. Also, we will refer to h-, u-, v-, and ζ-points that lie in fluid as fluid h-, u-, v-, and ζ-points; to h-, u-, v-, and ζ-points that lie in land as land h-, u-, v-, and ζ-points; to u- and v-points that lie on box faces that coincide with the model boundaries as boundary u- and v-points; and to ζ-points that lie at the endpoints of such box faces as boundary ζ-points. To enforce the no-flux condition, we set u and v at boundary u- and v-points to zero, and to obtain ζ at boundary ζ-points in a way that conserves vorticity and potential enstrophy, we solve specially formulated evolution equations for the vorticity [1].

3.4. Variable arrangement in the PLS

In the PLS, the model boundaries consist of the line segments joining the points of intersection of the exact boundary and the grid box faces. This is shown in Fig. 3. We can see from this figure that in the piecewise linear case, the grid contains not

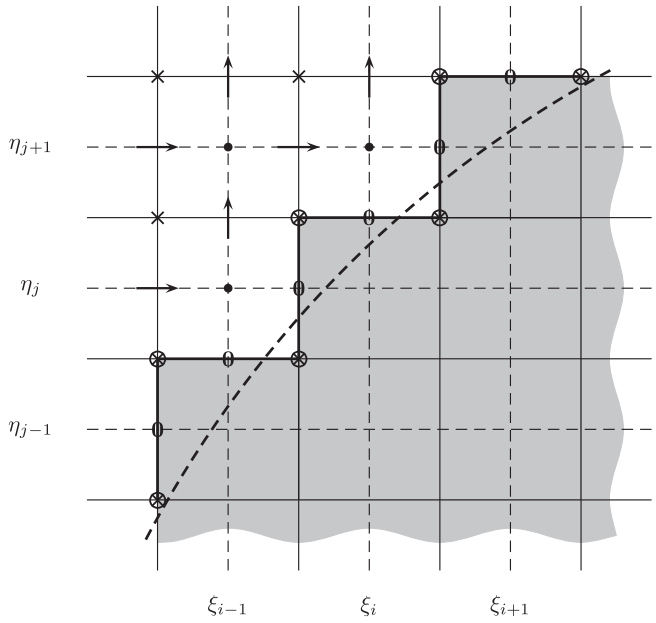

Fig. 2. Computational grid in the $\xi\eta$ plane near a fluid–land boundary showing the distribution of fluid and land grid boxes in the stairstep scheme (STS). The thick dashed curve is the exact boundary, and the set of thick solid line segments is the model boundary. The shaded boxes are land and the clear ones are fluid. The dots denote h-points, the arrows denote u- and v-points, and the "$\times$"s denote ζ-points. "0"s denote boundary u- and v-points. At such points, u and v are set to zero to enforce the no-flux condition. Circled "$\times$"s denote boundary ζ-points, i.e. ζ-points at which an evolution equation is solved to obtain ζ.

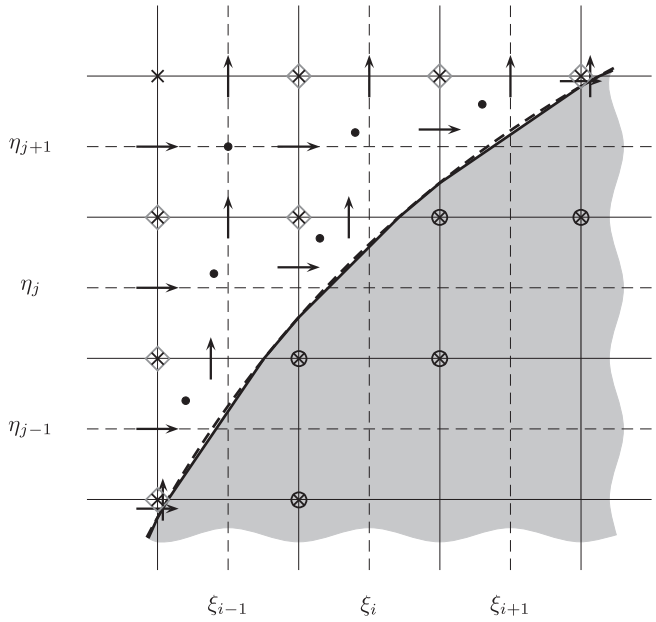

Fig. 3. Computational grid in the $\xi\eta$ plane near a fluid–land boundary showing the distribution of fluid, boundary, and land grid boxes in the piecewise linear scheme (PLS). The thick dashed curve is the exact boundary, and the set of thick solid line segments is the model boundary. The shaded region is land and the clear region is fluid. The dots denote h-points (at the centroids of the fluid portions of fluid and boundary boxes), the arrows denote u- and v-points (at the midpoints of the fluid portions of fluid and partial faces), and the "$\times$"s denote ζ-points. Circled "$\times$"s denote boundary ζ-points (i.e. ζ-points at which an evolution equation is solved to obtain ζ), and "$\times$"s within diamonds denote near-boundary ζ-points [i.e. fluid ζ-points that are surrounded by one or more (but at most four) boundary boxes; see Section 4.4]. Land h-points, land u-points, land v-points, and land ζ-points are not marked because the values of the dependent variables at such points are not physically meaningful.

only boxes that lie completely in fluid or completely in land but also ones that lie partially in fluid and partially in land. We will refer to these three types of boxes as fluid, land, and boundary boxes, respectively. We can also see from the figure that the faces of a boundary box may lie completely in fluid, partially in fluid, or completely in land. A fourth possibility is that a

box face lies exactly on a boundary. (For a boundary of arbitrary shape, this is a rare occurrence in the PLS, but it is always the case in the STS because the stairstep approximation forces boundaries to lie exactly on box faces). We will refer to these four types of faces as fluid, partial, land, and boundary faces, respectively. Similarly, the corners of a boundary box may lie in fluid, exactly on a boundary (which is again rare in the PLS but is always the case at boundaries in the STS; see Fig. 2), or in land. We will refer to these three types of corners as fluid, boundary, and land corners, respectively.

Due to the presence of these various types of boxes, faces, and corners, in the PLS we cannot always define the dependent variables h, u, v, and ζ at the same locations as on the C-grid. We will now present a generalized variable arrangement (GVA) on the grid that takes into account the presence of these various types of boxes, faces, and corners. Fig. 3 shows this GVA near a fluid–land boundary, and Fig. 4 gives a more detailed view of it for a specific boundary grid box. Below, we will consider the arrangement of each variable in the GVA. In doing so, we will require that the GVA reduce to the C-grid variable arrangement (CVA) at fluid boxes, fluid faces, and fluid corners in order that we recover the AL81 scheme away from boundaries.

First, we consider the depth h. Recall that in the CVA, there is a depth associated with each fluid box and that this depth is located at the center of the box. Since the GVA must be identical to the CVA at fluid boxes, in the GVA we now associate a depth with each fluid box and take this depth to be located at the center of the box. Next, we extend this approach to boundary boxes by associating a depth with each such box and taking this depth to be located at the centroid of the fluid portion of the box. [Note that the exact location within the fluid portion of the box where the depth is defined is not used in the PLS; the scheme only needs an h value "associated with" the fluid or boundary box. We use the exact location only for calculating

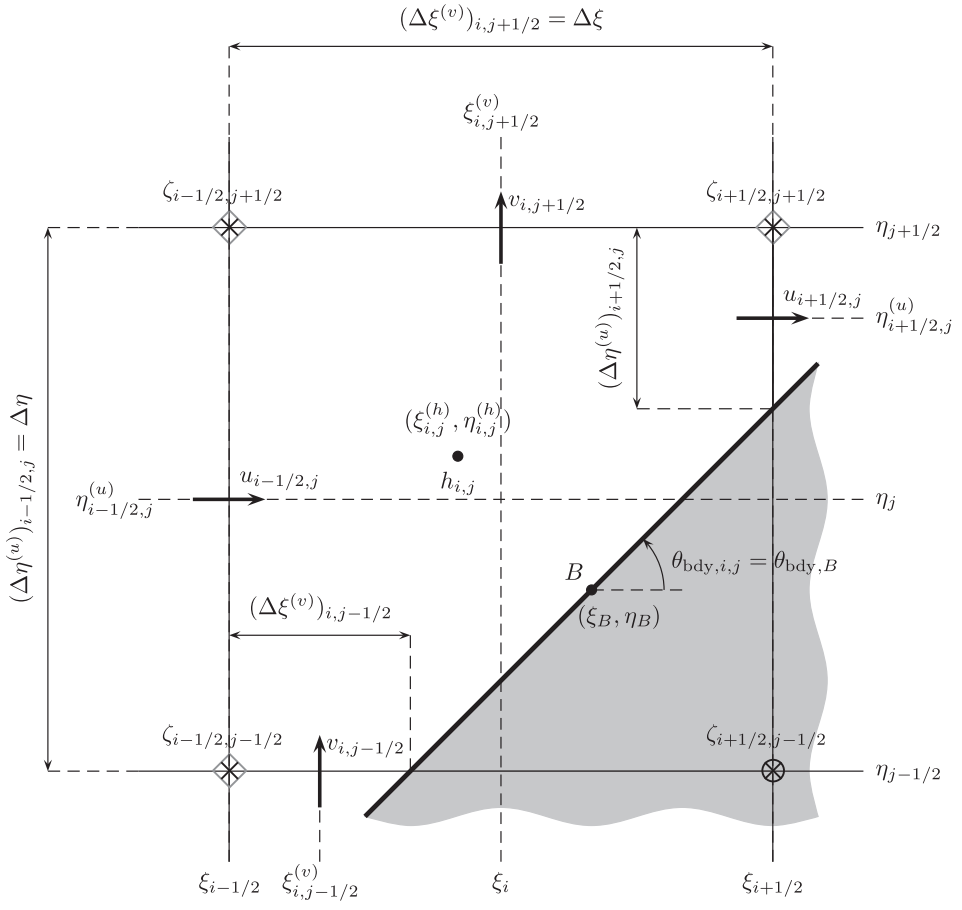

Fig. 4. Detailed view of the generalized variable arrangement (GVA) in the PLS at a boundary grid box in the $\xi\eta$ plane that is intersected on its southern and eastern faces by a fluid–land boundary. The shaded region is land and the clear region is fluid. The thick line denotes the model boundary, and $\theta_{\mathrm{bdy},i,j}$ is the angle in physical space that the boundary makes with a nearby curve of constant η, e.g. the curve on which $\eta = \eta_{j-1/2}$, $\eta = \eta_j$, or $\eta = \eta_{j+1/2}$. Here, $\theta_{\mathrm{bdy},i,j}$ is shown for the special case in which (ξ,η) represents Cartesian coordinates (x,y) and the grid is highly resolved (so that the curvature of the boundary can be ignored). The dot within the fluid portion of the box denotes the location where the depth is defined; the thick arrows on the box faces denote the locations where the velocity components are defined; and the "×"s denote the locations where the vorticities are defined. The circled "×" denotes a boundary ζ-point, and "×"s within diamonds denote near-boundary ζ-points (Section 4.4). Also shown are the sizes in the ξ and η directions of the fluid portions of the box faces, i.e. $(\Delta\xi^{(v)})_{i,j-1/2}$, $(\Delta\xi^{(v)})_{i,j+1/2}$, $(\Delta\eta^{(u)})_{i-1/2,j}$, and $(\Delta\eta^{(u)})_{i+1/2,j}$. Point B on the boundary is used in Appendix A in the derivation of the area $A^{(h)}_{i,j}$ associated with a boundary h-point and in Appendix B in the derivation of the shifted coordinates $\xi^{(v)*}_{i,j+1/2}$ and $\eta^{(u)*}_{i+1/2,j}$. $\theta_{\mathrm{bdy},B}$ is the boundary angle evaluated at point B.

error norms and for generating plots; see Appendix C.] Finally, note that strictly speaking, we should not associate a depth with a land box because in the continuous equations, the dependent variables are not defined within land. Nevertheless, it turns out that we can present the PLS more compactly (i.e. we can avoid the use of conditionals, which makes coding the scheme more straightforward) if we assume that there is a depth associated with each land box. For convenience, we now make this assumption. The exact location and value of this depth are not important, but for completeness, we take it to be located at the center of each land box and set its value to zero. To denote quantities associated with the fluid, boundary, or land grid box centered at (ξ_i, η_j) [or, more briefly, the box at (i,j)], we will use the subscript notation $(\ldots)_{i,j}$. Thus, the depth associated with the box at (i,j) is $h_{i,j}$. We will refer to the locations in fluid, boundary, and land boxes where $h_{i,j}$ is defined as fluid, boundary, and land h-points, respectively, and we will let $(\xi_{i,j}^{(h)}, \eta_{i,j}^{(h)})$ denote their coordinates. In Figs. 3 and 4, fluid and boundary h-points are marked by dots, and land h-points are not marked because the zero depths at such points do not have any physical meaning.

Next, we consider the ξ direction velocity component u. Recall that in the CVA, there is a u value associated with each eastern/western fluid face and that this value is located at the midpoint of the face. As above, for consistency with the CVA, in the GVA we now associate a u value with each eastern/western fluid face and take it to be located at the midpoint of the face. Next, we extend this approach to eastern/western partial faces by associating a u value with each such face and taking this value to be located at the midpoint of the fluid portion of the face. Also, as in the STS, we associate a u value with each eastern/western boundary face, take it to be located at the midpoint of the face, and set it to zero to enforce the no-flux boundary condition. Finally, note that as with the depth at a land box, strictly speaking we should not associate a u value with an eastern/western land face. Nevertheless, in order to present the PLS more compactly, we will associate a zero u value with each such face. As explained in Section 4.1, this value must be zero in order for the no-flux boundary condition to be automatically enforced. The exact location of this zero u value is not important, but for completeness, we will take it to be at the midpoint of each land face. To denote quantities associated with the eastern/western face centered at $(\xi_{i+1/2}, \eta_j)$ [or, more briefly, the face at $(i+1/2,j)$], we will use the subscript notation $(\ldots)_{i+1/2,j}$. Thus, the u value associated with the face at $(i+1/2,j)$ is $u_{i+1/2,j}$. We will refer to the locations on eastern/western fluid and partial faces where $u_{i+1/2,j}$ is defined as fluid u-points, its locations on eastern/western boundary faces as boundary u-points, and its locations on eastern/western land faces as land u-points. In Figs. 3 and 4, fluid u-points are marked by horizontal arrows, and land u-points are not marked because the zero u values at such points do not have any physical meaning. Boundary u-points are not included in the figures because they are rare in the PLS. We will let $\eta_{i+1/2,j}^{(u)}$ denote the η coordinate of the u-point at $(i+1/2,j)$. Thus, u-points are located at coordinates $(\xi_{i+1/2}, \eta_{i+1/2,j}^{(u)})$, where $\eta_{i+1/2,j}^{(u)} = \eta_j$ at eastern/western fluid, boundary, and land faces but not at eastern/western partial faces (Fig. 4).

We now consider the η direction velocity component v. The approach we use for v is analogous to the one above for u. Thus, in the GVA, we associate a v value with each northern/southern face regardless of its type. At a fluid face, we take v to be located at the midpoint of the face; at a partial face, we take it to be located at the midpoint of the fluid portion of the face; at a boundary face, we take it to be located at the midpoint of the face and set it to zero to enforce the no-flux boundary condition; and at a land face, we again take it to be located at the midpoint of the face and set it to zero. As with u at eastern/western land faces, v at northern/southern land faces does not represent a physical quantity; its definition at such faces is merely a convenience. To denote quantities associated with the northern/southern face centered at $(\xi_i, \eta_{j+1/2})$ [or, more briefly, the face at $(i,j+1/2)$], we will use the subscript notation $(\ldots)_{i,j+1/2}$. Thus, the v value associated with the face at $(i,j+1/2)$ is $v_{i,j+1/2}$. The definitions of fluid, boundary, and land v-points are the same as those of fluid, boundary, and land u-points except that they apply to northern/ southern faces instead of eastern/western ones. We will let $\xi_{i,j+1/2}^{(v)}$ denote the ξ coordinate of the v-point at $(i,j+1/2)$. Thus, v-points are located at coordinates $(\xi_{i,j+1/2}^{(v)}, \eta_{j+1/2})$, where $\xi_{i,j+1/2}^{(v)} = \xi_i$ at northern/southern fluid, boundary, and land faces but not at northern/southern partial faces (Fig. 4).

Finally, we consider the vorticity ζ. Recall that in the CVA, there is a vorticity associated with each fluid corner and that this vorticity is located exactly at the corner. For consistency with the CVA, in the GVA we associate a vorticity with each fluid corner and take it to be located exactly at the corner. We also associate a vorticity with each boundary corner (although these are rare in the PLS) and take it to be located exactly at the corner. We now consider land corners. Unlike the case of h at land boxes and u and v at land faces, the vorticity associated with a land corner is not necessarily unphysical. In the GVA, we associate a physically meaningful vorticity with any land corner that has at least one neighboring fluid or boundary grid box, and we take this vorticity to be located exactly at the corner. [This is obviously not the actual location of the vorticity because the actual location cannot be within land; it must be within the fluid or on the fluid–land boundary. Since this actual location (which it turns out we do not need to pinpoint) is within a grid box or two of that point on the exact boundary that is closest to the land corner in consideration, taking the vorticity to be located exactly at the land corner is a first-order approximation (in $\Delta\xi$ and $\Delta\eta$) of its actual location]. On the other hand, we do not associate a vorticity with any land corner at which all four neighboring boxes are land; instead, we leave the vorticity undefined at such a corner. To denote quantities associated with the box corner at $(\xi_{i+1/2}, \eta_{j+1/2})$ [or, more briefly, the corner at $(i+1/2,j+1/2)$], we will use the subscript notation $(\ldots)_{i+1/2,j+1/2}$. Thus, the vorticity associated with the corner at $(i+1/2,j+1/2)$ is $\zeta_{i+1/2,j+1/2}$. We will refer to fluid corners as fluid ζ-points, to boundary corners and to land corners having at least one neighboring fluid or boundary box as boundary ζ-points, and to land corners at which all four neighboring boxes are land as land ζ-points. In Figs. 3 and 4, fluid ζ-points are marked by "×"s and "×"s within diamonds (the latter denoting near-boundary ζ-points; see Section 4.4) while boundary ζ-points are marked by circled "×"s. Land ζ-points are not marked because the vorticity is not defined at such points. Note that since fluid and boundary ζ-points are located exactly at box corners, their coordinates are $(\xi_{i+1/2}, \eta_{j+1/2})$. As described in Section 4,

we will calculate the vorticity at fluid ζ-points diagnostically using the neighboring velocity components, and we will obtain the vorticity at boundary ζ-points prognostically by solving a discrete vorticity evolution equation.

Two quantities that are essential to the PLS are the sizes in the ξ and η directions of the fluid portions of box faces. We will denote the size in the η direction of the fluid portion of any eastern/western face centered at $(\xi_{i+1/2}, \eta_j)$ by $(\Delta\eta^{(u)})_{i+1/2,j}$, and we will denote the size in the ξ direction of the fluid portion of any northern/southern face centered at $(\xi_i, \eta_{j+1/2})$ by $(\Delta\xi^{(v)})_{i,j+1/2}$. These are shown in Fig. 4 for a boundary box that is intersected on its southern and eastern faces by a boundary (with land to the southeast of the boundary). Note that these quantities are defined at all four types of faces (fluid, partial, land, and boundary). At a fluid face, $(\Delta\eta^{(u)})_{i+1/2,j} = \Delta\eta$ or $(\Delta\xi^{(v)})_{i,j+1/2} = \Delta\xi$; at a partial face, $0 < (\Delta\eta^{(u)})_{i+1/2,j} < \Delta\eta$ or $0 < (\Delta\xi^{(v)})_{i,j+1/2} < \Delta\xi$; and at a land or boundary face, $(\Delta\eta^{(u)})_{i+1/2,j} = 0$ or $(\Delta\xi^{(v)})_{i,j+1/2} = 0$.

4. The piecewise linear scheme

In this section, we give a detailed description of the PLS. This consists of the specification of the discrete equations, the various incremental distances and areas appearing in these equations, the procedure used to obtain the vorticity at boundary ζ-points, and the procedure used to evaluate the initial velocity field and the forcing terms in the momentum equations.

4.1. Discrete equations

First, we present the discrete equations used in the PLS. Recall that away from boundaries, these equations reduce to those of the AL81 scheme [2,27].

We begin with the continuity equation (1). This is discretized at fluid and boundary h-points (i,j) as follows:

$$\frac{d}{dt}(\Pi_{i,j}) = -\left[(\delta_\xi F) + (\delta_\eta G)\right]_{i,j} \tag{12}$$

Here, $\delta_\xi(\ldots)$ and $\delta_\eta(\ldots)$ are the differencing operators in the ξ and η directions, respectively [e.g. $(\delta_\xi F)_{i,j} = F_{i+1/2,j} - F_{i-1/2,j}$]. $\Pi_{i,j}$ is the mass (or, equivalently, the volume, since the fluid is assumed to have constant density) in the fluid portion of the box at (i,j), $F_{i-1/2,j}$ and $F_{i+1/2,j}$ are the mass fluxes in the ξ direction through the western and eastern faces of the box, and $G_{i,j-1/2}$ and $G_{i,j+1/2}$ are the mass fluxes in the η direction through the southern and northern faces. $\Pi_{i,j}$ is given by

$$\Pi_{i,j} = (A^{(h)}h)_{i,j} \tag{13}$$

where $A^{(h)}_{i,j}$ is the area associated with the fluid portion of the box. We say "associated with" instead of "of" because it turns out that at a boundary box, $A^{(h)}_{i,j}$ should not be set to the geometric area of the fluid portion (although it does increase and decrease with the geometric area, and it is zero at a land box and is equal to the geometric area at a fluid box). We will present the expression for $A^{(h)}_{i,j}$ later below (Section 4.2). Note that (13) is valid at all three types of boxes (fluid, boundary, and land) because we have defined $h_{i,j}$ at all three types (with $h_{i,j} = 0$ at land boxes) and because the definition of $A^{(h)}_{i,j}$ given below will also apply at all three types. The mass fluxes are given by

$$F_{i+1/2,j} = (\bar{h}^{\xi} u \Delta s^{(u)}_{\eta})_{i+1/2,j} \tag{14}$$

$$G_{i,j+1/2} = (\bar{h}^{\eta} v \Delta s^{(v)}_{\xi})_{i,j+1/2} \tag{15}$$

In these expressions, $\overline{(\ldots)}^{\xi}$ and $\overline{(\ldots)}^{\eta}$ are the arithmetic averaging operators in the ξ and η directions, respectively [e.g. $\bar{h}^{\xi}_{i+1/2,j} = (h_{i+1,j} + h_{i,j})/2$]. In (14), $(\Delta s^{(u)}_{\eta})_{i+1/2,j}$ is the physical distance corresponding to the size $(\Delta\eta^{(u)})_{i+1/2,j}$ of the fluid portion of the eastern/western box face at $(i+1/2,j)$. $(\Delta s^{(v)}_{\xi})_{i,j+1/2}$ in (15) is defined in an analogous way at northern/southern box faces. These distances are given by

$$(\Delta s^{(u)}_{\eta})_{i+1/2,j} = \frac{(\Delta\eta^{(u)})_{i+1/2,j}}{n^{(u)}_{i+1/2,j}} \tag{16}$$

$$(\Delta s^{(v)}_{\xi})_{i,j+1/2} = \frac{(\Delta\xi^{(v)})_{i,j+1/2}}{m^{(v)}_{i,j+1/2}} \tag{17}$$

where $n^{(u)}_{i+1/2,j}$ is the inverse scale factor n evaluated at the u-point at $(i+1/2,j)$, and $m^{(v)}_{i,j+1/2}$ is the inverse scale factor m evaluated at the v-point at $(i,j+1/2)$. (Note that m and n are known functions of ξ and η, and they are defined in fluid, at boundaries, and in land. Thus, they can be evaluated anywhere in the $\xi\eta$ plane as necessary.) Expressions (16) and (17) are valid at all four types of faces (fluid, partial, land, and boundary) because $(\Delta\eta^{(u)})_{i+1/2,j}$ and $(\Delta\xi^{(v)})_{i,j+1/2}$ are each defined at all four types [with $(\Delta s^{(u)}_{\eta})_{i+1/2,j} = 0$ and $(\Delta s^{(v)}_{\xi})_{i,j+1/2} = 0$ at boundary and land faces because $(\Delta\eta^{(u)})_{i+1/2,j} = 0$ and $(\Delta\xi^{(v)})_{i,j+1/2} = 0$ at such faces; see Section 3.4]. This implies that the mass fluxes given by (14) and (15) are also valid at all four types of faces [because we have defined $u_{i+1/2,j}$, $v_{i,j+1/2}$, $(\Delta s^{(u)}_{\eta})_{i+1/2,j}$, and $(\Delta s^{(v)}_{\xi})_{i,j+1/2}$ at all four types and because h is defined at all three types of boxes]. Importantly, (14) and (15) assign a zero mass flux through any land or boundary faces that a boundary box might have because $u_{i+1/2,j}$ and $(\Delta\eta^{(u)})_{i+1/2,j}$ or $v_{i,j+1/2}$ and $(\Delta\xi^{(v)})_{i,j+1/2}$ at such faces are set to zero. This will enforce the

no-flux boundary condition at such boxes (at least as far as the continuity equation is concerned), thereby conserving the domain-summed mass.

Next, we consider the momentum equations (2) and (3). These are discretized at fluid u-points $(i+1/2,j)$ and fluid v-points $(i,j+1/2)$, respectively, as follows:

$$\frac{d}{dt}(u\Delta s_\xi^{(u)*})_{i+1/2,j} = \left[\overline{\overline{G}^\eta \bar{q}^\eta}^\xi + \frac{1}{48}\delta_\xi\left[(\delta_\eta G)(\delta_\xi\delta_\eta q)\right] - \frac{1}{12}\delta_\xi\left[\overline{F}^\xi(\delta_\eta\bar{q}^\xi)\right] - \frac{1}{12}\overline{(\delta_\xi F)(\delta_\eta\bar{q}^\xi)}^\xi - \delta_\xi(K+\Phi)\right]_{i+1/2,j} + \left[\Delta s_\xi^{(u)*}\left(\frac{S_\xi}{h}\right)^*\right]_{i+1/2,j} \tag{18}$$

$$\frac{d}{dt}(v\Delta s_\eta^{(v)*})_{i,j+1/2} = \left[-\overline{\overline{F}^\xi \bar{q}^\xi}^\eta - \frac{1}{48}\delta_\eta[(\delta_\xi F)(\delta_\xi\delta_\eta q)] + \frac{1}{12}\delta_\eta[\overline{G}^\eta(\delta_\xi\bar{q}^\eta)] + \frac{1}{12}\overline{(\delta_\eta G)(\delta_\xi\bar{q}^\eta)}^\eta - \delta_\eta(K+\Phi)\right]_{i,j+1/2} + \left[\Delta s_\eta^{(v)*}\left(\frac{S_\eta}{h}\right)^*\right]_{i,j+1/2} \tag{19}$$

In these equations, $(\Delta s_\xi^{(u)*})_{i+1/2,j}$ and $(\Delta s_\eta^{(v)*})_{i,j+1/2}$ are physical distances along curves of constant η and ξ, respectively, corresponding to (yet to-be-determined) incremental changes in ξ and η. We will derive expressions for these distances in Section 4.4. The kinetic energy per unit mass $K_{i,j}$ and the geopotential $\Phi_{i,j}$ appearing on the right-hand sides (RHSs) of (18) and (19) are given at h-points by

$$K_{i,j} = \begin{cases} \left[\dfrac{1}{A^{(h)}}\dfrac{1}{2}\left(\overline{A^{(u)}u^2}^\xi + \overline{A^{(v)}v^2}^\eta\right)\right]_{i,j} & \text{at fluid and boundary } h\text{-points} \\ \text{undefined} & \text{at land } h\text{-points} \end{cases} \tag{20}$$

$$\Phi_{i,j} = \begin{cases} g(h+h_{\text{bath}})_{i,j} & \text{at fluid and boundary } h\text{-points} \\ \text{undefined} & \text{at land } h\text{-points} \end{cases} \tag{21}$$

$K_{i,j}$ and $\Phi_{i,j}$ will not be needed at land h-points, so we have left their values at such points undefined. In (20), the areas $A_{i+1/2,j}^{(u)}$ and $A_{i,j+1/2}^{(v)}$ are given at all u-points and all v-points, respectively, by

$$A_{i+1/2,j}^{(u)} = [\Delta s_\xi^{(u)*}\Delta s_\eta^{(u)}]_{i+1/2,j} \tag{22}$$

$$A_{i,j+1/2}^{(v)} = [\Delta s_\xi^{(v)}\Delta s_\eta^{(v)*}]_{i,j+1/2} \tag{23}$$

Note that $A_{i+1/2,j}^{(u)}$ and $A_{i,j+1/2}^{(v)}$ are zero at boundary and land u- and v-points because $(\Delta s_\eta^{(u)})_{i+1/2,j}$ and $(\Delta s_\xi^{(v)})_{i,j+1/2}$ are zero at such points. The potential vorticity $q_{i+1/2,j+1/2}$ appearing on the RHSs of (18) and (19) has a physically meaningful value at fluid and boundary ζ-points but not at land ζ-points. Nevertheless, just as with h, u, and v, we will associate a zero q value with land ζ-points in order to be able to express the PLS more compactly. More specifically, doing so will allow us to write just one vorticity evolution equation at boundary ζ-points instead of having various cases as in Appendix A of KJ09. With this in mind, we now define $q_{i+1/2,j+1/2}$ as follows:

$$q_{i+1/2,j+1/2} = \begin{cases} \left(\dfrac{\zeta}{h^{(q)}}\right)_{i+1/2,j+1/2} & \text{at fluid and boundary } \zeta\text{-points} \\ 0 & \text{at land } \zeta\text{-points} \end{cases} \tag{24}$$

The interpolated depth $h_{i+1/2,j+1/2}^{(q)}$ in this expression is given by

$$h_{i+1/2,j+1/2}^{(q)} = \begin{cases} \left(\dfrac{\overline{\Pi}^{\xi\eta}}{A^{(\zeta)}}\right)_{i+1/2,j+1/2} & \text{at fluid and boundary } \zeta\text{-points} \\ \text{undefined} & \text{at land } \zeta\text{-points} \end{cases} \tag{25}$$

where the area $A_{i+1/2,j+1/2}^{(\zeta)}$ associated with ζ-points is given at all such points by

$$A_{i+1/2,j+1/2}^{(\zeta)} = \overline{(A^{(h)})}^{\xi\eta}_{i+1/2,j+1/2} \tag{26}$$

Also, the vorticity $\zeta_{i+1/2,j+1/2}$ in (24) is given by

$$\zeta_{i+1/2,j+1/2} = \begin{cases} (f+\zeta_{\text{rel}})_{i+1/2,j+1/2} & \text{at fluid } \zeta\text{-points} \\ \text{undefined} & \text{at land } \zeta\text{-points} \end{cases} \tag{27}$$

where $f_{i+1/2,j+1/2}$ is the Coriolis parameter (assumed here to be a known function of ξ and η) evaluated at $(\xi_{i+1/2},\eta_{j+1/2})$ and $\zeta_{\text{rel},i+1/2,j+1/2}$ is the relative vorticity. The latter is given by

$$\zeta_{\mathrm{rel},i+1/2,j+1/2} = \begin{cases} \left[\dfrac{1}{A^{(\zeta)}}\left\{\delta_\xi(v\Delta s_\eta^{(v)*}) - \delta_\eta(u\Delta s_\xi^{(u)*})\right\}\right]_{i+1/2,j+1/2} & \text{at fluid } \zeta\text{-points} \\ \text{undefined} & \text{at land } \zeta\text{-points} \end{cases} \tag{28}$$

As discussed in Section 3.4, we have left $\zeta_{i+1/2,j+1/2}$ undefined at land ζ-points. Note that (27) does not specify a way of obtaining the vorticity at boundary ζ-points. At such points, we will solve evolution equations to obtain $\zeta_{i+1/2,j+1/2}$ (Section 4.3). Note also that care must be taken in evaluating the forcing terms $(S_\xi/h)^*_{i+1/2,j+1/2}$ and $(S_\eta/h)^*_{i+1/2,j+1/2}$ on the RHSs of (18) and (19) at u- and v-points that are near boundaries in order to obtain a relative vorticity field that converges to the correct limit as the grid is refined. This issue is discussed in Section 4.4.

4.2. Area $A_{i,j}^{(h)}$ associated with h-points

We now derive expression for the area $A_{i,j}^{(h)}$ associated with each h-point. In order for the PLS to reduce to the AL81 scheme at a fluid h-point, $A_{i,j}^{(h)}$ at such a point must be given by [see Eq. (15) of KJ09]

$$A_{i,j}^{(h)} = \frac{\Delta\xi}{m_{i,j}}\frac{\Delta\eta}{n_{i,j}} \quad \text{at fluid } h\text{-points} \tag{29}$$

where $m_{i,j}$ and $n_{i,j}$ are the inverse scale factors evaluated at the fluid h-point at (i,j) [i.e. at (ξ_i,η_j)]. The RHS of (29) is just an approximation to the geometric area of the fluid box associated with the h-point. The most straightforward generalization of this to a boundary h-point is to set $A_{i,j}^{(h)}$ to the geometric area of the fluid portion of the grid box associated with that boundary h-point. However, we have found that this choice of $A_{i,j}^{(h)}$ gives poor results for the kinetic energy per unit mass $K_{i,j}$ at boundary h-points. This is because in the limit of an infinitely refined grid, the use of such an $A_{i,j}^{(h)}$ in (20) at a boundary h-point does not yield the correct value of K. In Appendix A, we derive the proper expression for $A_{i,j}^{(h)}$ by requiring that (20) give the correct value of K at boundary h-points in the limit of infinite grid resolution. The final result is given in expression (120) of that appendix. Combining (120) with (29) and defining $A_{i,j}^{(h)}$ to be zero at land h-points, we obtain the following general expression for $A_{i,j}^{(h)}$:

$$A_{i,j}^{(h)} = \begin{cases} \dfrac{\Delta\xi}{m_{i,j}}\dfrac{\Delta\eta}{n_{i,j}} & \text{at fluid } h\text{-points} \\ \left[\overline{A^{(u)}}^{\xi}\cos^2\theta_{\mathrm{bdy}} + \overline{A^{(v)}}^{\eta}\sin^2\theta_{\mathrm{bdy}}\right]_{i,j} & \text{at boundary } h\text{-points} \\ 0 & \text{at land } h\text{-points} \end{cases} \tag{30}$$

Here, $\theta_{\mathrm{bdy},i,j}$ is the angle in physical space (as opposed to in the $\xi\eta$ plane) that the boundary line segment in the boundary box at (i,j) makes with a nearby curve of constant η, e.g. the curve on which $\eta = \eta_{j-1/2}$, $\eta = \eta_j$, or $\eta = \eta_{j+1/2}$. In Fig. 4, we show $\theta_{\mathrm{bdy},i,j}$ for the special case in which $(\xi,\eta) = (x,y)$ (so that the $\xi\eta$ plane is identical to the xy plane, which is physical space). In general, however, the angle θ_{bdy} that the boundary makes with a curve of constant η in physical space is not the same as the angle it makes with the horizontal line in the $\xi\eta$ plane corresponding to that curve. For instance, (ξ,η) might represent a stretched Cartesian coordinate system. In such a case, there will be a distortion in the shape of the fluid–land boundary in the process of mapping it from physical space (i.e. the xy plane) to the $\xi\eta$ plane. For the configuration shown in Fig. 4 [and without assuming that $(\xi,\eta) = (x,y)$], $\theta_{\mathrm{bdy},i,j}$ is given by

$$\theta_{\mathrm{bdy},i,j} = \tan^{-1}\left[\frac{\Delta\eta/n_{i+1/2,j} - (\Delta s_\eta^{(u)})_{i+1/2,j}}{\Delta\xi/m_{i,j-1/2} - (\Delta s_\xi^{(v)})_{i,j-1/2}}\right] = \tan^{-1}\left[\frac{\Delta\eta/n_{i+1/2,j} - \Delta\eta^{(u)}_{i+1/2,j}/n^{(u)}_{i+1/2,j}}{\Delta\xi/m_{i,j-1/2} - \Delta\xi^{(v)}_{i,j-1/2}/m^{(v)}_{i,j-1/2}}\right] \tag{31}$$

where $m_{i,j-1/2}$ and $n_{i+1/2,j}$ are the inverse scale factors m and n evaluated at $(\xi_i,\eta_{j-1/2})$ and $(\xi_{i+1/2},\eta_j)$, respectively. The numerator on the RHS of (31) is the distance corresponding to the land portion of the eastern face of the boundary box, and the denominator is the distance corresponding to the land portion of the southern face. For other configurations, e.g. if the boundary segment intersects the southern and northern faces of the box instead of its southern and eastern faces, other expressions must be used to obtain $\theta_{\mathrm{bdy},i,j}$. As with (31), such expressions can be obtained using straightforward geometric arguments.

4.3. Vorticity equation at boundary ζ-points

Next, we outline the procedure used to obtain the vorticity at boundary ζ-points. For this purpose, we need the discrete flux-form vorticity equation at a fluid ζ-point. We can derive this by taking $\delta_\xi(\ldots)$ of (19), subtracting from the result $\delta_\eta(\ldots)$ of (18), and using the definition of ζ given by (27) and (28). This gives

$$\frac{d}{dt}(A^{(\zeta)}\zeta)_{i+1/2,j+1/2} = -\left[(\delta_\xi F^{(\zeta)}) + (\delta_\eta G^{(\zeta)})\right]_{i+1/2,j+1/2} + [A^{(\zeta)}S^{(\zeta)}]_{i+1/2,j+1/2} \tag{32}$$

where we have used the fact that $f_{i+1/2,j+1/2}$ is not a function of time. The vorticity fluxes $F^{(\zeta)}_{i,j+1/2}$ and $G^{(\zeta)}_{i+1/2,j}$ in (32) are given by [see Eqs. (49) and (50) of KJ09]

$$F^{(\zeta)}_{i,j+1/2} = \left[\overline{\overline{F}^{\xi}\bar{q}^{\xi}}^{\eta} - \frac{1}{12}\delta_\eta[\overline{F}^{\xi}(\delta_\eta\bar{q}^{\xi})] - \frac{1}{12}(\delta_\eta\overline{G}^{\eta})(\delta_\xi q)\right]_{i,j+1/2} \tag{33}$$

$$G^{(\zeta)}_{i+1/2,j} = \left[\overline{\overline{G}^{\eta}\bar{q}^{\xi\eta}}^{\xi} - \frac{1}{12}\delta_\xi[\overline{G}^{\eta}(\delta_\xi\bar{q}^{\eta})] - \frac{1}{12}(\delta_\xi\overline{F}^{\xi})(\delta_\eta q)\right]_{i+1/2,j} \tag{34}$$

and the source term $S^{(\zeta)}_{i+1/2,j+1/2}$ is given by

$$S^{(\zeta)}_{i+1/2,j+1/2} = \left[\frac{1}{A^{(\zeta)}}\left[\delta_\xi\left\{\Delta s^{(v)*}_{\eta}\left(\frac{S_\eta}{h}\right)^{*}\right\} - \delta_\eta\left\{\Delta s^{(u)*}_{\xi}\left(\frac{S_\xi}{h}\right)^{*}\right\}\right]\right]_{i+1/2,j+1/2} \tag{35}$$

Note that (35) is a discrete counterpart of (11). Eq. (32) describes the evolution of the average vorticity $\zeta_{i+1/2,j+1/2}$ within the rectangular control volume (CV) of dimensions $\Delta\xi \times \Delta\eta$ centered at the fluid ζ-point at $(i + 1/2, j + 1/2)$ (see Fig. 3 of KJ09). $A^{(\zeta)}_{i+1/2,j+1/2}$ is the physical area associated with this CV and is given by (26).

The procedure we use in the PLS to obtain the vorticity at boundary ζ-points is a generalization of the one presented in KJ09 for the STS. Thus, it is instructive to review the latter before presenting the former. In the STS, we obtain the vorticity at a boundary ζ-point by solving an evolution equation for the vorticity at that point. To derive this equation, we first consider (32) to be the sum of four equations, one for each quarter of the rectangular CV centered at the fluid ζ-point at $(i + 1/2, j + 1/2)$ (see Fig. 5 of KJ09). We will refer to the vorticity equations for the quarters as quarter vorticity equations (QVEs). The QVEs for the northwest (NW), northeast (NE), southwest (SW), and southeast (SE) quarters surrounding a fluid ζ-point are given by

$$\frac{d}{dt}(A^{(\zeta),\mathrm{NW}}\zeta)_{i+1/2,j+1/2} = -\left[(\hat{F}^{(\zeta),\mathrm{N}} - F^{(\zeta),\mathrm{NW}}) + (G^{(\zeta),\mathrm{NW}} - \hat{G}^{(\zeta),\mathrm{W}})\right]_{i+1/2,j+1/2} + [A^{(\zeta),\mathrm{NW}}S^{(\zeta)}]_{i+1/2,j+1/2} \tag{36}$$

$$\frac{d}{dt}(A^{(\zeta),\mathrm{NE}}\zeta)_{i+1/2,j+1/2} = -\left[(F^{(\zeta),\mathrm{NE}} - \hat{F}^{(\zeta),\mathrm{N}}) + (G^{(\zeta),\mathrm{NE}} - \hat{G}^{(\zeta),\mathrm{E}})\right]_{i+1/2,j+1/2} + [A^{(\zeta),\mathrm{NE}}S^{(\zeta)}]_{i+1/2,j+1/2} \tag{37}$$

$$\frac{d}{dt}(A^{(\zeta),\mathrm{SW}}\zeta)_{i+1/2,j+1/2} = -\left[(\hat{F}^{(\zeta),\mathrm{S}} - F^{(\zeta),\mathrm{SW}}) + (\hat{G}^{(\zeta),\mathrm{W}} - G^{(\zeta),\mathrm{SW}})\right]_{i+1/2,j+1/2} + [A^{(\zeta),\mathrm{SW}}S^{(\zeta)}]_{i+1/2,j+1/2} \tag{38}$$

$$\frac{d}{dt}(A^{(\zeta),\mathrm{SE}}\zeta)_{i+1/2,j+1/2} = -\left[(F^{(\zeta),\mathrm{SE}} - \hat{F}^{(\zeta),\mathrm{S}}) + (\hat{G}^{(\zeta),\mathrm{E}} - G^{(\zeta),\mathrm{SE}})\right]_{i+1/2,j+1/2} + [A^{(\zeta),\mathrm{SE}}S^{(\zeta)}]_{i+1/2,j+1/2} \tag{39}$$

Note that the only difference between (36)–(39) and Eqs. (51)–(59) of KJ09 is that the former include source terms while the latter do not. The various areas and vorticity fluxes in (36)–(39) are given by Eqs. (67)–(72) and (A.37)–(A.45) of KJ09, so we do not repeat them here.

Like fluid ζ-points, boundary ζ-points in the STS (e.g. the ones shown in Fig. 2) have CVs associated with them. These consist of the union of those quarters of the rectangle of dimensions $\Delta\xi \times \Delta\eta$ centered at the boundary ζ-point that lie in fluid (see Fig. 4 of KJ09). (Note that in the STS, a quarter is physically either completely in fluid or completely in land because the grid box that it is a part of consists either completely of fluid or completely of land.) The area $A^{(\zeta)}_{i+1/2,j+1/2}$ associated with a boundary ζ-point is the sum of the areas of the fluid quarters around that ζ-point; it is given by one of the 12 expressions in Appendix A of KJ09. Each fluid quarter around a boundary ζ-point has a valid QVE associated with it given by one of (36)–(39). [On the other hand, a land quarter does not have a valid QVE because many or all of the quantities in the vorticity equation for such a quarter are undefined (because they are located within land, and in the STS, physical quantities are left undefined within land; see KJ09).] Thus, a boundary ζ-point can have up to three valid QVEs associated with it, one for each fluid quarter. The overall vorticity equation for the boundary ζ-point is obtained by adding together these valid QVEs. Since in the STS there are 12 possible fluid–land configurations around a boundary ζ-point (see Section 6 of KJ09), the vorticity equation at a boundary ζ-point can be any one of 12 possibilities. These 12 equations can be obtained by adding the source term $[A^{(\zeta)}S^{(\zeta)}]_{i+1/2,j+1/2}$ to the RHSs of the 12 vorticity equations listed in Appendix A of KJ09. For example, we can obtain the vorticity equation at a boundary ζ-point that has fluid to its northwest and land to its northeast, southwest, and southeast by adding $[A^{(\zeta)}S^{(\zeta)}]_{i+1/2,j+1/2}$ to the RHS of Eq. (A.1) of KJ09. This gives

$$\frac{d}{dt}(A^{(\zeta)}\zeta)_{i+1/2,j+1/2} = F^{(\zeta),\mathrm{NW}}_{i+1/2,j+1/2} - G^{(\zeta),\mathrm{NW}}_{i+1/2,j+1/2} + [A^{(\zeta)}S^{(\zeta)}]_{i+1/2,j+1/2} \tag{40}$$

The equations in Appendix A of KJ09 are missing the source terms because in deriving them, it was assumed that there are no forcing terms on the RHSs of the momentum equations.

In the PLS, we use the following generalization of the STS procedure to obtain the vorticity at boundary ζ-points. We again associate a CV with each boundary ζ-point (although we do not specify the exact shape of this CV), and again we solve a flux-form vorticity equation at each such point to obtain the vorticity. To derive the vorticity equation at a boundary ζ-point, as in the STS we consider the fluid–land natures of the quarters of the rectangle of dimensions $\Delta\xi \times \Delta\eta$ centered at the boundary ζ-point. As long as the grid box that a quarter is a part of contains some fluid (i.e. has a positive $A^{(h)}_{i,j}$), the quarter is assigned a fluid area equal to one-fourth the fluid area associated with the box (i.e. $A^{(h)}_{i,j}/4$), and it is assumed to have a valid QVE [which is again one of (36)–(39)]. Note that the quarter itself does not have to physically lie in fluid in order to have a valid QVE. For

example, in Fig. 3, all four quarters of the rectangle of dimensions $\Delta\xi \times \Delta\eta$ centered at the boundary ζ-point at $(i + 1/2, j - 1/2)$ are completely in land, but the northwestern quarter of this rectangle has a valid QVE because the grid box that it is a part of [the one centered at (ξ_i, η_j)] contains some fluid. As in the STS, in the PLS the overall vorticity equation for a boundary ζ-point is given by the sum of the valid QVEs at that ζ-point (of which there can be at most three). Also, as might be expected, the area $A^{(\zeta)}_{i+1/2,j+1/2}$ associated with a boundary ζ-point is given by the sum of the fluid areas of those quarters around that ζ-point that have valid QVEs. This can be seen by expanding the numerical averaging operators on the RHS of (26) and noting that $A^{(h)}_{i,j}$ is zero at land boxes.

Due to the way we have defined $A^{(h)}_{i,j}$, $F_{i+1/2,j}$, $G_{i,j+1/2}$, and $q_{i+1/2,j+1/2}$ (namely, due to the fact that $A^{(h)}_{i,j}$ is zero at land h-points, $F_{i+1/2,j}$ is zero at land u-points, $G_{i,j+1/2}$ is zero at land v-points, and $q_{i+1/2,j+1/2}$ is zero at land ζ-points), we can (and will) use (32) [along with (26), (33) and (34)] as the vorticity equation at any boundary ζ-point. This is because it can be shown that using (26), (32), (33) and (34) along with expressions (30), (14), (15) and (24) for $A^{(h)}_{i,j}$, $F_{i+1/2,j}$, $G_{i,j+1/2}$, and $q_{i+1/2,j+1/2}$ gives the same vorticity equation at a boundary ζ-point as adding together the valid QVEs at that ζ-point (as is done in Appendix A of KJ09). The proof of this consists of substituting the zero values of $A^{(h)}_{i,j}$, $F_{i+1/2,j}$, $G_{i,j+1/2}$, and $q_{i+1/2,j+1/2}$ at land h-, u-, v-, and ζ-points, respectively, into (26), (32), (33) and (34) and comparing the resulting vorticity equation at a boundary ζ-point with the appropriate equation in Appendix A of KJ09. Thus, (32) along with (26), (33) and (34) provide a compact way of presenting (and programming) the various possible vorticity equations at boundary ζ-points.

Finally, we briefly describe the procedure used to evaluate the source term $S^{(\zeta)}_{i+1/2,j+1/2}$ in the boundary vorticity equations, both for the STS and the PLS. Note that we cannot use (35) to calculate $S^{(\zeta)}_{i+1/2,j+1/2}$ at a boundary ζ-point because (35) at such a point involves undefined or unphysical values (e.g. h, S_ξ, and S_η within land). In general, as in KJ09, we can obtain $S^{(\zeta)}_{i+1/2,j+1/2}$ at a boundary ζ-point by fitting polynomial functions of ξ and η to S_η/nh and S_ξ/mh, respectively (using values of S_η/nh and S_ξ/mh from within the fluid near the boundary ζ-point in consideration), taking the analytic derivatives of these polynomial functions with respect to ξ and η, and evaluating the results at the boundary ζ-point. However, if an analytic expression for $S^{(\zeta)}$ as a function of ξ, η, and t is available, it is more convenient to obtain $S^{(\zeta)}_{i+1/2,j+1/2}$ by simply evaluating that expression at the location of the boundary ζ-point. (Such a function must of course be defined in both fluid and land and must be continuous as it crosses the fluid–land boundary.) This is what we do in the numerical tests in Sections 6 and 7.

Recall from Section 3.4 that we have taken boundary ζ-points to be located exactly at grid box corners (and thus within land). Thus, either procedure described above for obtaining $S^{(\zeta)}_{i+1/2,j+1/2}$ at boundary ζ-points requires evaluation of some quantity within land. This is not a problem as long as the boundary ζ-points approach the boundary as the grid is refined (which they will do because they are by definition always within a grid box of the boundary, i.e. they are first-order approximations in $\Delta\xi$ and $\Delta\eta$ of the location of the exact boundary). We have also tried the more complicated approach of locating boundary ζ-points exactly on fluid–land boundaries but have found no significant differences in results.

4.4. Incremental distances $(\Delta s^{(u)*}_\xi)_{i+1/2,j}$ and $(\Delta s^{(v)*}_\eta)_{i,j+1/2}$ and evaluation of initial velocity field and forcing terms

To complete our presentation of the PLS, we now derive expressions for the incremental distances $(\Delta s^{(u)*}_\xi)_{i+1/2,j}$ and $(\Delta s^{(v)*}_\eta)_{i,j+1/2}$ appearing in (18), (19), (22), (23), (28), and (35). This derivation will also yield the procedure for evaluating the initial velocity field and the momentum forcing terms on the RHSs of (18) and (19).

The distances $(\Delta s^{(u)*}_\xi)_{i+1/2,j}$ and $(\Delta s^{(v)*}_\eta)_{i,j+1/2}$ must be defined at all three types of u- and v-points because they appear in expressions (22) and (23) for the areas $A^{(u)}_{i+1/2,j}$ and $A^{(v)}_{i,j+1/2}$, and the latter are needed at all three types of points. First, recall from Section 4.1 that $(\Delta s^{(u)}_\eta)_{i+1/2,j}$ and $(\Delta s^{(v)}_\xi)_{i,j+1/2}$ in (22) and (23) are zero at boundary and land u- and v-points. Thus, it does not matter how $(\Delta s^{(u)*}_\xi)_{i+1/2,j}$ and $(\Delta s^{(v)*}_\eta)_{i,j+1/2}$ are defined at such points (as long as they are not left undefined). For simplicity, we now define $(\Delta s^{(u)*}_\xi)_{i+1/2,j}$ and $(\Delta s^{(v)*}_\eta)_{i,j+1/2}$ at boundary and land u- and v-points to be zero, i.e.

$$(\Delta s^{(u)*}_\xi)_{i+1/2,j} = 0 \quad \text{at boundary and land } u\text{-points} \tag{41}$$

$$(\Delta s^{(v)*}_\eta)_{i,j+1/2} = 0 \quad \text{at boundary and land } v\text{-points} \tag{42}$$

Next, we consider $(\Delta s^{(u)*}_\xi)_{i+1/2,j}$ and $(\Delta s^{(v)*}_\eta)_{i,j+1/2}$ at fluid u- and v-points. In analogy with (16) and (17), we now express these distances at fluid u- and v-points in terms of increments $(\Delta\xi^{(u)*})_{i+1/2,j}$ and $(\Delta\eta^{(v)*})_{i,j+1/2}$ in the ξ and η directions, respectively, i.e.

$$(\Delta s^{(u)*}_\xi)_{i+1/2,j} = \frac{(\Delta\xi^{(u)*})_{i+1/2,j}}{m^{(u)*}_{i+1/2,j}} \quad \text{at fluid } u\text{-points} \tag{43}$$

$$(\Delta s^{(v)*}_\eta)_{i,j+1/2} = \frac{(\Delta\eta^{(v)*})_{i,j+1/2}}{n^{(v)*}_{i,j+1/2}} \quad \text{at fluid } v\text{-points} \tag{44}$$

where $(\Delta\xi^{(u)*})_{i+1/2,j}$ and $(\Delta\eta^{(v)*})_{i,j+1/2}$ are still to be determined. $m^{(u)*}_{i+1/2,j}$ in (43) is the inverse scale factor m associated with the u-point at $(i + 1/2, j)$, and $n^{(v)*}_{i,j+1/2}$ in (44) is the inverse scale factor n associated with the v-point at $(i, j + 1/2)$. (Here, we say "associated with" instead of "evaluated at" because, as described below, it turns out that at u- and v-points that are near

boundaries, $m^{(u)*}_{i+1/2,j}$ and $n^{(v)*}_{i,j+1/2}$ correspond to m and n evaluated not exactly at the u- and v-points but at slightly shifted locations.) To determine $(\Delta\xi^{(u)*})_{i+1/2,j}$ and $(\Delta\eta^{(v)*})_{i,j+1/2}$, first note that in order to recover the AL81 scheme at fluid faces (i.e. away from boundaries), we must have

$$(\Delta\xi^{(u)*})_{i+1/2,j} = \Delta\xi \quad \text{at eastern/western fluid faces} \tag{45}$$

$$(\Delta\eta^{(v)*})_{i,j+1/2} = \Delta\eta \quad \text{at northern/southern fluid faces} \tag{46}$$

This can be seen by comparing the left-hand sides (LHSs) of Eqs. (16) and (17) in KJ09 with the LHSs of Eqs. (18) and (19) and to (43) and (44) here. To determine $(\Delta\xi^{(u)*})_{i+1/2,j}$ and $(\Delta\eta^{(v)*})_{i,j+1/2}$ at partial faces, we impose the constraint that the vorticity source term $S^{(\zeta)}_{i+1/2,j+1/2}$ given by (35) yield the correct value (at fluid ζ-points) in the special case in which m, n, S_ξ/h, and S_η/h are all constants, say m_o, n_o, $(S_\xi/h)_o$, and $(S_\eta/h)_o$. We can see from (11) that in this case, $S^{(\zeta)} = 0$. Substituting (43) and (44) into (35), we obtain

$$S^{(\zeta)}_{i+1/2,j+1/2} = \left[\frac{1}{A^{(\zeta)}}\left[\delta_\xi\left\{\frac{\Delta\eta^{(v)*}}{n^{(v)*}}\left(\frac{S_\eta}{h}\right)^*\right\} - \delta_\eta\left\{\frac{\Delta\xi^{(u)*}}{m^{(u)*}}\left(\frac{S_\xi}{h}\right)^*\right\}\right]\right]_{i+1/2,j+1/2} \tag{47}$$

Setting $m^{(u)*}_{i+1/2,j} = m_o$, $n^{(v)*}_{i,j+1/2} = n_o$, $(S_\xi/h)^*_{i+1/2,j} = (S_\xi/h)_o$, and $(S_\eta/h)^*_{i,j+1/2} = (S_\eta/h)_o$, requiring that $S^{(\zeta)}_{i+1/2,j+1/2}$ equal the exact value of zero, and rearranging terms, we can rewrite (47) as

$$\frac{(S_\eta/h)_o}{n_o} \times \left[\delta_\xi\left(\Delta\eta^{(v)*}\right)\right]_{i+1/2,j+1/2} = \frac{(S_\xi/h)_o}{m_o} \times \left[\delta_\eta\left(\Delta\xi^{(u)*}\right)\right]_{i+1/2,j+1/2} \tag{48}$$

Since m_o, n_o, $(S_\xi/h)_o$, and $(S_\eta/h)_o$ are free to take on any value, (48) can hold only if

$$\left[\delta_\xi\left(\Delta\eta^{(v)*}\right)\right]_{i+1/2,j+1/2} = 0 \tag{49}$$

and

$$\left[\delta_\eta\left(\Delta\xi^{(u)*}\right)\right]_{i+1/2,j+1/2} = 0 \tag{50}$$

(49) implies that $(\Delta\eta^{(v)*})_{i,j+1/2}$ must be the same at two neighboring fluid v-points along a line of constant η regardless of whether the northern/southern faces on which these v-points are located are fluid or partial faces. Since we know from (46) that $(\Delta\eta^{(v)*})_{i,j+1/2}$ equals $\Delta\eta$ at a northern/southern fluid face, it must also equal $\Delta\eta$ at a northern/southern partial face. Thus, we have

$$(\Delta\eta^{(v)*})_{i,j+1/2} = \Delta\eta \quad \text{at fluid } v\text{-points (i.e. at both fluid and partial northern/southern faces)} \tag{51}$$

Similarly, (45) and (50) imply

$$(\Delta\xi^{(u)*})_{i+1/2,j} = \Delta\xi \quad \text{at fluid } u\text{-points (i.e. at both fluid and partial eastern/western faces)} \tag{52}$$

Substituting these into (43) and (44) and combining the results with (41) and (42), we obtain

$$(\Delta s^{(u)*}_\xi)_{i+1/2,j} = \begin{cases} \dfrac{\Delta\xi}{m^{(u)*}_{i+1/2,j}} & \text{at fluid } u\text{-points} \\ 0 & \text{at boundary and land } u\text{-points} \end{cases} \tag{53}$$

$$(\Delta s^{(v)*}_\eta)_{i,j+1/2} = \begin{cases} \dfrac{\Delta\eta}{n^{(v)*}_{i,j+1/2}} & \text{at fluid } v\text{-points} \\ 0 & \text{at boundary and land } v\text{-points} \end{cases} \tag{54}$$

In Cartesian coordinates $(\xi,\eta) = (x,y)$, we have $\Delta\xi = \Delta x$, $\Delta\eta = \Delta y$, and $m^{(u)*}_{i+1/2,j} = n^{(v)*}_{i,j+1/2} = 1$ (because m and n have the uniform value of 1 regardless of where they are evaluated). Thus, for the special case of Cartesian coordinates, (53) and (54) reduce to

$$(\Delta s^{(u)*}_\xi)_{i+1/2,j} = \begin{cases} \Delta x & \text{at fluid } u\text{-points} \\ 0 & \text{at boundary and land } u\text{-points} \end{cases} \tag{55}$$

$$(\Delta s^{(v)*}_\eta)_{i,j+1/2} = \begin{cases} \Delta y & \text{at fluid } v\text{-points} \\ 0 & \text{at boundary and land } v\text{-points} \end{cases} \tag{56}$$

What remains now is to determine $m^{(u)*}_{i+1/2,j}$ and $n^{(v)*}_{i,j+1/2}$ at fluid u- and v-points for the general case of orthogonal curvilinear coordinates (ξ,η). We will determine these along with the forcing terms $(S_\xi/h)^*_{i+1/2,j}$ and $(S_\eta/h)^*_{i,j+1/2}$ by requiring that in the limit of an infinitely refined grid, the vorticity source term $S^{(\zeta)}_{i+1/2,j+1/2}$ given by (35) approach the correct limit. In Appendix B, we show that if we simply evaluate $[\Delta s^{(u)*}_\xi (S_\xi/h)^*]_{i+1/2,j}$ and $[\Delta s^{(v)*}_\eta (S_\eta/h)^*]_{i,j+1/2}$ at near-boundary u- and v-points exactly where

u and v are defined at such points [i.e. at the coordinates $(\xi_{i+1/2}, \eta^{(u)}_{i+1/2,j})$ and $(\xi^{(v)}_{i,j+1/2}, \eta_{j+1/2})$, respectively], then $S^{(\zeta)}_{i+1/2,j+1/2}$ at near-boundary ζ-points will not converge to the correct value as the grid is refined. Here, we define near-boundary u- and v-points as those fluid u- and v-points that are surrounded by one or (at most) two boundary boxes, and we define near-boundary ζ-points as those fluid ζ-points that are surrounded by one or more (but at most four) boundary boxes. In Figs. 3 and 4, such ζ-points are denoted by "×"s within diamonds. We also show in Appendix B that in order to allow $S^{(\zeta)}_{i+1/2,j+1/2}$ at near-boundary ζ-points to converge to the correct limit, the forcing terms $[\Delta s^{(u)*}_{\xi}(S_\xi/h)^*]_{i+1/2,j}$ and $[\Delta s^{(v)*}_{\eta}(S_\eta/h)^*]_{i,j+1/2}$ in the momentum equations (18) and (19) at near-boundary u- and v-points must be evaluated at the shifted locations $(\xi_{i+1/2}, \eta^{(u)*}_{i+1/2,j})$ and $(\xi^{(v)*}_{i,j+1/2}, \eta_{j+1/2})$, respectively, instead of exactly at the u- and v-points [which are at $(\xi_{i+1/2}, \eta^{(u)}_{i+1/2,j})$ and $(\xi^{(v)}_{i,j+1/2}, \eta_{j+1/2})$]. This implies that $m^{(u)*}_{i+1/2,j}$, $n^{(v)*}_{i,j+1/2}$, $(S_\xi/h)^*_{i+1/2,j}$, and $(S_\eta/h)^*_{i,j+1/2}$ must be obtained by evaluating m, n, S_ξ/h, and S_η/h at the shifted locations. [Recall from (53) and (54) that $(\Delta s^{(u)*}_{\xi})_{i+1/2,j}$ and $(\Delta s^{(v)*}_{\eta})_{i,j+1/2}$ are defined in terms of $m^{(u)*}_{i+1/2,j}$ and $n^{(v)*}_{i,j+1/2}$, so the latter must be evaluated at the same locations as the former.] The procedure for determining the coordinates $\xi^{(v)*}_{i,j+1/2}$ and $\eta^{(u)*}_{i+1/2,j}$ is presented in Appendix B. As an example, we show in Fig. 12 the shifted locations $(\xi_{i+1/2}, \eta^{(u)*}_{i+1/2,j})$ and $(\xi^{(v)*}_{i,j+1/2}, \eta_{j+1/2})$ along with the locations of u- and v-points near a portion of the inner boundary of the northeastern quarter of the annulus used in some of the accuracy tests in Section 7. Note that away from boundaries (i.e. at non-near-boundary u- and v-points), $\xi^{(v)*}_{i,j+1/2} = \xi^{(v)}_{i,j+1/2} = \xi_i$ and $\eta^{(u)*}_{i+1/2,j} = \eta^{(u)}_{i+1/2,j} = \eta_j$.

Finally, note that expression (28) for the relative vorticity $\zeta_{\mathrm{rel},i+1/2,j+1/2}$ has the same form as expression (35) for the vorticity source term $S^{(\zeta)}_{i+1/2,j+1/2}$; we can obtain one from the other by replacing u and v with $(S_\xi/h)^*$ and $(S_\eta/h)^*$ or vice versa. Thus, to ensure that the initial relative vorticity field converges at near-boundary ζ-points as the grid is refined, we must evaluate the initial velocity components at near-boundary u- and v-points at the shifted locations instead of where u and v are defined. [We cannot do this at later times because in calculating $\zeta_{\mathrm{rel},i+1/2,j+1/2}$ using (28), we must use whatever values the model has generated for $u_{i+1/2,j}$, $u_{i+1/2,j+1}$, $v_{i,j+1/2}$, and $v_{i+1,j+1/2}$.] In Section 7, we demonstrate that evaluating the initial velocity components and the forcing terms at the shifted locations improves the accuracy of the model by allowing the (relative) vorticity to converge to the correct limit at near-boundary ζ-points.

5. Proofs of conservation properties

We have generalized the PLS from the STS in such a way that the conservation proofs presented in KJ09 for the STS still hold for the PLS. As a result, like the STS, the PLS conserves (as a function of time) the domain-summed mass $\mathrm{MASS_{tot}}$ and vorticity $\mathrm{VORT_{tot}}$ to within roundoff error, and it conserves the domain- summed total energy $\mathrm{TE_{tot}}$ (sum of the kinetic and potential energies) and potential enstrophy $\mathrm{PENST_{tot}}$ to within time integration errors. These quantities are defined as follows:

$$\mathrm{MASS_{tot}} = \sum_{\substack{\text{fld. \& bdy.}\\ h\text{-points}}} \Pi_{i,j} \tag{57}$$

$$\mathrm{TE_{tot}} = \sum_{\substack{\text{fld. \& bdy.}\\ h\text{-points}}} \frac{1}{2}\left[\overline{A^{(u)}u^2\bar{h}^{\xi}}^{\xi} + \overline{A^{(v)}v^2\bar{h}^{\eta}}^{\eta} + g\Pi(h+2h_{\mathrm{bath}})\right]_{i,j} \tag{58}$$

$$\mathrm{VORT_{tot}} = \sum_{\substack{\text{fld. \& bdy.}\\ \zeta\text{-points}}} (A^{(\zeta)}\zeta)_{i+1/2,j+1/2} \tag{59}$$

$$\mathrm{PENST_{tot}} = \sum_{\substack{\text{fld. \& bdy.}\\ \zeta\text{-points}}} \left[A^{(\zeta)}\frac{1}{2}\frac{\zeta^2}{h^{(q)}}\right]_{i+1/2,j+1/2} \tag{60}$$

$\mathrm{MASS_{tot}}$ is conserved because the discrete continuity equation (12) is in flux form and the no-flux condition is enforced at boundary and land faces of boundary boxes. The conservation of the remaining three quantities can be proven using procedures identical to the ones used in KJ09 for the STS. This is because the only differences between the STS and PLS are in the choices of the area $A^{(h)}_{i,j}$ and the distances $(\Delta s^{(u)*}_{\xi})_{i+1/2,j}$, $(\Delta s^{(u)}_{\eta})_{i+1/2,j}$, $(\Delta s^{(v)}_{\xi})_{i,j+1/2}$, and $(\Delta s^{(v)*}_{\eta})_{i,j+1/2}$. [The STS uses $A^{(h)}_{i,j} = \Delta\xi\Delta\eta/(mn)_{i,j}$, $(\Delta s^{(u)*}_{\xi})_{i+1/2,j} = \Delta\xi/m_{i+1/2,j}$, $(\Delta s^{(u)}_{\eta})_{i+1/2,j} = \Delta\eta/n_{i+1/2,j}$, $(\Delta s^{(v)}_{\xi})_{i,j+1/2} = \Delta\xi/m_{i,j+1/2}$, and $(\Delta s^{(v)*}_{\eta})_{i,j+1/2} = \Delta\eta/n_{i,j+1/2}$. In these, $m_{i,j}$ and $n_{i,j}$ are obtained by evaluating m and n at h-points (ξ_i, η_j); $m_{i+1/2,j}$ and $n_{i+1/2,j}$ are obtained by evaluating m and n at u-points $(\xi_{i+1/2}, \eta_j)$; and $m_{i,j+1/2}$ and $n_{i,j+1/2}$ are obtained by evaluating m and n at v-points $(\xi_i, \eta_{j+1/2})$.] The conservation proofs in KJ09 do not depend on how these quantities are defined. In this paper, we have taken advantage of this fact to derive a more accurate scheme. In Section 6, we demonstrate these conservation properties via numerical simulations.

6. Conservation tests

To demonstrate the conservation properties of the PLS and compare them with those of the STS, we begin by performing two simulations, one with each scheme, of advection of a vortex around an elliptic island. We set up the simulations as follows. We use Cartesian coordinates $(\xi,\eta) = (x,y)$ and a square domain that extends from -10 km to 10 km in both directions. We assume periodic boundary conditions along the edges of this domain and embed in it an elliptic island (Fig. 5). Since bathymetric effects are not the focus of this paper, for simplicity we set the bathymetry $h_{\text{bath}}(x,y)$ to zero. Also, we neglect rotation for now by setting $f = 0$. (We will consider the case with rotation later below.) We use a uniform grid with $I \times J = 40 \times 40$ points, so the grid sizes are $\Delta x = \Delta y = 500$ m. We initialize the flow with a rotating core of positive vorticity centered at $(x,y) = (-10\text{ km}, 0\text{ km})$ [Fig. 5, panels (a) and (b)]. The expressions for the initial h, u, and v fields are given by expressions (90)–(92) of KJ09, so we do not repeat them here. Also, the easterly forcing used to advect the vortex is given by expression (93) of KJ09 but with the constant $3.5 \times 10^{-3}\ \text{m}^2\ \text{s}^{-2}$ therein replaced with $10^{-3}\ \text{m}^2\ \text{s}^{-2}$. We integrate both simulations to $t = 10^6$ s ≈ 11.6 d using the fourth-order Runge–Kutta (RK4) method and a time step of $\Delta t = 5$ s. The initial and final vorticity fields for each scheme are shown in Fig. 5.

We find that both the STS and the PLS conserve MASS_{tot} and VORT_{tot} to within roundoff error. Also, both schemes conserve TE_{tot} after about $t = 10{,}000$ s, which is when the forcing shuts off. (Note that the forcing adds energy to this flow between 5000 s and 10,000 s. Thus, energy is conserved only after about 10,000 s; see Section 8.1 of KJ09.) Finally, as expected, both schemes conserve $\text{PENST}_{\text{tot}}$ to within time integration errors. The initial value of $\text{PENST}_{\text{tot}}$ for both schemes is $0.123\ \text{m}\ \text{s}^{-2}$; the deviation from this value by the end of the simulation is $1.19 \times 10^{-11}\ \text{m}\ \text{s}^{-2}$ for the STS and $1.05 \times 10^{-11}\ \text{m}\ \text{s}^{-2}$ for the PLS. We know that these deviations are due to time integration errors because they decrease with decreasing Δt. For

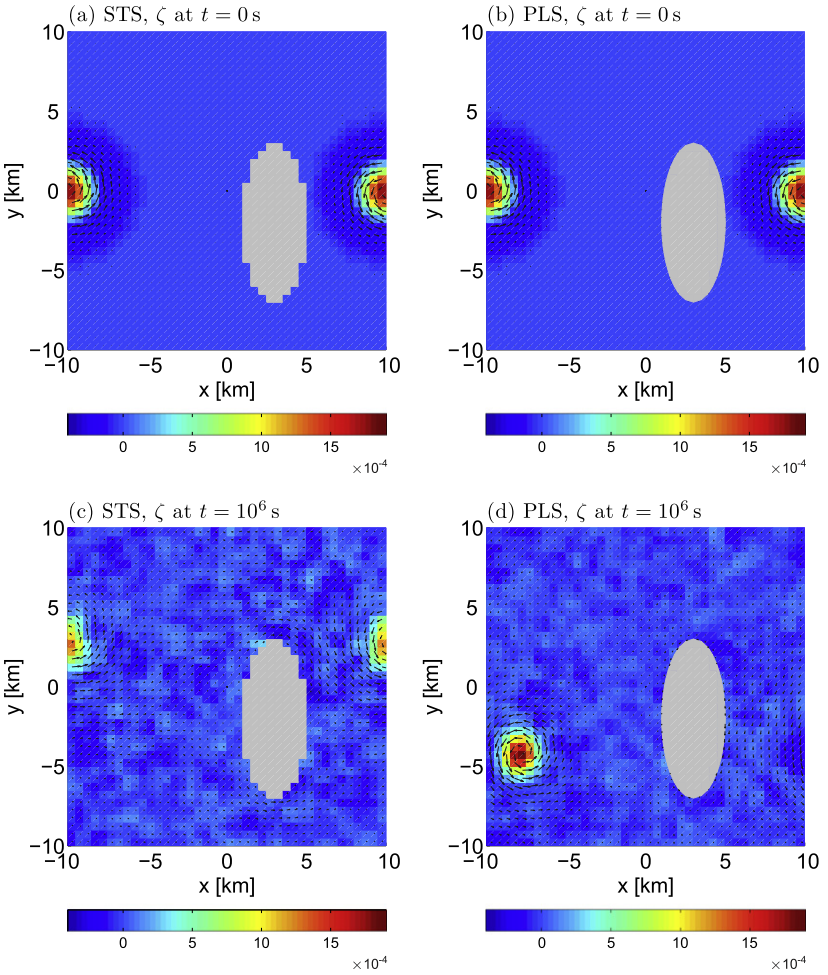

Fig. 5. Vorticity ζ (in s^{-1}) and velocities at $t = 0$ s and $t = 10^6$ s ≈ 11.6 d from simulations of advection of a vortex around an elliptic island performed on a $\Delta x = \Delta y = 500$ m grid. Panels (a) and (c) show results from the STS, and panels (b) and (d) show results from the PLS. Both simulations are without rotation ($f = 0$). The maximum velocity magnitude is 0.85 m s^{-1} in (a), (b), and (d) and 0.67 m s^{-1} in (c). All four plots use the same vector length scale for the velocity and the same color scale for the vorticity. For plotting purposes, u, v, and ζ have been interpolated from u-, v-, and ζ-points to h-points (Appendix C).

example, with a Δt of 2.5 s, we obtain a deviation in $\text{PENST}_{\text{tot}}$ of 3.90×10^{-13} m s^{-2} for the STS and 3.40×10^{-13} m s^{-2} for the PLS. For both schemes, these values correspond to a factor of about $32 = 2^5$ reduction in the $\text{PENST}_{\text{tot}}$ deviation. Thus, the time integration errors seem to be behaving as $o(\Delta t^5)$. This is faster than the $o(\Delta t^4)$ behavior one might expect from RK4, but in any case it indicates that the errors in $\text{PENST}_{\text{tot}}$ are due to the time integration.

To demonstrate that the conservation properties still hold when rotation is present, we have rerun the four simulations above (STS and PLS with $\Delta t = 5$ s and 2.5 s) with $f = 10^{-4}$ s^{-1}. The final velocity and vorticity fields are of course different than the ones without rotation because the inertial rotations of the velocity vectors change the path of the vortex, but our conclusions about the conservation properties are identical, i.e. in both schemes, MASS_{tot} and VORT_{tot} are conserved to within roundoff error, and TE_{tot} and $\text{PENST}_{\text{tot}}$ are conserved to within time integration errors.

7. Accuracy tests

As in KJ09, in this paper we determine the accuracies of the STS and PLS by performing grid refinement studies (GRSs). Performing a GRS entails simulating the same flow configuration on a set of successively finer grids, calculating various norms of the errors in the dependent variables h, u, v, and ζ (or any other quantity of interest that depends on these variables such as the potential vorticity $q = \zeta/h$), and observing the behaviors of these error norms with decreasing grid size. The error norms we calculate are the L_1, L_2, and L_∞ norms of the absolute error $|\Delta\phi|$ in some quantity ϕ (where ϕ can be h, u, v, ζ, q, etc.). We denote these error norms by $\|\Delta\phi\|_1$, $\|\Delta\phi\|_2$, and $\|\Delta\phi\|_\infty$, respectively. The definitions of these norms and the methods used to calculate them are given in Appendix C. The rates at which the error norms converge to zero as the grid is refined determine the accuracy of the scheme; the larger the rates are for a given dependent variable, the more accurately the scheme simulates that variable.

In addition to the STS and PLS, we perform GRSs with a version of the piecewise linear scheme in which the initial velocity field and/or the forcing terms at near-boundary u- and v-points are not evaluated at the shifted locations but at the locations where u and v are defined. We refer to this version of the piecewise linear scheme as the UNPLS (where the "UN" is for "unshifted"). By comparing the accuracy results of the UNPLS with those of the PLS, we will be able to demonstrate that the use of the shifted locations in the PLS indeed improves the accuracy of the model.

Although the prognostic variables in the boundary schemes are h, u, and v within the fluid and ζ at boundaries, in the tests in this section we also consider how accurately the schemes simulate the potential vorticity q. This is because an important feature of the SWEs is the conservation of potential vorticity q following a fluid particle (in the absence of sources and sinks). (Note that here, we mean conservation in a different sense than the conservation of domain-integrated quantities discussed in Section 2.) Eq. (8) states this mathematically since its LHS is the material derivative of q (i.e. Dq/Dt). From (8), we see that when $S^{(\zeta)} = 0$, q is simply advected by the flow. Thus, when $S^{(\zeta)}$ is zero, a numerical scheme for the SWEs should accurately advect q. Of course, when $S^{(\zeta)}$ is not zero, q is not conserved following a fluid particle, but a robust scheme should be able to simulate q accurately in this case as well. In the tests in this section, we check for this by observing the convergence rates of the L_1, L_2, and L_∞ error norms of q.

We perform the GRSs on ten test cases (TCs) of shallow water flow. Table 1 summarizes various aspects of these TCs. The first six TCs are 1D channel flows for which analytic solutions are available, and the last four are 2D flows in an annulus for which there are no analytic solutions. Note that in the channel flow TCs, we orient the channel at an angle to the grid. Thus, the flow generated by the model is 2D. Also, in the annulus flow TCs, we obtain the "exact" solutions by performing highly resolved simulations in cylindrical coordinates $(\xi, \eta) = (r, \theta)$ (Section 7.2). For most of the TCs, we perform three GRSs (one with the STS, a second with the PLS, and a third with the UNPLS), but for TCs 7, 8, and 9 we perform only two because

Table 1
Test cases (TCs) used to determine the accuracies of the stairstep (STS), piecewise linear (PLS), and unshifted piecewise linear (UNPLS) schemes. For each TC, the table specifies the flow geometry, whether or not there is external forcing, the value of the Coriolis parameter f, whether or not an analytic solution is available, and the initial conditions.

TC #	Geometry	Forcing?	Coriolis param. f	Analytic solution?	Initial conditions
1	Channel at 30° to x axis	No	0	Yes	Time-independent solution given by Eqs. (61)–(63) (h uniform at 5 m; u and v spatially variable)
2	Channel at 30° to x axis	Yes	0	Yes	Eqs. (70) and (71) (h uniform at 5 m; $u = v = 0$)
3	Channel at 30° to x axis	No	10^{-2} s^{-1}	Yes	Time-independent solution given by Eqs. (73)–(75) (h, u, and v all spatially variable)
4	Channel at 10° to x axis	No	0	Yes	Time-independent solution given by Eqs. (61)–(63) (h uniform at 5 m; u and v spatially variable)
5	Channel at 10° to x axis	Yes	0	Yes	Eqs. (70) and (71) (h uniform at 5 m; $u = v = 0$)
6	Channel at 10° to x axis	No	10^{-1} s^{-1}	Yes	Time-independent solution given by Eqs. (73)–(75) (h, u, and v all spatially variable)
7	Annulus	No	0	No	Gaussian hill of h given by Eq. (76) with $h_{\text{peak}} = 0.1$ m; $u = v = 0$
8	Annulus	No	10^{-3} s^{-1}	No	Gaussian hill of h given by Eq. (76) with $h_{\text{peak}} = 0.05$ m; $u = v = 0$
9	Annulus	No	10^{-3} s^{-1}	No	Gaussian hill of h given by Eq. (76) with $h_{\text{peak}} = 0.05$ m; u and v given by Eqs. (79)–(84)
10	Annulus	Yes	0	No	h uniform at 5 m; $u = v = 0$

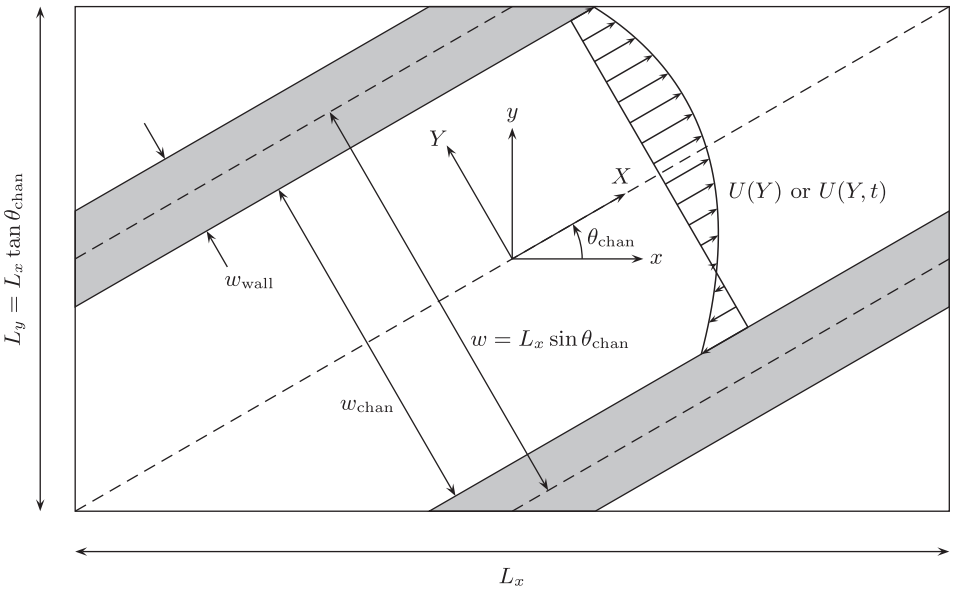

Fig. 6. Orientation of the channel in the model domain in the xy plane. The shaded regions are land (the channel walls) and the clear regions are fluid. The channel walls are at an angle θ_{chan} to the x axis. The model uses the (x,y) coordinate system, so the flow in the model is 2D. The channel-aligned coordinate system (X,Y) (with X denoting the along-channel distance and Y the cross-channel distance) is only used in the derivation of analytic solutions for various 1D channel flows (Appendix E). The dimensions of the domain in the x and y directions, L_x and L_y, must be related by $L_y = L_x \tan\theta_{\text{chan}}$ in order for the periodic boundary conditions along the edges of the domain to be satisfied. w_{chan} and w_{wall} are the channel width and the wall thickness, respectively, and $w = w_{\text{chan}} + w_{\text{wall}}$ is the distance between wall centerlines. Also shown is the velocity profile $U(Y)$ or $U(Y,t)$ used in the analytic solutions in TCs 1–6 in Section 7.1.

for these, the PLS and UNPLS are equivalent. That's because in these TCs, there is no forcing and the initial velocity field is zero near boundaries, so the shifted coordinates are not needed. We perform all the GRSs in Cartesian coordinates $(\xi,\eta) = (x,y)$, and in all simulations, we use the fourth-order Runge–Kutta method (RK4) to advance the solution forward in time.

The original AL81 scheme (without land) is second-order accurate in $\Delta\xi$ and $\Delta\eta$. Thus, the most we can expect from the GRSs is second-order convergence of the errors [although in some cases (e.g. TCs 4–6), we obtain rates that are slightly higher than this theoretical maximum, e.g. 2.2; see Table 3]. For each GRS, we have plotted the L_1, L_2, and L_∞ error norms of h, u, v, ζ, and q as functions of the grid size at regular time intervals and have observed their rates of convergence to zero. In some cases, these rates stay essentially unchanged with time and grid size. For these, we report a single convergence rate. In other cases, the rates vary with time and/or grid size (i.e. the error norm as a function of the grid size might not be perfectly linear on a log–log plot). For these, we list a range of rates (e.g. 1.5–2).

7.1. Test cases 1–6: channel flows

First, we discuss the six channel flow TCs. Fig. 6 shows the orientation of the channel with respect to the Cartesian coordinate system (x,y) used in the model. We can see from this figure that the channel is situated at an angle θ_{chan} to the x axis. Thus, as far as the model is concerned, the flow is 2D. TCs 1–3 are with $\theta_{\text{chan}} = 30°$, and TCs 4–6 are with $\theta_{\text{chan}} = 10°$. In order for the channel geometry to satisfy the periodic boundary conditions along the edges of the domain, the domain sizes L_x and L_y in the x and y directions must be related by $L_y = L_x \tan\theta_{\text{chan}}$. In all six TCs, we use $L_x = 20$ km. Thus, in TCs 1–3, $L_y \approx 11.55$ km, and in TCs 4–6, $L_y \approx 3.53$ km. The perpendicular distance w between the centerlines of the two walls in Fig. 6 is $L_x \sin\theta_{\text{chan}}$. This distance is also equal to the sum of the wall-to-wall width of the channel w_{chan} and the width of the wall w_{wall}, i.e. $w = w_{\text{chan}} + w_{\text{wall}}$. We choose w_{wall} to be $0.19w$ in all six TCs. Thus, $w_{\text{chan}} = 0.81w = 0.81 L_x \sin\theta_{\text{chan}}$. For TCs 1–3, this gives $w_{\text{chan}} = 8.1$ km, and for TCs 4–6, it gives $w_{\text{chan}} = 2.81$ km.

The grids we use in the GRSs of TCs 1–3 have sizes $\Delta x \times \Delta y = 250$ m $\times$ 251.02 m, 125 m $\times$ 125.51 m, 62.5 m $\times$ 62.76 m, and 31.25 m $\times$ 31.38 m. The corresponding time steps are 20 s, 10 s, 5 s, and 2.5 s for TCs 1 and 2 and 10 s, 5 s, 2.5 s, and 1.25 s for TC 3. The grids for TCs 4–6 have sizes $\Delta x \times \Delta y = 125$ m $\times$ 125.95 m, 62.5 m $\times$ 62.97 m, 31.25 m $\times$ 31.49 m, and 15.625 m $\times$ 15.743 m. The corresponding time steps are 10 s, 5 s, 2.5 s, and 1.25 s for TCs 4 and 5 and 4 s, 2 s, 1 s, and 0.5 s for TC 6. (See Appendix D for a discussion of the procedure used to set the time step.) We integrate all six TCs to a maximum time of $t = 20{,}000$ s.

Motion can be initiated in the model by specifying appropriate initial conditions (i.e. by specifying a nonzero initial velocity and/or a nonuniform depth) and/or by specifying an external forcing. We are interested in the accuracies of the STS, PLS,

and UNPLS in both of these situations. We are also interested in the effects of rotation (i.e. zero vs. nonzero Coriolis parameter f) and boundary angle θ_{bdy} (Fig. 4) on accuracy. The channel flow TCs are designed to assess the effects of these factors on the accuracies of the schemes under the constraint that there be an analytic solution with which the results can be compared. For this purpose, in Appendix E we derive two analytic solutions for 1D channel flow. First, we derive a solution for the non-rotating case ($f = 0$) that has a nonzero initial velocity and a nonzero (but transient) forcing. This solution [expressed in a Cartesian coordinate system (X,Y) aligned with the channel; see Fig. 6] is given by Eqs. (189), (194), (198) and (200). (Note that either the initial velocity or the forcing can be set to zero if desired; the solution will still be non-trivial. However, if the forcing is set to zero, the solution will become time-independent.) One drawback of using this solution as a test case is that h is constant in space and time. Thus, some of the terms in the discrete equations (e.g. the pressure gradients) will be zero or negligible. To activate these terms and to include the effects of rotation, in Appendix E we derive a second analytic solution for the case of a constant (nonzero) f and zero forcing. In this case, the solution [again in the channel-aligned (X,Y) coordinate system] is given by Eqs. (189), (204) and (205). We can see from (205) that the fluid depth is now spatially variable. Note that the solution in this case is time-independent. (We were unable to find a time-dependent analytic solution for $f \neq 0$.)

We now discuss the use of these analytic solutions in TCs 1–6. In TCs 1 and 4, we test the accuracies of the schemes for the case of no rotation, no forcing, and a time-independent solution. The analytic solution in this case [expressed in the channel-aligned coordinate system (X,Y)] is given by (189), (194), (198) and (200) with $(S_X/h)_{bot}$, $(S_X/h)_{ctr}$, and $(S_X/h)_{top}$ in (200) set to zero (i.e. no forcing). This solution can be expressed in terms of the model coordinate system (x,y) and its velocity components u and v as

$$h = h_o \tag{61}$$
$$u(x,y) = U(Y(x,y)) \times \cos\theta_{chan} \tag{62}$$
$$v(x,y) = U(Y(x,y)) \times \sin\theta_{chan} \tag{63}$$

where, from (200), the along-channel velocity $U(Y)$ is given by

$$U(Y) = U_{ctr} + (U_{top} - U_{bot})\frac{Y}{w_{chan}} + 2(U_{top} - 2U_{ctr} + U_{bot})\left(\frac{Y}{w_{chan}}\right)^2 \tag{64}$$

In (62) and (63), the cross-channel distance Y (measured from the channel centerline; see Fig. 6) is given in terms of x and y as follows:

$$Y(x,y) = \begin{cases} -w + (-x\sin\theta_{chan} + y\cos\theta_{chan}) & \text{in the upper-left channel in Fig. 6} \\ -x\sin\theta_{chan} + y\cos\theta_{chan} & \text{in the central channel in Fig. 6} \\ w - (-x\sin\theta_{chan} + y\cos\theta_{chan}) & \text{in the lower-right channel in Fig. 6} \end{cases} \tag{65}$$

In TCs 1 and 4, we choose $h_o = 5$ m in (61) and $U_{bot} = -1$ m s^{-1}, $U_{ctr} = 1$ m s^{-1}, and $U_{top} = 0.5$ m s^{-1} in (64). The resulting cross-channel velocity profile $U(Y)$ is shown in Fig. 6. Note that since the solution is time-independent, the initial conditions are given by (61)–(63). Also, since there is no forcing, the vorticity source term $S^{(\zeta)}$ is zero in these two TCs.

In TCs 2 and 5, we test the accuracies of the schemes for the case of no rotation, no initial velocity, and a gradual, transient forcing that ramps up the velocity to some steady-state solution. The analytic solution [expressed in the (X,Y) coordinate system] is again given by (189), (194), (198) and (200) but now with U_{bot}, U_{ctr}, and U_{top} in (200) set to zero (i.e. no initial velocity). In terms of the (x,y) model coordinate system and its velocity components u and v, the solution is given by

$$h = h_o \tag{66}$$
$$u(x,y,t) = U(Y(x,y),t) \times \cos\theta_{chan} \tag{67}$$
$$v(x,y,t) = U(Y(x,y),t) \times \sin\theta_{chan} \tag{68}$$

where $Y(x,y)$ is again given by (65) and, from (200), $U(Y,t)$ is given by

$$U(Y,t) = \left[(S_X/h)_{ctr} + \left\{(S_X/h)_{top} - (S_X/h)_{bot}\right\}\frac{Y}{w_{chan}} + 2\left\{(S_X/h)_{top} - 2(S_X/h)_{ctr} + (S_X/h)_{bot}\right\}\left(\frac{Y}{w_{chan}}\right)^2\right] \times I(t) \tag{69}$$

with $I(t)$ given by (198). The initial conditions are

$$h = h_o \tag{70}$$
$$u = v = 0 \tag{71}$$

In TCs 2 and 5, we choose $h_o = 5$ m in (66) and (70) and $(S_X/h)_{bot} = -2 \times 10^{-4}$ m s^{-2}, $(S_X/h)_{ctr} = 2 \times 10^{-4}$ m s^{-2}, and $(S_X/h)_{top} = 10^{-4}$ m s^{-2} in (69). These values are chosen such that as $t \to \infty$, (66)–(68) become identical to (61)–(63). The shape of the resulting velocity profile $U(Y,t)$ is shown in Fig. 6. Note that the shape of $U(Y,t)$ does not change in time but its magnitude does.

The vorticity source term $S^{(\zeta)}$ for TCs 2 and 5 can be obtained in the (X,Y) coordinate system by setting $(\xi,\eta) = (X,Y)$ and $m = n = 1$ in (11). This gives

$$S^{(\zeta)} = \frac{\partial}{\partial X}\left(\frac{S_Y}{h}\right) - \frac{\partial}{\partial Y}\left(\frac{S_X}{h}\right)$$

Substituting (190) and (195) into this, carrying out the differentiation with respect to Y, and rewriting the result as a function of x and y, we obtain

$$S^{(\zeta)}(x,y,t) = -\frac{1}{w_{\text{chan}}}\left[\left\{(S_X/h)_{\text{top}} - (S_X/h)_{\text{bot}}\right\} + 4\left\{(S_X/h)_{\text{top}} - 2(S_X/h)_{\text{ctr}} + (S_X/h)_{\text{bot}}\right\}\frac{Y(x,y)}{w_{\text{chan}}}\right] \times T(t) \tag{72}$$

where $T(t)$ is given by (196). In TCs 2 and 5, we obtain the source term $S^{(\zeta)}_{i+1/2,j+1/2}$ on the RHS of the discrete flux-form vorticity equation (32) at the boundary ζ-point at $(i+1/2, j+1/2)$ by evaluating (72) at $(\xi_{i+1/2}, \eta_{j+1/2}) = (x_{i+1/2}, y_{j+1/2})$ and multiplying the result by the area $A^{(\zeta)}_{i+1/2,j+1/2}$.

Finally, in TCs 3 and 6, we check the accuracies of the schemes for the case of $f \neq 0$. We set the forcing in these two TCs to zero because the only analytic solution we have when $f \neq 0$ is a steady-state solution without forcing. The analytic solution is thus given by Eqs. (189), (204) and (205) of Appendix E. In terms of the model coordinate system (x,y) and its velocity components u and v, we can write this solution as

$$h(x,y) = h_{\text{bot}} - \frac{f}{g} w_{\text{chan}} \times \left[\frac{U_{\text{ctr}}}{2}\left\{2\left(\frac{Y(x,y)}{w_{\text{chan}}}\right) + 1\right\} + \frac{U_{\text{top}} - U_{\text{bot}}}{8}\left\{4\left(\frac{Y(x,y)}{w_{\text{chan}}}\right)^2 - 1\right\} + \frac{U_{\text{top}} - 2U_{\text{ctr}} + U_{\text{bot}}}{12}\left\{8\left(\frac{Y(x,y)}{w_{\text{chan}}}\right)^3 + 1\right\}\right] \tag{73}$$

$$u(x,y) = U(Y(x,y)) \times \cos\theta_{\text{chan}} \tag{74}$$

$$v(x,y) = U(Y(x,y)) \times \sin\theta_{\text{chan}} \tag{75}$$

where $U(Y)$ is given by (204) [which is identical to (64)] and $Y(x,y)$ is given by (65). In both TCs 3 and 6, we choose $U_{\text{bot}} = -1$ m s^{-1}, $U_{\text{ctr}} = 1$ m s^{-1}, and $U_{\text{top}} = 0.5$ m s^{-1}, which are the same values used in TCs 1 and 4. As in the latter two TCs, the vorticity source term $S^{(\zeta)}$ is zero in TCs 3 and 6 because the forcing is zero. Note that h_{bot} and f must be chosen such that the RHS of (73) is positive for all Y between $-w_{\text{chan}}/2$ and $w_{\text{chan}}/2$. In addition, in order for rotational scales [determined by the Rossby radius of deformation $R = (gh)^{1/2}/|f|$] to be resolved by the domain, we require that R be smaller than w_{chan}. To satisfy these requirements, we have chosen $h_{\text{bot}} = 50$ m and $f = 10^{-2}$ s^{-1} for TC 3 and $h_{\text{bot}} = 50$ m and $f = 10^{-1}$ s^{-1} for TC 6. For TC 3 (for which $w_{\text{chan}} = 8.1$ km), these values give minimum and maximum h values of 45.2 m and 50.7 m and corresponding R values of 2.11 km and 2.23 km. For TC 6 (for which $w_{\text{chan}} = 2.81$ km), we get minimum and maximum h values of 33.3 m and 52.4 m and corresponding R values of 181 m and 227 m.

The rates of convergence obtained from the GRSs of TCs 1–3 ($\theta_{\text{chan}} = 30°$) are listed in Table 2, and the rates from the GRSs of TCs 4–6 ($\theta_{\text{chan}} = 10°$) are listed in Table 3. Note that in all our GRSs (including the ones for TCs 7–10 in Section 7.2), the largest absolute error is invariably at or near (i.e. within a grid box or two of) a boundary. Thus, the L_∞ error norm (which is defined as the largest absolute error in a variable anywhere in the flow domain; see Appendix C) represents the error at or near boundaries. With this in mind, we now draw the following conclusions from Tables 2 and 3:

1. In all TCs, the convergence rates of all three error norms of h, u, and v for the PLS are larger than those for the STS. In almost all cases, these rates are about 1 order higher for the PLS. The only exception to this is $\|\Delta h\|_\infty$ for the $f \neq 0$ TCs (3 and 6). In these TCs, the $\|\Delta h\|_\infty$ convergence rates are still larger for the PLS than for the STS but only by 0.4–0.6 order.
2. u and v near boundaries (as measured by $\|\Delta u\|_\infty$ and $\|\Delta v\|_\infty$) do not converge for the STS (i.e. they have convergence rates of 0) but always converge for the PLS and UNPLS. Similarly, h near boundaries does not converge for the STS except for the $f \neq 0$ TCs, but it always converges for the PLS and UNPLS.
3. The convergence rates of h for the PLS and UNPLS are identical in all six TCs.
4. The convergence rates of ζ and q for the UNPLS are generally smaller than those for the PLS and STS. In fact, except for TC 6 [and possibly also TC 5, in which $\|\Delta\zeta\|_2$ does not converge but $\|\Delta\zeta\|_\infty$ does (although at the minimal rate of 0.2–0.3)], ζ and q near boundaries do not converge for the UNPLS. On the other hand, for the PLS, ζ and q near boundaries converge in all TCs. This shows that the use of the shifted locations in the PLS is an effective means of bringing about convergence of the relative vorticity $\zeta_{\text{rel},i+1/2,j+1/2}$ and/or the vorticity source term $S^{(\zeta)}_{i+1/2,j+1/2}$ at near-boundary ζ-points, and this in turn improves the convergence rates of ζ and q both near and away from boundaries.
5. The convergence rates of u and v for the PLS are always at least as large as those for the UNPLS and often somewhat larger. This indicates that having $q_{i+1/2,j+1/2}$ converge at near-boundary ζ-points in the PLS also helps u and v converge faster. [We emphasize the convergence of $q_{i+1/2,j+1/2}$ here because it is $q_{i+1/2,j+1/2}$, not $\zeta_{i+1/2,j+1/2}$, that appears in the nonlinear terms on the RHSs of the momentum equations (18) and (19).]
6. In the unforced TCs (1, 3, 4, and 6), ζ converges somewhat faster for the PLS than for the STS. In these TCs, the error norms of ζ for the STS are more jagged functions of the grid size and are more variable in time than they are for the PLS. In the forced TCs (2 and 5), ζ converges slightly faster for the STS than for the PLS. In these TCs, the error norms of ζ are very smooth functions of the grid size and time for both schemes.

Table 2
Rates of convergence of the L_1, L_2, and L_∞ error norms of h, u, v, ζ, and q with decreasing grid size for TCs 1–3 (channel at $\theta_{chan} = 30^\circ$ to the x axis) obtained from grid refinement studies with the stairstep (STS), piecewise linear (PLS), and unshifted piecewise linear (UNPLS) schemes.

		h	u	v	ζ	q
TC 1 (channel at 30°, no forcing, f = 0)						
STS	L_1	0.7–0.8	0.9	0.8–0.9	1–1.4	1.6
	L_2	0.6	0.5	0.5	0.8–1.4	1.5
	L_∞	0	0	0	0–1	0.9–1.1
PLS	L_1	1.6–1.7	2	1.8–1.9	1.5	1.5
	L_2	1.5	1.5	1.5	1.5	1.5
	L_∞	0.9–1	1	1	1–1.2	1–1.2
UNPLS	L_1	1.6–1.7	1.5	1.5–1.6	0.6	0.6
	L_2	1.5	1.4	1.5	0.5	0.5
	L_∞	0.9–1	0.7–1	0.8–1.1	0	0
TC 2 (channel at 30°, with forcing, f = 0)						
STS	L_1	0.9	1	1	1.8	2
	L_2	0.5	0.5	0.5	1.4–1.6	1.4–1.5
	L_∞	0	0	0	1.1–1.2	0.8–0.9
PLS	L_1	2	2	2	1.7	1.8
	L_2	1.5	1.5	1.5	1.6	1.6
	L_∞	0.9–1	1	1	1.1–1.3	1.1–1.3
UNPLS	L_1	2	1.6	1.9	0.7	0.7
	L_2	1.5	1.4	1.5	0.5	0.5
	L_∞	0.9–1	0.9	0.9–1.1	0	0
TC 3 (channel at 30°, no forcing, $f = 10^{-2}\,s^{-1}$)						
STS	L_1	0.8–0.9	1	0.9–1	0.9–1	1.7
	L_2	0.8–1	0.5	0.5	0.8–0.9	1.5
	L_∞	0.3–0.4	0	0	0.4–0.5	1
PLS	L_1	2	2	2	1.5	1.7
	L_2	1.6	1.5	1.5	1.4	1.5
	L_∞	1	1	1	1–1.1	1.1–1.2
UNPLS	L_1	2	1.5–1.6	1.7	0.6	0.6
	L_2	1.6	1.4	1.4–1.5	0.5	0.5
	L_∞	1	0.8–1	0.9–1.1	0	0

7. q for the STS and PLS converges at about the same rate (possibly slightly faster for the STS in the forced TCs). For both these schemes, the error norms of q are very smooth functions of the grid size and time in all TCs (even in the GRSs with the STS in which the error norms of ζ are jagged functions of the grid size and variable in time).

The results of these channel flow TCs indicate that overall, the PLS is the most accurate scheme because it simulates h, u, and v more accurately than the STS, ζ and q about as accurately as the STS, h as accurately as the UNPLS, u and v slightly more accurately than the UNPLS, and ζ and q more accurately than the UNPLS.

7.2. Test cases 7–10: annulus flows

We now discuss the four TCs of flow in an annulus. We use the same annulus geometry in all four TCs, with the inner boundary at $r = 5$ km and the outer boundary at $r = 25$ km (where r is the radial distance from the origin). Also, to perform the GRSs, we use the same set of (Cartesian) grids in all four TCs. These grids have sizes $\Delta x = \Delta y = 500$ m, 250 m, 125 m, and 62.5 m. The corresponding time steps are 10 s, 5 s, 2 s, and 1 s for TCs 7–9 and 5 s, 2 s, 1 s, and 0.5 s for TC 10. (See Appendix D for a discussion of the procedure used to set the time step.)

Since we do not have analytic solutions for these TCs, we obtain the "exact" solution for each TC by performing a simulation in cylindrical coordinates $(\xi, \eta) = (r, \theta)$ on a highly refined grid. (Recall that the exact solution is needed for the calculation of the error norms; see Appendix C.) We do this because any simulation of the annulus geometry in cylindrical coordinates is more accurate than one in Cartesian coordinates with comparable resolution. This is because in (r, θ) space, the boundaries of the annulus can be made to lie exactly along grid lines. This eliminates the need for stairsteps (which are present in the simulations with the STS in Cartesian coordinates) or boundary boxes (i.e. boxes that lie partially in fluid and partially in land that are present in the simulations with the PLS and UNPLS in Cartesian coordinates), both of which are sources of error and reduce the accuracy of the model. Note that since there are no stairsteps or boundary boxes in cylindrical coordinates, the STS, PLS, and UNPLS reduce to the same scheme in this coordinate system (but only for the particular case of the annulus geometry considered here). To obtain the "exact" solutions for TCs 7–9, we use a cylindrical grid with

Table 3
Rates of convergence of the L_1, L_2, and L_∞ error norms of h, u, v, ζ, and q with decreasing grid size for TCs 4–6 (channel at $\theta_{chan} = 10°$ to the x axis) obtained from grid refinement studies with the stairstep (STS), piecewise linear (PLS), and unshifted piecewise linear (UNPLS) schemes.

		h	u	v	ζ	q
TC 4 (channel at 10°, no forcing, $f = 0$)						
STS	L_1	0.9–1.1	0.9–1	0.9–1	1.3–1.4	1.7
	L_2	0.9–1	0.5	0.5	1.3–1.4	1.5
	L_∞	0	0	0	1–1.2	1–1.1
PLS	L_1	1.9	2.2	2	1.5	1.5
	L_2	1.7	1.5	1.7	1.5	1.5
	L_∞	0.8–1	1	1–1.1	1–1.2	1–1.2
UNPLS	L_1	1.9	1.4–1.5	1.8	0.4–0.5	0.4
	L_2	1.7	1.3–1.4	1.7	0.4	0.3
	L_∞	0.8–1	1–1.2	1–1.2	0	0
TC 5 (channel at 10°, with forcing, $f = 0$)						
STS	L_1	0.9	1	1	2.1	2.1
	L_2	0.4	0.5	0.5	1.7	1.5
	L_∞	0	0	0	1	0.9–1
PLS	L_1	1.9	2.2	2	1.9	1.9
	L_2	1.7	1.5	1.7	1.6	1.5
	L_∞	0.9	1	1.1	1	1.1
UNPLS	L_1	1.9	1.5	2	0.5	0.4
	L_2	1.7	1.3	1.7	0	0
	L_∞	0.9	1.2	1.1	0.2–0.3	0.2–0.3
TC 6 (channel at 10°, no forcing, $f = 10^{-1}\ s^{-1}$)						
STS	L_1	0.9–1	1	0.9–1	0.9–1.1	1.7
	L_2	0.9–1.1	0.5	0.5	1–1.1	1.5
	L_∞	0.5–0.6	0	0	0.5–1.1	1
PLS	L_1	1.8–2.2	2.2	2.1–2.2	1.4	1.7
	L_2	1.9	2	2.2	1.2	1.5
	L_∞	1	1.2–1.4	1.5	0.7–0.9	1.1
UNPLS	L_1	1.8–2.2	2.2	2.1–2.2	1.3–1.4	1.7
	L_2	1.9	2	2.2	1–1.2	1.5
	L_∞	1	1.5–1.6	1.5–1.6	0.7–0.9	1.1–1.2

sizes $\Delta r \times \Delta\theta = 62.5\ \text{m} \times 0.14°$ and a time step of 1 s, and to obtain the "exact" solution for TC 10, we use a grid with $\Delta r \times \Delta\theta = 15.625\ \text{m} \times 0.27°$ and a time step of 2 s.

7.2.1. Test case 7: irrotational gravity waves

First, we consider irrotational flow (i.e. $\zeta = 0$). We set $f = 0$ and $S_\xi = S_\eta = 0$ (i.e. no forcing), and we initialize the flow with $u = v = 0$ and h given by

$$h = h_o + h_{peak} \times \exp\left[-\frac{\{(x - x_o)^2 + (y - y_o)^2\}}{(3\ \text{km})^2}\right] \tag{76}$$

where $h_o = 5$ m, $h_{peak} = 0.1$ m, $x_o = r_o \cos\theta_o$, and $y_o = r_o \sin\theta_o$ with $r_o = 15$ km and $\theta_o = 60°$. This corresponds to a Gaussian hill of fluid of peak height 0.1 m (relative to the 5 m background depth) centered at $(r, \theta) = (15\ \text{km}, 60°)$ [Fig. 7, panel (a)]. We integrate these initial conditions to a maximum time of 10,000 s. As the integration advances, gravity waves propagate out from the fluid hill and reflect off the boundaries. Many such reflections occur during the integration period. As an example, we show in panel (b) of Fig. 7 the depth and velocity fields at $t = 2000$ s from the PLS simulation on the 500 m grid (which is the coarsest Cartesian grid). Note that since in this TC the initial velocity and the forcing are both zero, the shifted coordinates $\xi^{(v)*}_{i,j+1/2}$ and $\eta^{(u)*}_{i+1/2,j}$ (Section 4.4) are not needed. Thus, the PLS and UNPLS reduce to the same scheme. Here, we refer to this scheme simply as the PLS.

Table 4 lists the convergence rates of the error norms of h, u, and v for the STS and PLS for TC 7. We can see from this table that these rates are 0.5–1 order higher for the PLS than for the STS. In particular, $\|\Delta u\|_\infty$ and $\|\Delta v\|_\infty$ converge at a rate between 1 and 2 for the PLS, but they do not converge at all for the STS. This indicates that u and v near boundaries converge for the PLS but not for the STS.

If the vorticity source term $S^{(\zeta)}$ is zero, we can rewrite Eq. (7) as

$$\frac{\partial \zeta}{\partial t} = -\left[mu\frac{\partial \zeta}{\partial \xi} + nv\frac{\partial \zeta}{\partial \eta}\right] - \zeta(\nabla \cdot \boldsymbol{u}) \tag{77}$$

where the velocity divergence in orthogonal curvilinear coordinates is given by

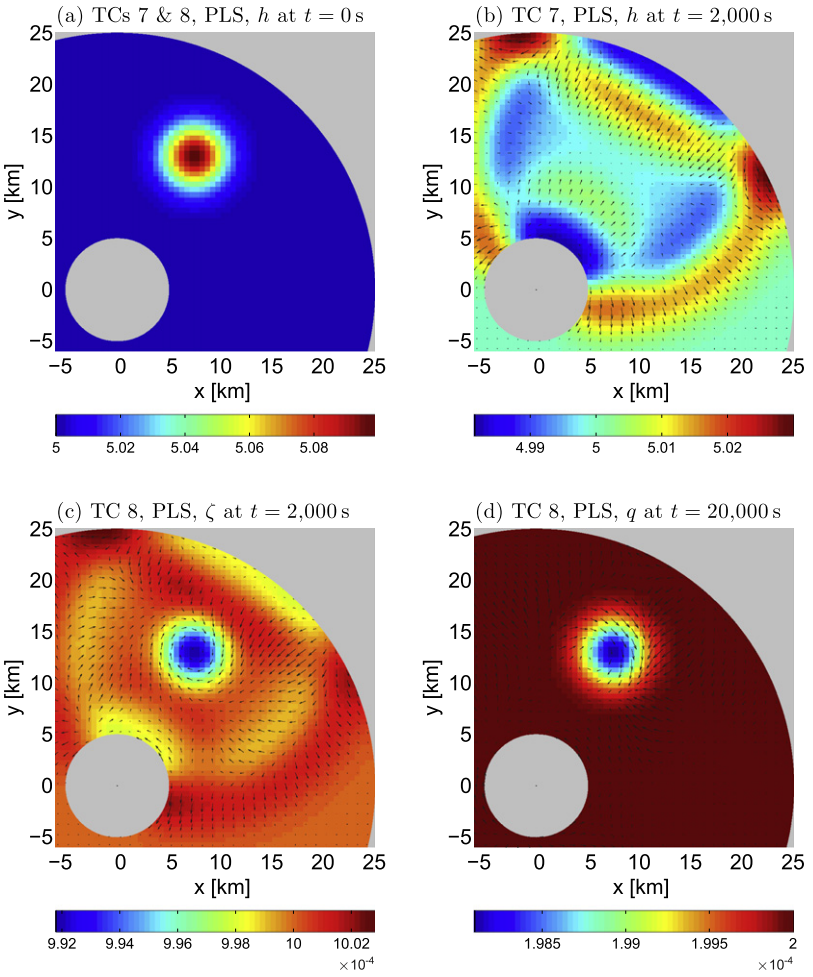

Fig. 7. (a) Initial fluid depth h (in m) for TCs 7 (irrotational gravity waves) and 8 (rotational gravity waves), (b) h and velocities at $t = 2000$ s for TC 7, (c) vorticity ζ (in s^{-1}) and velocities at $t = 2000$ s for TC 8, and (d) potential vorticity q (in $m^{-1}\,s^{-1}$) and velocities at $t = 20{,}000$ s for TC 8. All figures are from PLS simulations on the $\Delta x = \Delta y = 500$ m grid. For clarity, velocity vectors in (b), (c), and (d) are shown at only every second grid point. The maximum velocity magnitude is 0.033 m s^{-1} in (b), 0.017 m s^{-1} in (c), and 0.015 m s^{-1} in (d). For plotting purposes, u, v, and ζ have been interpolated from u-, v-, and ζ-points to h-points (Appendix C). Rates of convergence are listed in Table 4.

$$\nabla \cdot \boldsymbol{u} = mn\left[\frac{\partial}{\partial \xi}\left(\frac{u}{n}\right) + \frac{\partial}{\partial \eta}\left(\frac{v}{m}\right)\right] \tag{78}$$

From (77), we see that if ζ is initially zero everywhere, it will remain zero at all later times. In the current TC, ζ is initially zero, and $S^{(\zeta)}$ is zero because $S_\xi = S_\eta = 0$. Thus, ζ should remain zero throughout the integration. Both the STS and the PLS maintain this property of the continuous equations. For both schemes and considered over all the grids, the vorticity at the end of the simulation consists of a noisy field of roundoff error having maximum absolute value less that $10^{-17}\,s^{-1}$.

7.2.2. Test case 8: rotational gravity waves

Next, we consider flow in which vorticity is initially present due only to the Coriolis effect (i.e. initially, there is no relative vorticity, only planetary vorticity). To ensure that rotation has a significant effect in this flow, we set f to the relatively high value of $10^{-3}\,s^{-1}$ (i.e. relative to the usual value of $10^{-4}\,s^{-1}$ used for mid-latitudes). We use the same initial conditions and zero forcings as in TC 7 except that we set $h_{peak} = 0.05$ m instead of 0.1 m. (The choice of $h_{peak} = 0.05$ m vs. 0.1 m is random and makes no difference in the results). Thus, as in TC 7, the PLS and UNPLS in this TC reduce to the same scheme which we refer to simply as the PLS.

We integrate this TC to 20,000 s. As in TC 7, gravity waves propagate out from the initial fluid hill, but unlike in TC 7, they now transport vorticity. The gravity waves are rotational because the initial fluid hill quickly generates a velocity divergence, and this in turn interacts with the nonzero initial vorticity ($\zeta = f$) to produce a nonzero vorticity tendency [via the second term on the RHS of (77)]. These rotational gravity waves reflect off the boundaries many times throughout the integration.

Table 4
Rates of convergence of the L_1, L_2, and L_∞ error norms of h, u, v, ζ, and q with decreasing grid size for TCs 7 (irrotational gravity waves), 8 (rotational gravity waves), and 10 (forced flow) obtained from grid refinement studies with the stairstep (STS), piecewise linear (PLS), and unshifted piecewise linear (UNPLS) schemes. All three TCs use the annulus geometry. In TCs 7 and 8, the PLS and UNPLS reduce to the same scheme, so results from the UNPLS are not listed. Also, in TC 7, no convergence rates are listed for ζ and q because these variables remain at their exact value of zero (within roundoff error) during all simulations.

		h	u	v	ζ	q
TC 7 (irrotational gravity waves, $f = 0$)						
STS	L_1	1.4	1.3	1.3	–	–
	L_2	1.4	0.5–1.5	0.5–1.5	–	–
	L_∞	1–1.5	0	0	–	–
PLS	L_1	2	2	2	–	–
	L_2	2	2	2	–	–
	L_∞	1–2	1–2	1–2	–	–
TC 8 (rotational gravity waves, $f = 10^{-3}\ s^{-1}$)						
STS	L_1	1.4	1.3	1.3	1.4	2
	L_2	1.4	1–1.5	1–1.5	1.4	2
	L_∞	1–1.5	0	0	1–1.5	2
PLS	L_1	2	2	2	2	2
	L_2	2	2	2	2	2
	L_∞	1–2	1–2	1–2	1–2	2
TC 10 (forced flow, $f = 0$)						
STS	L_1	1	0.9–1	0.9–1	1	1
	L_2	0.5–1	0.5	0.5	0.5	0.5
	L_∞	0	0	0	0	0
PLS	L_1	2	2	2	1.5	1.5
	L_2	1.6–1.8	1.5–1.6	1.5–1.6	1.2	1.2
	L_∞	1	1–1.1	1–1.1	0.4–0.6	0.4–0.6
UNPLS	L_1	2	1.8–2	1.8–2	0.9	0.9
	L_2	1.6–1.8	1.3–1.5	1.3–1.5	0.5	0.5
	L_∞	1	0.9–1	0.6–1	0	0

As an example, we show in panel (c) of Fig. 7 the vorticity and velocity fields at $t = 2000$ s from the PLS simulation on the 500 m grid.

Table 4 lists the convergence rates of the error norms of h, u, v, ζ, and q for the STS and PLS for TC 8. As in TC 7, these rates are 0.5–1 order higher for the PLS than for the STS, and again u and v near boundaries converge for the PLS but not for the STS. Note also that for both schemes, all three error norms of q converge at a rate of 2. This is discussed further in the following section.

7.2.3. Test case 9: potential vorticity advection

Although q in TC 8 is nonzero, its spatially varying part is generated at and remains very near the location of the initial hill of fluid; it does not approach and interact with the boundaries. This can be seen in panel (d) of Fig. 7, which shows q and the velocities at the final time of $t = 20{,}000$ s from the PLS simulation on the 500 m grid. The potential vorticity field does not move much after it has been generated because the flow in TC 8 consists only of gravity waves, and these do not generate a persistent velocity field that can advect q any significant distance. Since the AL81 scheme away from boundaries is second-order accurate and since by design, both the STS and the PLS can handle a constant potential vorticity field perfectly (i.e. to within roundoff error; see Section 6 of KJ09), in TC 8 all three error norms of q converge at a rate of 2 for both schemes (Table 4).

Although this is a reassuring result, we are also interested in the accuracy of the boundary schemes when the spatially variable part of the potential vorticity interacts with the boundaries. To generate a flow in which this occurs, we choose TC 9 such that it is identical to TC 8 in all ways except that the initial velocity field is nonzero. In terms of the cylindrical velocity components u_r and u_θ, this field is given by

$$u_r(r,\theta) = (0.8\ \mathrm{m\ s^{-1}}) \times \cos(2\theta) \times B(r) \tag{79}$$

$$u_\theta(r) = (0.1\ \mathrm{m\ s^{-1}}) \times B(r) \tag{80}$$

where the radial dependence $B(r)$ is given by

$$B(r) = \exp\left[-\left(\frac{r - r_o}{3\ \mathrm{km}}\right)^2\right] \times \left[1 - \cos^{10}\left\{\frac{\pi}{20\ \mathrm{km}}(r - 5\ \mathrm{km})\right\}\right] \tag{81}$$

Note that u_r at the annulus boundaries (at $r = 5$ km and 25 km) is zero as required by the no-flux boundary condition, and it can be shown that the initial vorticity at the boundaries (which must be specified as part of the initial conditions) is zero as well. The initial Cartesian velocity components u and v are given by

$$u = u_r(r,\theta)\cos\theta - u_\theta(r,\theta)\sin\theta \tag{82}$$

$$v = u_r(r,\theta)\sin\theta + u_\theta(r,\theta)\cos\theta \tag{83}$$

where

$$r = (x^2 + y^2)^{1/2} \quad \text{and} \quad \theta = \tan^{-1}(y/x) \tag{84}$$

Panel (a) of Fig. 8 shows the initial q and velocity fields corresponding to (79) and (80) on the 62.5 m grid (which is the finest Cartesian grid). Note that as in TCs 7 and 8, the PLS and UNPLS reduce to the same scheme in this TC because the forcing is again zero and the initial velocity field is nonzero only in a region away from the boundaries [Fig. 8, panel (a)]. Again, we refer to this scheme simply as the PLS.

We integrate this TC to 80,000 s in order to give q enough time to reach and interact fully with the inner boundary of the annulus. The q and velocity fields at this final time from the PLS simulation on the 62.5 m grid are shown in panel (b) of Fig. 8. We can see that by this time, the core of positive q has rotated counterclockwise, and its western end has reached and is being stretched around the inner boundary. The bulk of the core of positive q is being advected around the east side of the island, but a thin filament is being advected around the west side. This filament gets progressively thinner until it cannot be resolved even on the finest grid. This starts to occur gradually after about 80,000 s. For this reason, we do not integrate beyond this time.

In this TC, the initial nonzero velocity field generates additional gravity waves, i.e. in addition to the ones generated by the initial Gaussian hill of fluid. These steepen and break relatively early in the simulation (around t = 10,000 s). This wave

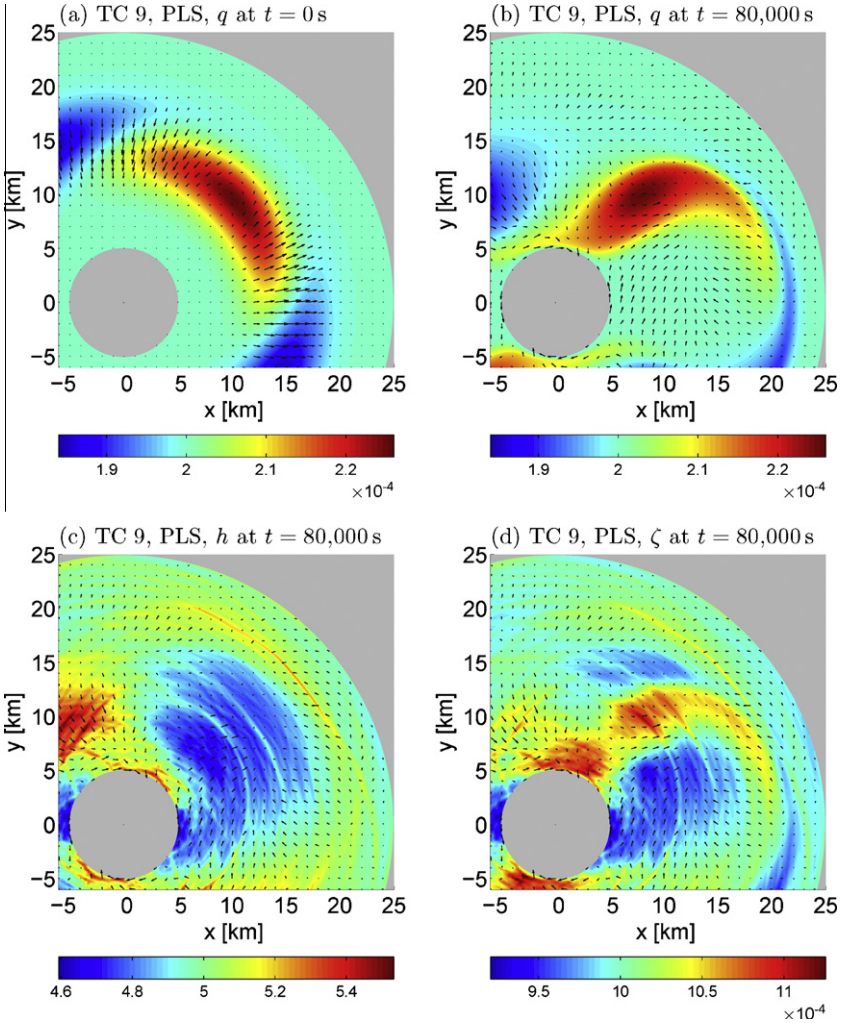

Fig. 8. Various fields from the PLS simulation of TC 9 (potential vorticity advection) on the $\Delta x = \Delta y$ = 62.5 m grid. (a) Initial potential vorticity q (in m^{-1} s^{-1}) and velocities, (b) q and velocities at t = 80,000 s, (c) fluid depth h (in m) and velocities at t = 80,000 s, and (d) vorticity ζ (in s^{-1}) and velocities at t = 80,000 s. For clarity, velocity vectors are shown at only every 16th grid point. The maximum velocity magnitude is 0.81 m s^{-1} in (a) and 0.51 m s^{-1} in (b)–(d). Panels (a) and (b) use the same color scale, and all four panels use the same vector length scale. For plotting purposes, u, v, ζ, and q have been interpolated from u-, v-, and ζ-points to h-points (Appendix C).

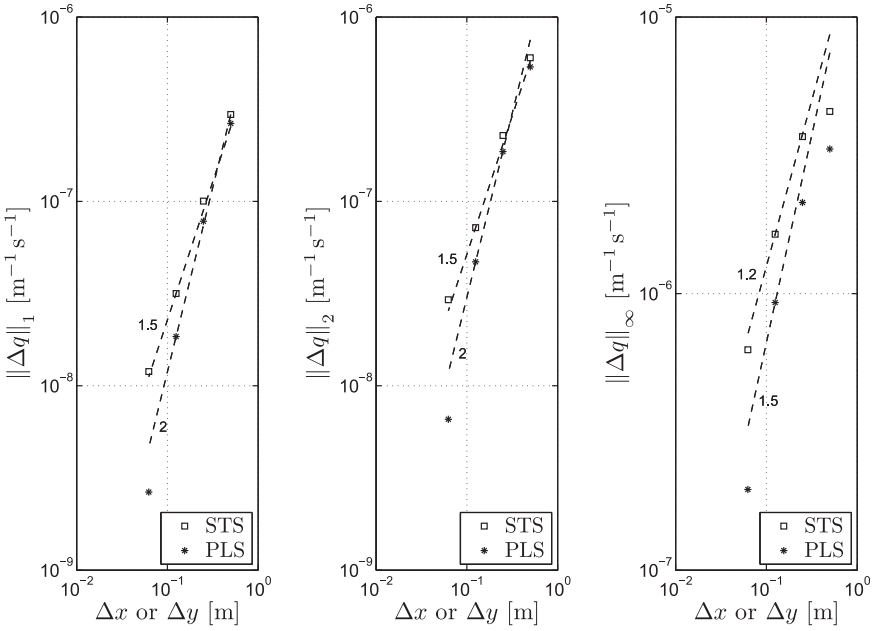

Fig. 9. L_1, L_2, and L_∞ error norms of q at t = 80,000 s for TC 9 (potential vorticity advection) from the STS and PLS. The dashed lines are reference lines having the indicated slopes.

steepening and breaking is marked by the appearance of fronts and oscillations in the h, u, v, and ζ fields. The oscillations arise presumably because the infinitely steep fronts cannot be resolved on any of the grids. These fronts and oscillations appear as streaks in panels (c) and (d) of Fig. 8, which show h and ζ along with the velocity vectors at t = 80,000 s from the PLS simulation on the 62.5 m grid. The fronts and oscillations are also present in the "exact" simulation on the highly-resolved cylindrical grid. As a result, it is not possible to reliably calculate the error norms of h, u, v, and ζ after about t = 10,000 s. Surprisingly (and fortunately), however, q remains quite smooth, as can be seen in panel (b) of Fig. 8. Throughout the integration period, its L_1, L_2, and L_∞ error norms converge at rates of 1.5, 1.5, and 1–2, respectively, for the STS and at rates of 2, 2, and 1–2, respectively, for the PLS. Note that $\|\Delta q\|_\infty$ is a somewhat jagged function of the grid size for both schemes, but it is almost always smaller in magnitude for the PLS than the STS. As an example, we show in Fig. 9 the error norms of q as functions of Δx or Δy at t = 80,000 s. [In this figure, the sharp decrease in the error norms of the PLS as we move from the 125 m to the 62.5 m (the finest) grid is due to the fact that the accuracy of the simulation on the 62.5 m grid approaches that of the "exact" simulation in cylindrical coordinates.] Thus, both the STS and the PLS advect potential vorticity around the inner annulus boundary reasonably well, but the PLS does a slightly better job.

7.2.4. Test case 10: forced flow

Since most simulations with the SWEs are going to involve some type of forcing (e.g. wind forcing), in this final TC we consider such a flow. We initialize the flow with $u = v = 0$ and $h = h_o = 5$ m, and for simplicity, we set $f = 0$. In the simulation in cylindrical coordinates used to obtain the "exact" solution, we initiate motion using the forcing terms $S_\xi/mh = S_r/h$ and $S_\eta/nh = rS_\theta/h$ on the RHSs of the momentum equations (2) and (3). Here, S_r and S_θ are the cylindrical components of the stress vector $\boldsymbol{S}$ (Section 2). We choose these to be

$$S_r = -(10^{-3}\ \mathrm{m^2\ s^{-2}})\frac{h}{h_o}(c_0 + c_1 r + c_2 r^2)\cos^4\left[\frac{1}{2}\left(\theta - \frac{2\pi}{3}\right)\right] \times T(t) \tag{85}$$

$$S_\theta = (10^{-3}\ \mathrm{m^2\ s^{-2}})\frac{h}{h_o}(c_0 + c_1 r + c_2 r^2)\cos^4\left[\frac{1}{2}\left(\theta - \frac{\pi}{3}\right)\right] \times T(t) \tag{86}$$

where $c_0 = 1.75$, $c_1 = -3.0 \times 10^{-4}\ \mathrm{m^{-1}}$, $c_2 = 10^{-8}\ \mathrm{m^{-2}}$, and $T(t)$ is the time-dependent part of the forcing. We choose this to be the same as the time-dependent part of the forcing in the forced 1D channel flow TCs 2 and 5, i.e. Eq. (196) of Appendix E. Substituting (85) and (86) into (11), we can show that the vorticity source term $S^{(\zeta)}$ on the RHS of (7) is given by

$$\begin{aligned} S^{(\zeta)} &= mn\left[\frac{\partial}{\partial\xi}\left(\frac{S_\eta}{nh}\right) - \frac{\partial}{\partial\eta}\left(\frac{S_\xi}{mh}\right)\right] = \frac{1}{r}\left[\frac{\partial}{\partial r}\left(\frac{rS_\theta}{h}\right) - \frac{\partial}{\partial\theta}\left(\frac{S_r}{h}\right)\right] \\ &= (10^{-3}\ \mathrm{m^2\ s^{-2}})\frac{1}{h_o r}\left[(c_0 + 2c_1 r + 3c_2 r^2)\cos^4\left\{\frac{1}{2}\left(\theta - \frac{\pi}{3}\right)\right\}\right. \\ &\quad \left. -2(c_0 + c_1 r + c_2 r^2)\cos^3\left\{\frac{1}{2}\left(\theta - \frac{2\pi}{3}\right)\right\}\sin\left\{\frac{1}{2}\left(\theta - \frac{2\pi}{3}\right)\right\}\right] \times T(t) \end{aligned} \tag{87}$$

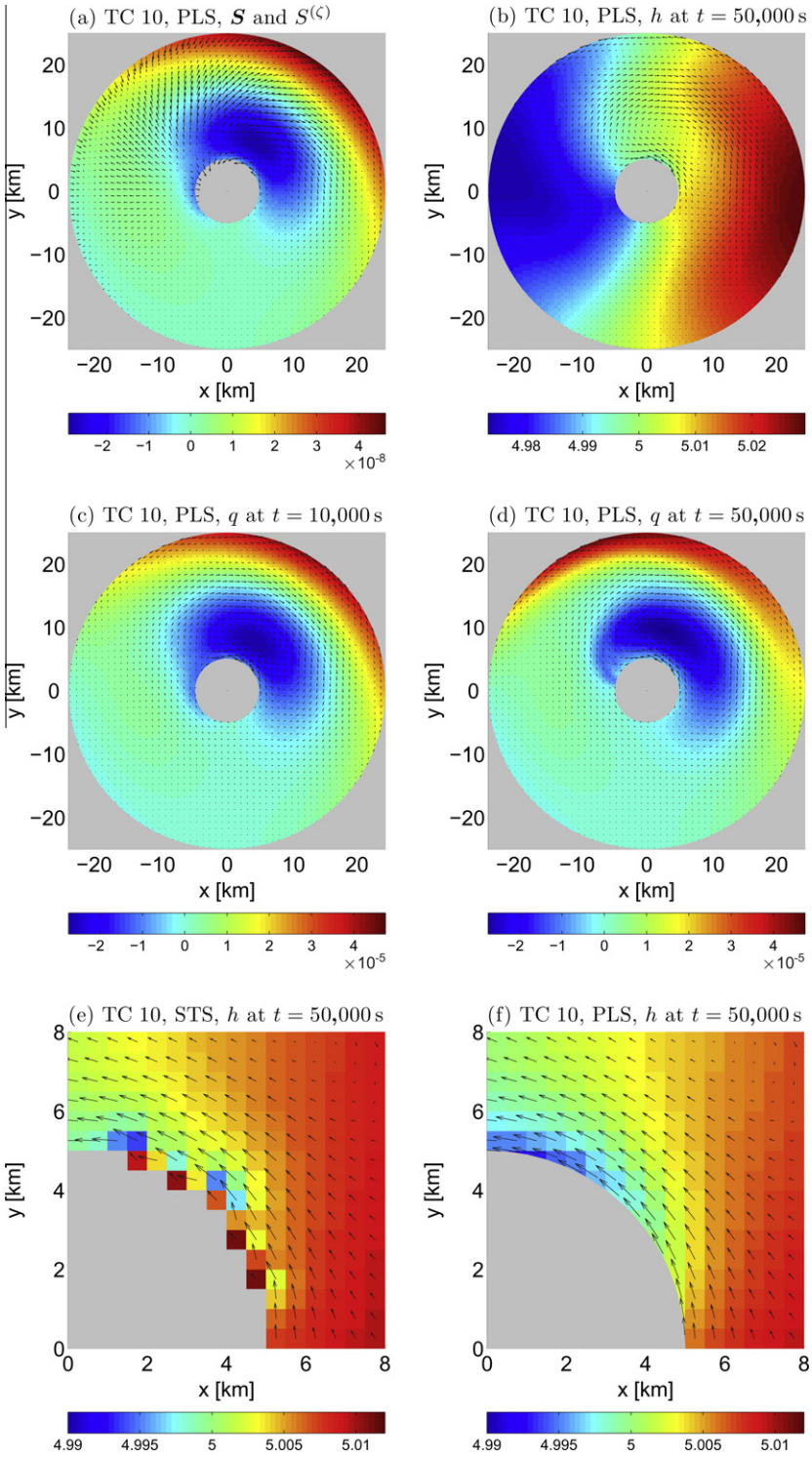

Fig. 10. Various fields from TC 10 (forced flow) on the $\Delta x = \Delta y = 500$ m grid. (a) Stress vector field $\boldsymbol{S}$ (in $m^2\ s^{-2}$) and vorticity source term $S^{(\zeta)}$ (in s^{-2}) given by Eqs. (85)–(87) with $T(t)$ set to 1, shown here for the PLS; (b) fluid depth h (in m) and velocities at $t = 50{,}000$ s from the PLS; (c) potential vorticity q (in $m^{-1}\ s^{-1}$) and velocities at $t = 10{,}000$ s (which corresponds to about the end of the forcing period) from the PLS; (d) q and velocities at $t = 50{,}000$ s from the PLS; (e) h and velocities at $t = 50{,}000$ s from the STS near the inner boundary of the northeastern quarter of the annulus; and (f) h and velocities at $t = 50{,}000$ s from the PLS near the inner boundary of the northeastern quarter of the annulus. For clarity, vectors in (a)–(d) are shown at only every second grid point. The maximum stress magnitude in (a) is $6.1 \times 10^{-4}\ m^2\ s^{-2}$. The maximum velocity magnitudes are 0.64 m s^{-1} in (b), (d), and (f) and 0.63 m s^{-1} in (c) and (e). Panels (c) and (d) use the same vector length scale and color scale, as do panels (e) and (f). For plotting purposes, u, v, and q have been interpolated from u-, v-, and ζ-points to h-points (Appendix C). Rates of convergence are listed in Table 4.

In cylindrical coordinates, we obtain the source term in the discrete flux-form vorticity equation (32) at the boundary ζ-point at $(i+1/2, j+1/2)$ by evaluating (87) at $(\xi_{i+1/2}, \eta_{j+1/2}) = (r_{i+1/2}, \theta_{j+1/2})$ and multiplying the result by the associated area $A^{(\zeta)}_{i+1/2,j+1/2}$.

In Cartesian coordinates, we initiate motion using the forcing functions $S_\xi/mh = S_x/h$ and $S_\eta/nh = S_y/h$ on the RHSs of the x and y direction momentum equations (2) and (3). The Cartesian stress components S_x and S_y are obtained using

$$S_x = S_r(r,\theta,t)\cos\theta - S_\theta(r,\theta,t)\sin\theta \tag{88}$$

$$S_y = S_r(r,\theta,t)\sin\theta + S_\theta(r,\theta,t)\cos\theta \tag{89}$$

where S_r and S_θ are given by (85) and (86), and r and θ are calculated from x and y using (84). As in cylindrical coordinates, we obtain the source term in the discrete flux-form vorticity equation at the boundary ζ-point at $(i+1/2, j+1/2)$ by evaluating (87) at $(\xi_{i+1/2}, \eta_{j+1/2}) = (x_{i+1/2}, y_{j+1/2})$ [with r and θ in (87) obtained from $x_{i+1/2}$ and $y_{j+1/2}$ using (84)] and multiplying the result by the area $A^{(\zeta)}_{i+1/2,j+1/2}$. Panel (a) of Fig. 10 shows the stress vector field $\boldsymbol{S}$ given by (85) and (86) or (88) and (89) and the corresponding vorticity source term $S^{(\zeta)}$ given by (87) on the 500 m Cartesian grid. Note that in the figure, $\boldsymbol{S}$ and $S^{(\zeta)}$ are shown at their maximum values in time, i.e. with $T(t)$ set to 1.

Since the forcing in this TC is nonzero near boundaries, the PLS and UNPLS are no longer equivalent. Thus, as in TCs 1–6, in this TC we perform three GRSs—one with the STS, a second with the PLS, and a third with the UNPLS. We integrate this TC to $t = 50{,}000$ s in order to give the flow sufficient time to evolve on its own after the forcing stops (at $t \approx 10{,}000$ s). Panel (b) of Fig. 10 shows the depth and velocity fields at $t = 50{,}000$ s, and panels (c) and (d) show the potential vorticity and velocity fields at $t = 10{,}000$ s and $t = 50{,}000$ s, respectively. All three panels are for the PLS on the 500 m grid. Comparing panels (c) and (d), we can see that between the end of the forcing and the end of the simulation, the potential vorticity gets advected around both the inner and outer boundaries of the annulus. Thus, the flow interacts strongly with the boundaries.

Table 4 lists the convergence rates of the error norms of h, u, v, ζ, and q for all three schemes for TC 10. We can see from this table that the convergence rates for h, u, and v are about 1 order larger for the PLS and UNPLS than for the STS. The L_1 and L_2 error norms of h, u, and v converge faster for the PLS and UNPLS than for the STS because as we move from coarser to finer grids, the model boundaries in the PLS and UNPLS shift much less than in the STS. (This is also the reason for the higher convergence rates of the L_1 and L_2 error norms of h, u, and v for the PLS and UNPLS in all the other TCs, including TCs 1–6.) This is in turn due to the fact that the boundary profile on any given grid is much more accurately approximated with the PLS and UNPLS than with the STS. Panels (e) and (f) of Fig. 10 show the depth and velocity fields for the STS and PLS, respectively, near the inner boundary of the northeastern quarter of the annulus on the 500 m grid at $t = 50{,}000$ s. (The corresponding figure for the UNPLS is indistinguishable from the one for the PLS and is therefore not shown.) We can see from this figure that h, u, and v near the boundary are jagged for the STS but are smooth for the PLS (and UNPLS). The jaggedness in the STS fields comes about because the fluid velocity must change both its magnitude and direction abruptly to get around the steps. To get around convex corners, the flow accelerates, giving rise to large velocities and minima (depressions) in the depth. On the other hand, at concave corners, the flow slows down and the fluid piles up, giving rise to maxima in the depth. Note that the jaggedness in h, u, and v near boundaries in the STS does not disappear as the grid is refined. This is because even though the size of the boundary steps decreases with decreasing grid size, the steps themselves never go away. As a result, h, u, and v near stairstep boundaries do not converge to those near a smooth (in this case circular) boundary even as the flow far from the boundary converges to the exact solution. This is reflected in the fact that the L_∞ error norms of h, u, and v for the STS have convergence rates of 0. [Recall that $\|\Delta u\|_\infty$ and $\|\Delta v\|_\infty$ for the STS also fail to converge in TCs 1–8. However, $\|\Delta h\|_\infty$ for the STS converges in some of these TCs (3, 6, 7, and 8) but not others (1, 2, 4, and 5). We have not been able to determine the circumstances under which $\|\Delta h\|_\infty$ for the STS converges or fails to converge. On the other hand, $\|\Delta h\|_\infty$, $\|\Delta u\|_\infty$, and $\|\Delta v\|_\infty$ for the PLS and UNPLS converge in all of TCs 1–8 and TC 10.]

We can also see from Table 4 that the PLS simulates h with the same accuracy as the UNPLS, and it simulates u and v slightly more accurately (by 0.1–0.2 order). Also, the STS and UNPLS simulate ζ and q with about the same accuracy while the PLS simulates it more accurately by about 0.5 order. (Note that ζ and q behave almost identically in this TC because the relative changes in h in any of the simulations are much smaller than the relative changes in ζ. Thus, $q = \zeta/h \approx \zeta/h_o = \zeta/5$ m, and any conclusions drawn here about the error norms of ζ also apply to the error norms of q.) Most notably, $\|\Delta\zeta\|_\infty$ (representing the error in ζ at or near boundaries) converges at a rate of 0.4–0.6 for the PLS but does not converge for the STS and UNPLS. This result demonstrates that the evaluation of the forcing terms at the shifted locations in the PLS is indeed effective in increasing the accuracy of the scheme. This procedure allows ζ near boundaries to converge. This in turn helps improve the convergence rates of $\|\Delta\zeta\|_1$ and $\|\Delta\zeta\|_2$ (which are 0.9 and 0.5 for the UNPLS and 1.5 and 1.2 for the PLS) as well as the convergence rates of all three error norms of u and v (by 0.1–0.2 order). Thus, it is clear in this TC that the PLS is the most accurate of the three boundary schemes.

8. Conclusion

We have presented a new boundary scheme for use with the mass, energy, vorticity, and potential enstrophy conserving scheme of Arakawa and Lamb [2] for the inviscid shallow water equations that uses piecewise linear line segments to

approximate boundary profiles. The new boundary scheme is a generalization of a previous scheme that uses stairsteps to approximate boundary profiles [1]. Here, we refer to the new piecewise linear scheme as the PLS and the previous stairstep scheme as the STS. Both boundary schemes maintain all four conservation properties of the original Arakawa and Lamb scheme [2] for unbounded flows.

We have performed numerical tests to compare the conservation properties and accuracy of the PLS with those of the STS. The conservation tests demonstrated that, like the STS, the PLS conserves the domain-summed mass and vorticity to within roundoff error and the domain-summed energy and potential enstrophy to within time integration errors. The accuracy tests involved performing grid refinement studies (GRSs) and observing the rates of convergence of the L_1, L_2, and L_∞ error norms of h, u, v, ζ, and q with decreasing grid size. We performed these GRSs on a total of ten test cases. The first six of these were channels flows (for which analytic solutions are available), and the last four were annulus flows (for which analytic solutions are not available, so we obtained the "exact" solutions by performing simulations in cylindrical coordinates on highly refined grids). To demonstrate that the use of the shifted locations in the PLS is effective in improving the accuracy of the model, for each test case we ran GRSs not only with the STS and PLS but also with a version of the piecewise linear scheme which we refer to as the UNPLS that does not make use of the shifted locations, i.e. it evaluates the initial velocity components and the forcing terms exactly at (the unshifted) u- and v-points. The GRSs of the ten test cases with the STS, PLS, and UNPLS yielded the following accuracy results:

1. The PLS simulates h, u, and v more accurately than the STS by 0.5–1 order. For the PLS, h, u, and v near boundaries always converge (as measured by the convergence rates of their L_∞ error norms). For the STS, u and v near boundaries never converge while h near boundaries converges in some test cases but not others.
2. In some test cases, the PLS simulates ζ and q about as accurately as the STS while in other cases, it simulates ζ and q more accurately (e.g. by 0.5 order). In none of the test cases does the STS simulate ζ and/or q significantly more accurately (i.e. by more than 0.2 order) than the PLS.
3. The UNPLS simulates h as accurately as the PLS but simulates u and v somewhat less accurately than the PLS (but still more accurately than the STS). Just as for the PLS, h, u, and v near boundaries always converge for the UNPLS.
4. In most test cases, the PLS simulates ζ and q much more accurately (e.g. by 1 order) than the UNPLS. In fact, in most cases, ζ and q near boundaries do not converge for the UNPLS, but they converge in all cases for the PLS. This shows that the use of the shifted locations in the PLS allows ζ and q near boundaries to converge (which in turn helps increase the convergence rates of u and v).
5. The only one of the three boundary schemes for which all five of the quantities h, u, v, ζ, and q converge near boundaries in all test cases is the PLS.

Given these accuracy results and the fact that the STS, PLS, and UNPLS conserve the domain-summed mass, energy, vorticity, and potential enstrophy equally well (note that the use of the shifted locations has no effect on conservation properties, so the PLS and UNPLS conserve the same four domain-summed quantities), we conclude that the PLS is superior to the STS and UNPLS. (The STS was in turn shown in KJ09 to be an improvement over several other non-conserving stairstep boundary schemes). We plan to generalize the PLS to the equations governing 3D atmospheric and oceanic flows.

Acknowledgments

This research was supported by the Precourt Institute for Energy Efficiency, the Department of the Army Center at Stanford University, and the Environmental Protection Agency. We would like to thank two anonymous reviewers for their valuable comments and suggestions.

Appendix A. Derivation of $A_{i,j}^{(h)}$ at boundary h-points

In this appendix, we derive an expression for the area $A_{i,j}^{(h)}$ associated with a boundary h-point (which exist only in the PLS). We will choose $A_{i,j}^{(h)}$ at such points so that the discrete expression for $K_{i,j}$ given by (20) converges to the correct limit as the grid is refined and the boundary h-point approaches the fluid–land boundary.

Let (ξ_B, η_B) denote the coordinates of some point, say point B, on a fluid–land boundary in the $\xi\eta$ plane (Fig. 4). In the analysis below, we will use the following limiting process. We will keep the location of B fixed, and we will consider progressively finer grids, focusing on each grid on the specific boundary box that happens to encompass point B. In the limit of an infinitely refined grid, the area of the boundary box will go to zero, and the h-point associated with the box, the two u-points on its eastern and western faces, and the two v-points on its northern and southern faces will all converge to point B (whether these u- and v-points are fluid or land).

On a given grid, let $(\xi_{i,j}^{(h)}, \eta_{i,j}^{(h)})$ denote the coordinates of the boundary h-point associated with the boundary box that happens to encompass point B. From (20), $K_{i,j}$ at this h-point is given by

$$K_{i,j} = \frac{1}{A_{i,j}^{(h)}} \frac{1}{2} \left[\overline{A^{(u)} u^2}^{\xi} + \overline{A^{(v)} v^2}^{\eta} \right]_{i,j} \tag{90}$$

Expanding the averaging operators on the RHS, we get

$$K_{i,j} = \frac{1}{4A_{i,j}^{(h)}}\left[(A^{(u)}u^2)_{i+1/2,j} + (A^{(u)}u^2)_{i-1/2,j} + (A^{(v)}v^2)_{i,j+1/2} + (A^{(v)}v^2)_{i,j-1/2}\right] \tag{91}$$

Since $(\xi_{i,j}^{(h)}, \eta_{i,j}^{(h)})$ approaches point B as we consider progressively finer grids, in the limit of infinite grid refinement the RHS of (91) must converge to the value of K at point B. To obtain this value, we first express the ξ and η velocity components u and v as follows:

$$u = U\cos\alpha \tag{92}$$
$$v = U\sin\alpha \tag{93}$$

Here, U is the magnitude of the velocity and $\alpha = \tan^{-1}(v/u)$ is its direction. Recall from Section 2 that in the continuous case, K is given by

$$K = \frac{1}{2}(u^2 + v^2)$$

Substituting (92) and (93) into this, we get

$$K = \frac{1}{2}[(U\cos\alpha)^2 + (U\sin\alpha)^2] = \frac{1}{2}U^2$$

Evaluating this at point B, we obtain

$$K_B = \frac{1}{2}U_B^2 \tag{94}$$

where U_B is the velocity magnitude at point B. This is the value that $K_{i,j}$ must converge to as we consider progressively finer grids. To determine the conditions under which this requirement is satisfied, we must first express the RHS of (91) in terms of U_B. This requires that we first express u and v in terms of U_B. To obtain such expressions, it will be convenient to first expand U and α in terms of the separations in the ξ and η directions between point B and some generic point (ξ,η) within the fluid. We will denote these separations by X and Y, i.e.

$$X = \xi - \xi_B; \quad Y = \eta - \eta_B \tag{95}$$

For small X and Y [i.e. as the generic point (ξ,η) approaches B], we can expand U and α about (ξ_B,η_B) to first order in X and Y as follows:

$$U = U_B + a_1X + a_2Y \tag{96}$$
$$\alpha = \alpha_B + b_1X + b_2Y \tag{97}$$

Here, U_B, a_1, a_2, α_B, b_1, and b_2 are (generally time-dependent) coefficients that are not functions of ξ and η (or X and Y). [We do not include bilinear terms, e.g. a_3XY and b_3XY, on the RHSs of (96) and (97) because these are effectively second-order terms. This is due to the fact that we are refining the grid in both the ξ and η directions, so X and Y go to zero simultaneously. The results obtained in this appendix are the same whether or not we include these terms.] Note that (96) satisfies the requirement that $U = U_B$ at point B (i.e. when $X = Y = 0$). Also, α_B is the value of α at point B. We must now substitute (96) and (97) into the RHSs of (92) and (93). First, however, we use trigonometric identities to rewrite $\cos\alpha$ and $\sin\alpha$ as follows:

$$\cos\alpha = \cos[(\alpha-\alpha_B)+\alpha_B] = \cos(\alpha-\alpha_B)\cos\alpha_B - \sin(\alpha-\alpha_B)\sin\alpha_B \tag{98}$$
$$\sin\alpha = \sin[(\alpha-\alpha_B)+\alpha_B] = \sin(\alpha-\alpha_B)\cos\alpha_B + \cos(\alpha-\alpha_B)\sin\alpha_B \tag{99}$$

For convenience, we define the angle β as follows:

$$\beta = b_1X + b_2Y \tag{100}$$

Note that β is first order in X and Y. Thus, it goes to zero as X and Y go to zero. Substituting (100) into (97), we get

$$\alpha - \alpha_B = \beta \tag{101}$$

Using (101), we can rewrite (98) and (99) as follows:

$$\cos\alpha = \cos\alpha_B\cos\beta - \sin\alpha_B\sin\beta$$
$$\sin\alpha = \cos\alpha_B\sin\beta + \sin\alpha_B\cos\beta$$

Substituting these into (92) and (93), we get

$$u = (\cos\alpha_B\cos\beta - \sin\alpha_B\sin\beta)U \tag{102}$$
$$v = (\cos\alpha_B\sin\beta + \sin\alpha_B\cos\beta)U \tag{103}$$

We now keep only those terms on the RHSs of (102) and (103) that are zeroth- or first-order in X or Y. For small $|\beta|$, the series expansions for $\cos\beta$ and $\sin\beta$ are given by

$$\cos\beta = 1 - \frac{1}{2}\beta^2 + \cdots; \quad \sin\beta = \beta - \frac{1}{6}\beta^3 + \cdots$$

Substituting these into (102) and (103) and keeping only terms that are zeroth- or first- order in β, we obtain

$$u = (\cos\alpha_B - \beta\sin\alpha_B)U$$
$$v = (\beta\cos\alpha_B + \sin\alpha_B)U$$

Substituting in (96) and (100), we can rewrite these as

$$u = [\cos\alpha_B - (b_1X + b_2Y)\sin\alpha_B](U_B + a_1X + a_2Y)$$
$$v = [(b_1X + b_2Y)\cos\alpha_B + \sin\alpha_B](U_B + a_1X + a_2Y)$$

Carrying out the multiplications on the RHSs and retaining only zeroth- and first-order terms in X and Y, we obtain

$$u = U_B\cos\alpha_B + (a_1\cos\alpha_B - U_Bb_1\sin\alpha_B)X + (a_2\cos\alpha_B - U_Bb_2\sin\alpha_B)Y$$
$$v = U_B\sin\alpha_B + (a_1\sin\alpha_B + U_Bb_1\cos\alpha_B)X + (a_2\sin\alpha_B + U_Bb_2\cos\alpha_B)Y$$

These are the required expressions for u and v in terms of U_B [and the other coefficients on the RHSs of (96) and (97)]. Squaring these and again retaining only zeroth- and first-order terms in X and Y, we get

$$u^2 = (U_B\cos\alpha_B)^2 + 2U_B\cos\alpha_B(a_1\cos\alpha_B - U_Bb_1\sin\alpha_B)X + 2U_B\cos\alpha_B(a_2\cos\alpha_B - U_Bb_2\sin\alpha_B)Y \tag{104}$$

$$v^2 = (U_B\sin\alpha_B)^2 + 2U_B\sin\alpha_B(a_1\sin\alpha_B + U_Bb_1\cos\alpha_B)X + 2U_B\sin\alpha_B(a_2\sin\alpha_B + U_Bb_2\cos\alpha_B)Y \tag{105}$$

These expressions are valid for small X and Y. Evaluating (104) at the u-points on the eastern and western faces of the boundary box at (i,j) [i.e. at $(\xi_{i+1/2}, \eta^{(u)}_{i+1/2,j})$ and $(\xi_{i-1/2}, \eta^{(u)}_{i-1/2,j})$], we obtain

$$u^2_{i+1/2,j} = (U_B\cos\alpha_B)^2 + 2U_B\cos\alpha_B(a_1\cos\alpha_B - U_Bb_1\sin\alpha_B)X_{i+1/2} + 2U_B\cos\alpha_B(a_2\cos\alpha_B - U_Bb_2\sin\alpha_B)Y^{(u)}_{i+1/2,j} \tag{106}$$

$$u^2_{i-1/2,j} = (U_B\cos\alpha_B)^2 + 2U_B\cos\alpha_B(a_1\cos\alpha_B - U_Bb_1\sin\alpha_B)X_{i-1/2} + 2U_B\cos\alpha_B(a_2\cos\alpha_B - U_Bb_2\sin\alpha_B)Y^{(u)}_{i-1/2,j} \tag{107}$$

where $(X_{i+1/2}, Y^{(u)}_{i+1/2,j})$ and $(X_{i-1/2}, Y^{(u)}_{i-1/2,j})$ are the X and Y values at these u-points and are given by

$$X_{i+1/2} = \xi_{i+1/2} - \xi_B; \quad Y^{(u)}_{i+1/2,j} = \eta^{(u)}_{i+1/2,j} - \eta_B \tag{108}$$
$$X_{i-1/2} = \xi_{i-1/2} - \xi_B; \quad Y^{(u)}_{i-1/2,j} = \eta^{(u)}_{i-1/2,j} - \eta_B \tag{109}$$

Similarly, evaluating (105) at the v-points on the northern and southern faces of the boundary box at (i,j) [i.e. at $(\xi^{(v)}_{i,j+1/2}, \eta_{j+1/2})$ and $(\xi^{(v)}_{i,j-1/2}, \eta_{j-1/2})$], we obtain

$$v^2_{i,j+1/2} = (U_B\sin\alpha_B)^2 + 2U_B\sin\alpha_B(a_1\sin\alpha_B + U_Bb_1\cos\alpha_B)X^{(v)}_{i,j+1/2} + 2U_B\sin\alpha_B(a_2\sin\alpha_B + U_Bb_2\cos\alpha_B)Y_{j+1/2} \tag{110}$$

$$v^2_{i,j-1/2} = (U_B\sin\alpha_B)^2 + 2U_B\sin\alpha_B(a_1\sin\alpha_B + U_Bb_1\cos\alpha_B)X^{(v)}_{i,j-1/2} + 2U_B\sin\alpha_B(a_2\sin\alpha_B + U_Bb_2\cos\alpha_B)Y_{j-1/2} \tag{111}$$

where $(X^{(v)}_{i,j+1/2}, Y_{j+1/2})$ and $(X^{(v)}_{i,j-1/2}, Y_{j-1/2})$ are the X and Y values at these v-points and are given by

$$X^{(v)}_{i,j+1/2} = \xi^{(v)}_{i,j+1/2} - \xi_B; \quad Y_{j+1/2} = \eta_{j+1/2} - \eta_B \tag{112}$$
$$X^{(v)}_{i,j-1/2} = \xi^{(v)}_{i,j-1/2} - \xi_B; \quad Y_{j-1/2} = \eta_{j-1/2} - \eta_B \tag{113}$$

Note that in obtaining (106), (107), (110) and (111), we have assumed that $(i+1/2,j)$ and $(i-1/2,j)$ are fluid u-points and $(i,j+1/2)$ and $(i,j-1/2)$ are fluid v-points. (This is the case that is illustrated in Fig. 4.) However, as we move to finer grids, these u- and v-points can alternate between being fluid and land (although at least one of these u-points and at least one of these v-points will always be fluid). Fortunately, in this analysis, it does not matter what we set $u^2_{i+1/2,j}$ and $v^2_{i,j+1/2}$ to at land u- and v-points because at such points, $u^2_{i+1/2,j}$ and $v^2_{i,j+1/2}$ will be multiplied by $A^{(u)}_{i+1/2,j}$ and $A^{(v)}_{i,j+1/2}$ [see (91)], which will be zero (Section 4.1). Thus, we can use (106), (107), (110) and (111) in our analysis whether or not the corresponding u- and v-points are fluid or land. Substituting (106), (107), (110) and (111) into (91) and rearranging terms, we obtain

$$
\begin{aligned}
K_{i,j} = {} & U_B^2 \frac{1}{4A_{i,j}^{(h)}} \left[\cos^2\alpha_B \left(A_{i+1/2,j}^{(u)} + A_{i-1/2,j}^{(u)} \right) + \sin^2\alpha_B \left(A_{i,j+1/2}^{(v)} + A_{i,j-1/2}^{(v)} \right) \right] \\
& + 2U_B a_1 \frac{1}{4A_{i,j}^{(h)}} \left[\cos^2\alpha_B \left(A_{i+1/2,j}^{(u)} X_{i+1/2} + A_{i-1/2,j}^{(u)} X_{i-1/2} \right) + \sin^2\alpha_B \left(A_{i,j+1/2}^{(v)} X_{i,j+1/2}^{(v)} + A_{i,j-1/2}^{(v)} X_{i,j-1/2}^{(v)} \right) \right] \\
& + 2U_B a_2 \frac{1}{4A_{i,j}^{(h)}} \left[\cos^2\alpha_B \left(A_{i+1/2,j}^{(u)} Y_{i+1/2,j}^{(u)} + A_{i-1/2,j}^{(u)} Y_{i-1/2,j}^{(u)} \right) + \sin^2\alpha_B \left(A_{i,j+1/2}^{(v)} Y_{j+1/2} + A_{i,j-1/2}^{(v)} Y_{j-1/2} \right) \right] \\
& - 2U_B^2 b_1 \frac{1}{4A_{i,j}^{(h)}} \cos\alpha_B \sin\alpha_B \left[\left(A_{i+1/2,j}^{(u)} X_{i+1/2} + A_{i-1/2,j}^{(u)} X_{i-1/2} \right) - \left(A_{i,j+1/2}^{(v)} X_{i,j+1/2}^{(v)} + A_{i,j-1/2}^{(v)} X_{i,j-1/2}^{(v)} \right) \right] \\
& - 2U_B^2 b_2 \frac{1}{4A_{i,j}^{(h)}} \cos\alpha_B \sin\alpha_B \left[\left(A_{i+1/2,j}^{(u)} Y_{i+1/2,j}^{(u)} + A_{i-1/2,j}^{(u)} Y_{i-1/2,j}^{(u)} \right) - \left(A_{i,j+1/2}^{(v)} Y_{j+1/2} + A_{i,j-1/2}^{(v)} Y_{j-1/2} \right) \right]
\end{aligned} \tag{114}
$$

We now take the limit of this expression as we consider progressively finer grids. In this limit, the areas $A_{i,j}^{(h)}$, $A_{i+1/2,j}^{(u)}$, $A_{i-1/2,j}^{(u)}$, $A_{i,j+1/2}^{(v)}$, and $A_{i,j-1/2}^{(v)}$ all go to zero. We will assume here that the ratios of $A_{i+1/2,j}^{(u)}$, $A_{i-1/2,j}^{(u)}$, $A_{i,j+1/2}^{(v)}$, and $A_{i,j-1/2}^{(v)}$ to $A_{i,j}^{(h)}$ remain finite. We will verify this assumption later below after we derive the expression for $A_{i,j}^{(h)}$ at a boundary h-point. Note that $X_{i+1/2}$, $Y_{i+1/2,j}^{(u)}$, $X_{i-1/2}$, $Y_{i-1/2,j}^{(u)}$, $X_{i,j+1/2}^{(v)}$, $Y_{j+1/2}$, $X_{i,j-1/2}^{(v)}$, and $Y_{j-1/2}$ also go to zero as we consider progressively finer grids. Thus, the terms involving X and Y on the RHS of (114) go to zero in this limit and we obtain

$$
K_{i,j} \to U_B^2 \frac{1}{4A_{i,j}^{(h)}} \left[\cos^2\alpha_B \left(A_{i+1/2,j}^{(u)} + A_{i-1/2,j}^{(u)} \right) + \sin^2\alpha_B \left(A_{i,j+1/2}^{(v)} + A_{i,j-1/2}^{(v)} \right) \right] \quad \text{as we consider progressively finer grids} \tag{115}
$$

Recall that the correct limit for $K_{i,j}$ is given by the RHS of (94). Thus, we now require that the RHS of (115) approach that of (94), i.e.

$$
U_B^2 \frac{1}{2A_{i,j}^{(h)}} \left[\cos^2\alpha_B \overline{(A^{(u)})}_{i,j}^{\xi} + \sin^2\alpha_B \overline{(A^{(v)})}_{i,j}^{\eta} \right] \to \frac{1}{2} U_B^2 \quad \text{as we consider progressively finer grids} \tag{116}
$$

Note that we have used the numerical averaging operators to rewrite the terms involving $A_{i+1/2,j}^{(u)}$ and $A_{i,j+1/2}^{(v)}$ in (116) more compactly. (116) is equivalent to requiring that

$$
A_{i,j}^{(h)} \to \left[\overline{A^{(u)}}^{\xi} \cos^2\alpha_B + \overline{A^{(v)}}^{\eta} \sin^2\alpha_B \right]_{i,j} \quad \text{as we consider progressively finer grids} \tag{117}
$$

Recall that α_B is the value of the velocity angle α at the boundary point B. Since the velocity vector at the boundary must be tangent to the boundary, α_B must equal $\theta_{\text{bdy},B}$ or $\theta_{\text{bdy},B} \pm \pi$, where $\theta_{\text{bdy},B}$ is the angle in physical space that the boundary makes with a curve of constant η passing through point B (see Fig. 4 and the more detailed description of θ_{bdy} given in Section 4.2). Thus,

$$
\cos^2\alpha_B = \cos^2\theta_{\text{bdy},B}; \quad \sin^2\alpha_B = \sin^2\theta_{\text{bdy},B} \tag{118}
$$

Substituting these into (117), we obtain the following requirement on $A_{i,j}^{(h)}$ at boundary h-points:

$$
A_{i,j}^{(h)} \to \left[\overline{A^{(u)}}^{\xi} \cos^2\theta_{\text{bdy},B} + \overline{A^{(v)}}^{\eta} \sin^2\theta_{\text{bdy},B} \right]_{i,j} \quad \text{as we consider progressively finer grids} \tag{119}
$$

To satisfy this, we now set $A_{i,j}^{(h)}$ at boundary h-points as follows:

$$
A_{i,j}^{(h)} = \left[\overline{A^{(u)}}^{\xi} \cos^2\theta_{\text{bdy}} + \overline{A^{(v)}}^{\eta} \sin^2\theta_{\text{bdy}} \right]_{i,j} \tag{120}
$$

Here, $\theta_{\text{bdy},i,j}$ is the angle in physical space that the linear boundary segment within the boundary box at (i,j) makes with a curve of constant η. Note that as we consider progressively finer grids, $\theta_{\text{bdy},i,j}$ converges to $\theta_{\text{bdy},B}$ because in this limit, the curvature of the boundary can be ignored. Thus, the RHS of (120) converges to that of (119). Eq. (120) is the expression we use in calculating $A_{i,j}^{(h)}$ at boundary h-points.

Now that we have derived the expression for $A_{i,j}^{(h)}$ at boundary h-points, we can confirm the assumption made above that the limits of the ratios of $A_{i+1/2,j}^{(u)}$, $A_{i-1/2,j}^{(u)}$, $A_{i,j+1/2}^{(v)}$, and $A_{i,j-1/2}^{(v)}$ to $A_{i,j}^{(h)}$ remain finite as we consider progressively finer grids. Since $A_{i,j}^{(h)}$ given by (120) satisfies (119), we will simply work with (119). Substituting (118) into (119) and expanding the numerical averaging operators, we obtain

$$
\begin{aligned}
A_{i,j}^{(h)} \to {} & \frac{1}{2} A_{i+1/2,j}^{(u)} \cos^2\alpha_B + \frac{1}{2} A_{i-1/2,j}^{(u)} \cos^2\alpha_B + \frac{1}{2} A_{i,j+1/2}^{(v)} \sin^2\alpha_B + \frac{1}{2} A_{i,j-1/2}^{(v)} \sin^2\alpha_B \\
& \text{as we consider progressively finer grids}
\end{aligned} \tag{121}
$$

Since the box at (i,j) is a boundary box, at least one of $A_{i+1/2,j}^{(u)}$ and $A_{i-1/2,j}^{(u)}$ and at least one of $A_{i,j+1/2}^{(v)}$ and $A_{i,j-1/2}^{(v)}$ is positive, and all four of these areas are always nonnegative. Also, $\cos^2\alpha_B$ and $\sin^2\alpha_B$ cannot both be zero; at least one of them must be po-

sitive. Thus, each of the four terms on the RHS of (121) is nonnegative, and at least one is always positive. This implies that each of the four terms is greater than or equal to zero and less than or equal to their sum. Consider, for instance, the first term on the RHS of (121). From the argument above, we have

$$0 \leqslant \frac{1}{2}A^{(u)}_{i+1/2,j}\cos^2\alpha_B \leqslant \frac{1}{2}A^{(u)}_{i+1/2,j}\cos^2\alpha_B + \frac{1}{2}A^{(u)}_{i-1/2,j}\cos^2\alpha_B + \frac{1}{2}A^{(v)}_{ij+1/2}\sin^2\alpha_B + \frac{1}{2}A^{(v)}_{ij-1/2}\sin^2\alpha_B \tag{122}$$

Dividing this by $A^{(h)}_{ij}$ (which is always positive), taking the limit as we consider progressively finer grids, and substituting in (121), we get

$$0 \leqslant \frac{1}{2}\frac{A^{(u)}_{i+1/2,j}}{A^{(h)}_{ij}}\cos^2\alpha_B \leqslant 1 \quad \text{as we consider progressively finer grids} \tag{123}$$

If $\cos\alpha_B$ is zero, then all terms on the RHS of (114) involving the ratio of $A^{(u)}_{i+1/2,j}$ to $A^{(h)}_{ij}$ drop out and we do not have to worry about whether this ratio remains finite as we consider progressively finer grids. Thus, in (123), we only need to consider the case of $\cos\alpha_B$ being nonzero. Then $\cos^2\alpha_B$ is positive, so we can rewrite (123) as

$$0 \leqslant \frac{A^{(u)}_{i+1/2,j}}{A^{(h)}_{ij}} \leqslant \frac{2}{\cos^2\alpha_B} \quad \text{as we consider progressively finer grids} \tag{124}$$

Since the RHS of (124) is a constant, we see that $A^{(u)}_{i+1/2,j}/A^{(h)}_{ij}$ remains finite, as assumed in the derivation above. We can use analogous procedures to show that the ratios of $A^{(u)}_{i-1/2,j}$, $A^{(v)}_{ij+1/2}$, and $A^{(v)}_{ij-1/2}$ to $A^{(h)}_{ij}$ also remain finite as we consider progressively finer grids.

Appendix B. Derivation of the shifted coordinates $\xi^{(v)*}_{ij+1/2}$ and $\eta^{(u)*}_{i+1/2j}$

In this appendix, we show that if in the piecewise linear scheme the forcing terms $[\Delta s^{(u)*}_{\xi}(S_\xi/h)^*]_{i+1/2,j}$ and $[\Delta s^{(v)*}_{\eta}(S_\eta/h)^*]_{ij+1/2}$ in the discrete momentum equations (18) and (19) at near-boundary u- and v-points are evaluated exactly where u and v are defined, then the vorticity source term $S^{(\zeta)}_{i+1/2,j+1/2}$ in the discrete vorticity equation (32) at near-boundary ζ-points will not converge to the correct limit as the grid is refined. We then derive the (ξ,η) coordinates of the locations where the forcing terms must be evaluated in order for $S^{(\zeta)}_{i+1/2,j+1/2}$ at near-boundary ζ-points to converge to the correct limit. Recall from Section 4.4 that near-boundary u- and v-points are fluid u- and v-points that are surrounded by one or (at most) two boundary boxes, and near-boundary ζ-points are fluid ζ-points that are surrounded by one or more (but at most four) boundary boxes. In Figs. 3 and 4, near-boundary ζ-points are denoted by "×"s within diamonds. Note that near-boundary ζ-points are always located on one of the corners of a boundary box. Thus, as the grid is refined, they approach the fluid–land boundary.

To demonstrate that $S^{(\zeta)}_{i+1/2,j+1/2}$ at near-boundary ζ-points does not converge to the correct limit if the forcing terms at near-boundary u- and v-points are evaluated exactly where u and v are defined, we consider as simple a case as possible. Thus, we use Cartesian coordinates $(\xi,\eta) = (x,y)$ with $m = n = 1$, and we assume the stress components are given by

$$S_x = 0 \quad \text{and} \quad S_y = (\alpha + \beta x)h \tag{125}$$

where α and β are arbitrary constants. Then the forcing terms in the continuous momentum equations (2) and (3) are given by

$$\frac{S_\xi}{mh} = \frac{S_x}{h} = 0 \quad \text{and} \quad \frac{S_\eta}{nh} = \frac{S_y}{h} = \alpha + \beta x \tag{126}$$

From (11), the corresponding exact expression for $S^{(\zeta)}$ is

$$S^{(\zeta)} = \frac{\partial}{\partial x}\left(\frac{S_y}{h}\right) - \frac{\partial}{\partial y}\left(\frac{S_x}{h}\right) = \beta \tag{127}$$

We will now evaluate the discrete expression for $S^{(\zeta)}_{i+1/2,j+1/2}$ given by (35) at the near-boundary ζ-point at $(i+1/2, j+1/2)$ in Fig. 11, and we will then check whether its limit as the grid is refined (and the near-boundary ζ-point approaches the boundary) corresponds to the RHS of (127). In Fig. 11, we have assumed for simplicity that the boundary is linear and passes exactly through the boundary ζ-points at $(i+1/2, j-1/2)$ and $(i+3/2, j+1/2)$. Thus, the coordinates of the u-points at $(i+1/2, j)$ and $(i+1/2, j+1)$ are $(\xi_{i+1/2}, \eta^{(u)}_{i+1/2,j}) = (x_{i+1/2}, y_j)$ and $(\xi_{i+1/2}, \eta^{(u)}_{i+1/2,j+1}) = (x_{i+1/2}, y_{j+1})$, respectively, and the coordinates of the v-points at $(i, j+1/2)$ and $(i+1, j+1/2)$ are $(\xi^{(v)}_{ij+1/2}, \eta_{j+1/2}) = (x_i, y_{j+1/2})$ and $(\xi^{(v)}_{i+1,j+1/2}, \eta_{j+1/2}) = (x_{i+1}, y_{j+1/2})$, respectively. Since these two u-points and two v-points are all of fluid type, we have [from (55) and (56)]

$$(\Delta s^{(u)*}_{\xi})_{i+1/2,j} = (\Delta s^{(u)*}_{\xi})_{i+1/2,j+1} = \Delta x \tag{128}$$

$$(\Delta s^{(v)*}_{\eta})_{ij+1/2} = (\Delta s^{(v)*}_{\eta})_{i+1,j+1/2} = \Delta y \tag{129}$$

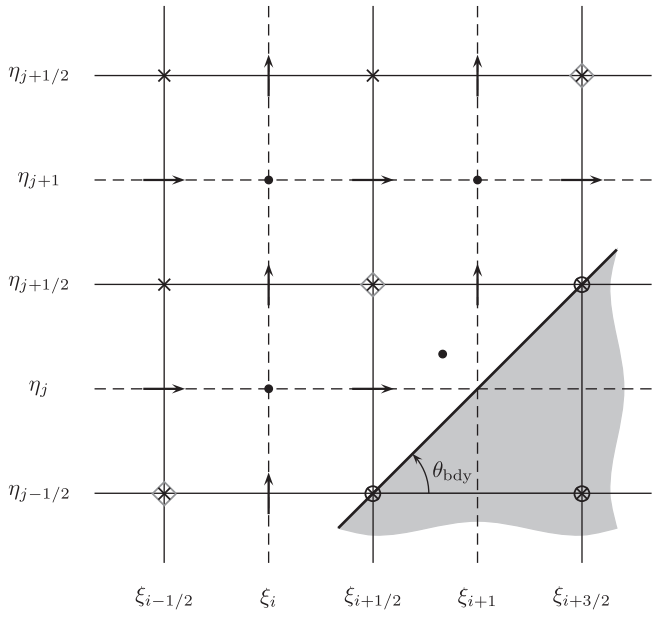

Fig. 11. Linear fluid–land boundary in the $\xi\eta$ plane (which in this case is identical to the Cartesian xy plane) used to demonstrate that if the forcing terms in the momentum equations at near-boundary u- and v-points are evaluated exactly where u and v are defined, the vorticity source term $S^{(\zeta)}_{i+1/2,j+1/2}$ at near-boundary ζ-points does not approach the correct limit as the grid is refined. The thick solid line is the model boundary, and θ_{bdy} is the angle the boundary makes with lines of constant η. The shaded region is land and the clear region is fluid. The dots denote h-points, the arrows denote u- and v-points, and the "×"s denote ζ-points. Circled "×"s denote boundary ζ-points, and "×"s within diamonds denote near-boundary ζ-points [i.e. fluid ζ-points that are surrounded by one or more (but at most four) boundary boxes]. The u-points at $(\xi_{i+1/2},\eta_j)$ and $(\xi_{i+3/2},\eta_{j+1})$ and the v-points at $(\xi_i,\eta_{j-1/2})$ and $(\xi_{i+1},\eta_{j+1/2})$ are near-boundary u- and v-points [i.e. fluid u- and v-points that are surrounded by one or (at most) two boundary boxes].

Substituting these into (35) and expanding the differencing operators, we obtain

$$S^{(\zeta)}_{i+1/2,j+1/2} = \frac{1}{A^{(\zeta)}_{i+1/2,j+1/2}}\left[\Delta y\left\{\left(\frac{S_y}{h}\right)^*_{i+1,j+1/2} - \left(\frac{S_y}{h}\right)^*_{i,j+1/2}\right\} - \Delta x\left\{\left(\frac{S_x}{h}\right)^*_{i+1/2,j+1} - \left(\frac{S_x}{h}\right)^*_{i+1/2,j}\right\}\right] \tag{130}$$

We now use (126) to evaluate the forcing terms in this expression exactly at the locations where u and v are defined. This gives

$$S^{(\zeta)}_{i+1/2,j+1/2} = \frac{1}{A^{(\zeta)}_{i+1/2,j+1/2}}[\Delta y\{(\alpha+\beta x_{i+1}) - (\alpha+\beta x_i)\} - \Delta x\{0-0\}] = \frac{\Delta y}{A^{(\zeta)}_{i+1/2,j+1/2}}\beta(x_{i+1}-x_i) = \beta\frac{\Delta x\Delta y}{A^{(\zeta)}_{i+1/2,j+1/2}} \tag{131}$$

It remains to calculate $A^{(\zeta)}_{i+1/2,j+1/2}$. From (26), we see that this is just the arithmetic average of $A^{(h)}_{i,j+1}$, $A^{(h)}_{i+1,j+1}$, $A^{(h)}_{i,j}$, $A^{(h)}_{i+1,j}$. Since in Fig. 11 the h-points at $(i,j+1)$, $(i+1,j+1)$, and (i,j) are all of fluid type, we have from (30)

$$A^{(h)}_{i,j+1} = A^{(h)}_{i+1,j+1} = A^{(h)}_{i,j} = \Delta x\Delta y \tag{132}$$

Also, since $(i+1,j)$ is a boundary h-point, we see from (30) that in order to obtain $A^{(h)}_{i+1,j}$, we need $A^{(u)}_{i+1/2,j}$, $A^{(u)}_{i+3/2,j}$, $A^{(v)}_{i+1,j-1/2}$, and $A^{(v)}_{i+1,j+1/2}$. These are given by (22) and (23). Since $(i+1/2,j)$ is a fluid u-point, $(i+3/2,j)$ is a land u-point, $(i+1,j-1/2)$ is a land v-point, and $(i+1,j+1/2)$ is a fluid v-point, we have [from (55) and (56)]

$$(\Delta s^{(u)*}_{\xi})_{i+1/2,j} = \Delta x; \quad (\Delta s^{(u)*}_{\xi})_{i+3/2,j} = 0 \tag{133}$$

$$(\Delta s^{(v)*}_{\eta})_{i+1,j-1/2} = 0; \quad (\Delta s^{(v)*}_{\eta})_{i+1,j+1/2} = \Delta y \tag{134}$$

Also, from (16) and (17) and the subsequent discussion, we have

$$(\Delta s^{(u)}_{\eta})_{i+1/2,j} = \Delta y; \quad (\Delta s^{(u)}_{\eta})_{i+3/2,j} = 0 \tag{135}$$

$$(\Delta s^{(v)}_{\xi})_{i+1,j-1/2} = 0; \quad (\Delta s^{(v)}_{\xi})_{i+1,j+1/2} = \Delta x \tag{136}$$

Substituting (133)–(136) into (22) and (23), we obtain

$$A^{(u)}_{i+1/2,j} = \Delta x\Delta y; \quad A^{(u)}_{i+3/2,j} = 0 \tag{137}$$

$$A^{(v)}_{i+1,j-1/2} = 0; \quad A^{(v)}_{i+1,j+1/2} = \Delta x\Delta y \tag{138}$$

Then

$$\overline{(A^{(u)})}^{\xi}_{i+1,j} = \frac{1}{2}\Delta x\Delta y \quad \text{and} \quad \overline{(A^{(v)})}^{\eta}_{i+1,j} = \frac{1}{2}\Delta x\Delta y \tag{139}$$

Substituting these into (30) (with the i index increased by one), we get

$$A^{(h)}_{i+1,j} = \left[\left(\frac{1}{2}\Delta x\Delta y\right)\cos^2\theta_{\text{bdy}} + \left(\frac{1}{2}\Delta x\Delta y\right)\sin^2\theta_{\text{bdy}}\right]_{i+1,j} = \frac{1}{2}\Delta x\Delta y \tag{140}$$

We now substitute (132) and (140) into (26) to obtain

$$A^{(\zeta)}_{i+1/2,j+1/2} = \frac{1}{4}\left[3\Delta x\Delta y + \frac{1}{2}\Delta x\Delta y\right] = \frac{7}{8}\Delta x\Delta y \tag{141}$$

Finally, we substitute (141) into (131) to obtain

$$S^{(\zeta)}_{i+1/2,j+1/2} = \frac{8}{7}\beta \tag{142}$$

Since β is a constant, the RHS of (142) does not change as the grid is refined and the near-boundary ζ-point at $(i + 1/2, j + 1/2)$ approaches the boundary. Thus, in the limit of an infinitely refined grid, $S^{(\zeta)}_{i+1/2,j+1/2}$ does not approach the correct value given by (127). This shows that if the forcing terms at near-boundary u- and v-points are evaluated exactly where u and v are defined, the vorticity source term at near-boundary ζ-points can take on the wrong value regardless of grid resolution, reducing the accuracy of the scheme.

We will now derive the (ξ,η) coordinates of the locations where the forcing terms in the discrete momentum equations at near-boundary u- and v-points must be evaluated in order for $S^{(\zeta)}_{i+1/2,j+1/2}$ at near-boundary ζ-points to converge to the correct limit as the grid is refined. As in Appendix A, we let (ξ_B,η_B) denote the coordinates of some point, say point B, on a fluid–land boundary in the $\xi\eta$ plane (Fig. 4). In the analysis below, we will consider the following limiting process. We will keep the location of B fixed, and we will consider progressively finer grids, focusing on each grid on the near-boundary ζ-point closest to B. This ζ-point will always be at one of the corners of the boundary box that happens to encompass point B. In the limit of an infinitely refined grid, the area of the encompassing boundary box will go to zero, and the near-boundary ζ-point will converge to point B.

On a given grid, let $(\xi_{i+1/2},\eta_{j+1/2})$ denote the coordinates of the near-boundary ζ-point that is closest to point B. From (35), the source term $S^{(\zeta)}_{i+1/2,j+1/2}$ on the RHS of the discrete vorticity equation at this ζ-point is given by

$$S^{(\zeta)}_{i+1/2,j+1/2} = \left[\frac{1}{A^{(\zeta)}}\left[\delta_\xi\left\{\Delta s^{(v)*}_\eta\left(\frac{S_\eta}{h}\right)^*\right\} - \delta_\eta\left\{\Delta s^{(u)*}_\xi\left(\frac{S_\xi}{h}\right)^*\right\}\right]\right]_{i+1/2,j+1/2} \tag{143}$$

Comparing this to (11), we can see that the first term involving S_η on the RHS of (143) is a discrete counterpart of $mn\times\partial(S_\eta/nh)/\partial\xi$ evaluated at $(\xi_{i+1/2},\eta_{j+1/2})$, and the second term is a discrete counterpart of $mn\times\partial(S_\xi/mh)/\partial\eta$ at this same point. Using the fact that $(\Delta s^{(v)*}_\eta)_{i,j+1/2} = \Delta\eta/n^{(v)*}_{i,j+1/2}$ at fluid v-points [see (54)] and expanding the $\delta_\xi(\ldots)$ operator, we can rewrite the first term on the RHS of (143) as follows:

$$\left[\frac{1}{A^{(\zeta)}}\delta_\xi\left\{\Delta s^{(v)*}_\eta\left(\frac{S_\eta}{h}\right)^*\right\}\right]_{i+1/2,j+1/2} = \frac{\Delta\eta}{A^{(\zeta)}_{i+1/2,j+1/2}}\left[\left\{\frac{1}{n^{(v)*}}\left(\frac{S_\eta}{h}\right)^*\right\}_{i+1,j+1/2} - \left\{\frac{1}{n^{(v)*}}\left(\frac{S_\eta}{h}\right)^*\right\}_{i,j+1/2}\right] \tag{144}$$

Similarly, using the fact that $(\Delta s^{(u)*}_\xi)_{i+1/2,j} = \Delta\xi/m^{(u)*}_{i+1/2,j}$ at fluid u-points [see (53)] and expanding the $\delta_\eta(\ldots)$ operator, we can rewrite the second term on the RHS of (143) as follows:

$$\left[\frac{1}{A^{(\zeta)}}\delta_\eta\left\{\Delta s^{(u)*}_\xi\left(\frac{S_\xi}{h}\right)^*\right\}\right]_{i+1/2,j+1/2} = \frac{\Delta\xi}{A^{(\zeta)}_{i+1/2,j+1/2}}\left[\left\{\frac{1}{m^{(u)*}}\left(\frac{S_\xi}{h}\right)^*\right\}_{i+1/2,j+1} - \left\{\frac{1}{m^{(u)*}}\left(\frac{S_\xi}{h}\right)^*\right\}_{i+1/2,j}\right] \tag{145}$$

Since $(\xi_{i+1/2},\eta_{j+1/2})$ approaches point B as we consider progressively finer grids, in the limit of infinite grid refinement the RHS of (144) must converge to the quantity $mn\times\partial(S_\eta/nh)/\partial\xi$ evaluated at B, and the RHS of (145) must converge to the quantity $mn\times\partial(S_\xi/mh)/\partial\eta$ evaluated at B. To obtain the values of these quantities at B, it will be convenient to first expand S_ξ/mh and S_η/nh in terms of the separations in the ξ and η directions between point B and some generic point (ξ,η) within the fluid. We will denote these separations by X and Y, i.e.

$$X = \xi - \xi_B; \quad Y = \eta - \eta_B \tag{146}$$

For small X and Y [i.e. as the generic point (ξ,η) approaches B], we can expand S_ξ/mh and S_η/nh about (ξ_B,η_B) to first order in X and Y as follows:

$$\frac{S_\xi}{mh} = a_0 + a_1X + a_2Y + a_3XY \tag{147}$$

$$\frac{S_\eta}{nh} = b_0 + b_1X + b_2Y + b_3XY \tag{148}$$

Here, a_0, a_1, a_2, b_0, b_1, and b_2 are (generally time-dependent) coefficients that are not functions of ξ and η (or X and Y). Since S_ξ and S_η are arbitrary forcings, we can treat these coefficients as arbitrary quantities. Taking the derivatives of (148) and (147) with respect to ξ and η, respectively, we obtain

$$\frac{\partial}{\partial \xi}\left(\frac{S_\eta}{nh}\right) = \frac{\partial}{\partial X}\left(\frac{S_\eta}{nh}\right) = b_1 + b_3 Y$$
$$\frac{\partial}{\partial \eta}\left(\frac{S_\xi}{mh}\right) = \frac{\partial}{\partial Y}\left(\frac{S_\xi}{mh}\right) = a_2 + a_3 X$$

We now multiply these by mn and evaluate the results at point B to obtain

$$\left[mn\frac{\partial}{\partial \xi}\left(\frac{S_\eta}{nh}\right)\right]_B = m_B n_B \times b_1 \tag{149}$$
$$\left[mn\frac{\partial}{\partial \eta}\left(\frac{S_\xi}{mh}\right)\right]_B = m_B n_B \times a_2 \tag{150}$$

where we have used the fact that X and Y evaluated at point B are zero. In (149) and (150), m_B and n_B are the inverse scale factors evaluated at B. The RHSs of (149) and (150) are the values that the RHSs of (144) and (145) must converge to as we consider progressively finer grids. To determine the conditions under which this requirement is satisfied, we must first express the RHSs of (144) and (145) in terms of a_0 through b_2. For this purpose, we let $(\xi^{(u)*}_{i+1/2,j}, \eta^{(u)*}_{i+1/2,j})$ denote the location where the forcing $[\Delta s^{(u)*}_\xi (S_\xi/h)^*]_{i+1/2,j}$ in the discrete ξ direction momentum equation is evaluated, and we let $(\xi^{(v)*}_{ij+1/2}, \eta^{(v)*}_{ij+1/2})$ denote the location where the forcing $[\Delta s^{(v)*}_\eta (S_\eta/h)^*]_{ij+1/2}$ in the discrete η direction momentum equation is evaluated. [Of course, away from boundaries, $(\xi^{(u)*}_{i+1/2,j}, \eta^{(u)*}_{i+1/2,j})$ is exactly the location of a u-point, i.e. $(\xi^{(u)*}_{i+1/2,j}, \eta^{(u)*}_{i+1/2,j}) = (\xi_{i+1/2}, \eta^{(u)}_{i+1/2,j}) = (\xi_{i+1/2}, \eta_j)$, and $(\xi^{(v)*}_{ij+1/2}, \eta^{(v)*}_{ij+1/2})$ is exactly the location of a v-point, i.e. $(\xi^{(v)*}_{ij+1/2}, \eta^{(v)*}_{ij+1/2}) = (\xi^{(v)}_{ij+1/2}, \eta_{j+1/2}) = (\xi_i, \eta_{j+1/2})$.] Also, we let $X^{(u)*}_{i+1/2,j}$, $Y^{(u)*}_{i+1/2,j}$, $X^{(v)*}_{ij+1/2}$, and $Y^{(v)*}_{ij+1/2}$ denote the X and Y values corresponding to $\xi^{(u)*}_{i+1/2,j}$, $\eta^{(u)*}_{i+1/2,j}$, $\xi^{(v)*}_{ij+1/2}$, and $\eta^{(v)*}_{ij+1/2}$, respectively, i.e.

$$X^{(u)*}_{i+1/2,j} = \xi^{(u)*}_{i+1/2,j} - \xi_B; \quad Y^{(u)*}_{i+1/2,j} = \eta^{(u)*}_{i+1/2,j} - \eta_B \tag{151}$$
$$X^{(v)*}_{ij+1/2} = \xi^{(v)*}_{ij+1/2} - \xi_B; \quad Y^{(v)*}_{ij+1/2} = \eta^{(v)*}_{ij+1/2} - \eta_B \tag{152}$$

Next, we evaluate (148) at $(\xi^{(v)*}_{ij+1/2}, \eta^{(v)*}_{ij+1/2})$ and $(\xi^{(v)*}_{i+1,j+1/2}, \eta^{(v)*}_{i+1,j+1/2})$ and substitute the results into (144) to obtain

$$\left[\frac{1}{A^{(\zeta)}}\delta_\xi\left\{\Delta s^{(v)*}_\eta\left(\frac{S_\eta}{h}\right)^*\right\}\right]_{i+1/2,j+1/2} = \frac{\Delta\eta}{A^{(\zeta)}_{i+1/2,j+1/2}}\left[b_1\left\{X^{(v)*}_{i+1,j+1/2} - X^{(v)*}_{ij+1/2}\right\} + b_2\left\{Y^{(v)*}_{i+1,j+1/2} - Y^{(v)*}_{ij+1/2}\right\} + b_3\left\{X^{(v)*}_{i+1,j+1/2}Y^{(v)*}_{i+1,j+1/2} - X^{(v)*}_{ij+1/2}Y^{(v)*}_{ij+1/2}\right\}\right] \tag{153}$$

Similarly, we evaluate (147) at $(\xi^{(u)*}_{i+1/2,j}, \eta^{(u)*}_{i+1/2,j})$ and $(\xi^{(u)*}_{i+1/2,j+1}, \eta^{(u)*}_{i+1/2,j+1})$ and substitute the results into (145) to obtain

$$\left[\frac{1}{A^{(\zeta)}}\delta_\eta\left\{\Delta s^{(u)*}_\xi\left(\frac{S_\xi}{h}\right)^*\right\}\right]_{i+1/2,j+1/2} = \frac{\Delta\xi}{A^{(\zeta)}_{i+1/2,j+1/2}}\left[a_1\left\{X^{(u)*}_{i+1/2,j+1} - X^{(u)*}_{i+1/2,j}\right\} + a_2\left\{Y^{(u)*}_{i+1/2,j+1} - Y^{(u)*}_{i+1/2,j}\right\} + a_3\left\{X^{(u)*}_{i+1/2,j+1}Y^{(u)*}_{i+1/2,j+1} - X^{(u)*}_{i+1/2,j}Y^{(u)*}_{i+1/2,j}\right\}\right] \tag{154}$$

Note that in evaluating (147) at $(\xi^{(u)*}_{i+1/2,j}, \eta^{(u)*}_{i+1/2,j})$ and $(\xi^{(u)*}_{i+1/2,j+1}, \eta^{(u)*}_{i+1/2,j+1})$ and (148) at $(\xi^{(v)*}_{ij+1/2}, \eta^{(v)*}_{ij+1/2})$ and $(\xi^{(v)*}_{i+1,j+1/2}, \eta^{(v)*}_{i+1,j+1/2})$, we have assumed that these four locations approach point B as we consider progressively finer grids. This requirement arises because (147) and (148) are valid only for small X and Y. Although we will not provide a mathematical proof that this requirement is always satisfied, below we will demonstrate graphically that it is indeed satisfied for the annulus geometry used in the GRSs with the PLS in Section 7.2.

Recall that the requirement for $S^{(\zeta)}_{i+1/2,j+1/2}$ to converge to the correct value is that the RHSs of (153) and (154) converge to those of (149) and (150), respectively. Since b_1, b_2, and b_3 are arbitrary, the RHS of (153) will converge to that of (149) only if the coefficients of b_1, b_2, and b_3 in (153) converge to those in (149), i.e.

$$\frac{\Delta\eta}{A^{(\zeta)}_{i+1/2,j+1/2}}\left[X^{(v)*}_{i+1,j+1/2} - X^{(v)*}_{ij+1/2}\right] \to m_B n_B \quad \text{as we consider progressively finer grids} \tag{155}$$

$$\frac{\Delta\eta}{A^{(\zeta)}_{i+1/2,j+1/2}}\left[Y^{(v)*}_{i+1,j+1/2} - Y^{(v)*}_{ij+1/2}\right] \to 0 \quad \text{as we consider progressively finer grids} \tag{156}$$

$$\frac{\Delta\eta}{A^{(\zeta)}_{i+1/2,j+1/2}}\left[X^{(v)*}_{i+1,j+1/2}Y^{(v)*}_{i+1,j+1/2} - X^{(v)*}_{ij+1/2}Y^{(v)*}_{ij+1/2}\right] \to 0 \quad \text{as we consider progressively finer grids} \tag{157}$$

First, consider (156). The simplest way to satisfy this is to require that

$$\frac{\Delta\eta}{A^{(\zeta)}_{i+1/2,j+1/2}}\left[Y^{(v)*}_{i+1,j+1/2}-Y^{(v)*}_{ij+1/2}\right]=0 \tag{158}$$

Using (152), we can rewrite this as

$$\eta^{(v)*}_{i+1,j+1/2}=\eta^{(v)*}_{ij+1/2} \tag{159}$$

Since at fluid v-points away from boundaries $\eta^{(v)*}_{ij+1/2}=\eta_{j+1/2}$, (159) implies that

$$\eta^{(v)*}_{ij+1/2}=\eta_{j+1/2}\quad\text{at all fluid } v\text{-points} \tag{160}$$

Next, consider (155). To satisfy this, we require that

$$\frac{\Delta\eta}{A^{(\zeta)}_{i+1/2,j+1/2}}\left[X^{(v)*}_{i+1,j+1/2}-X^{(v)*}_{ij+1/2}\right]=1\Big/\overline{\left(\frac{1}{mn}\right)}^{\xi\eta}_{i+1/2,j+1/2} \tag{161}$$

The quantities $(mn)_{ij+1}$, $(mn)_{i+1,j+1}$, $(mn)_{ij}$, and $(mn)_{i+1,j}$ on the RHS of this expression are values of the product mn evaluated at grid box centers (regardless of whether the grid box is fluid, boundary, or land), i.e. at (ξ_i,η_{j+1}), (ξ_{i+1},η_{j+1}), (ξ_i,η_j), and (ξ_{i+1},η_j), respectively. [Recall that m and n are known functions of space (Section 4.1), so we can evaluate them anywhere, i.e. within fluid, within land, or on a boundary.] Satisfying (161) will also satisfy (155) because as the grid is refined, the quantity $1/\overline{(1/mn)}^{\xi\eta}_{i+1/2,j+1/2}$ on the RHS converges to m_Bn_B [because the ζ-point at $(\xi_{i+1/2},\eta_{j+1/2})$ approaches point B, and $1/\overline{(1/mn)}^{\xi\eta}_{i+1/2,j+1/2}$ is a consistent approximation to mn evaluated at $(\xi_{i+1/2},\eta_{j+1/2})$]. Finally, consider (157). We will now show that once (155) and (156) are satisfied [via (160) and (161)], (157) will be automatically satisfied. Substituting (160) into the expression for $Y^{(v)*}_{ij+1/2}$ given in (152), we obtain

$$Y^{(v)*}_{ij+1/2}=Y^{(v)*}_{i+1,j+1/2}=\eta_{j+1/2}-\eta_B\quad\text{at all fluid } v\text{-points} \tag{162}$$

We now substitute (161) and (162) into (157) to obtain the following requirement for the coefficient of b_3 in (153) to converge to that in (149):

$$(\eta_{j+1/2}-\eta_B)\Big/\overline{\left(\frac{1}{mn}\right)}^{\xi\eta}_{i+1/2,j+1/2}\to 0\quad\text{as we consider progressively finer grids} \tag{163}$$

This is automatically satisfied because $\eta_{j+1/2}$ approaches η_B as we consider progressively finer grids. Thus, (157) is satisfied as long as (160) and (161) hold (which they do by assumption).

For convenience, we now use (152) to rewrite (161) as

$$\xi^{(v)*}_{i+1,j+1/2}-\xi^{(v)*}_{ij+1/2}=\Delta\xi\left(\frac{A^{(\zeta)}}{A^{(\zeta),\mathrm{tot}}}\right)_{i+1/2,j+1/2} \tag{164}$$

where we have defined $A^{(\zeta),\mathrm{tot}}_{i+1/2,j+1/2}$ as

$$A^{(\zeta),\mathrm{tot}}_{i+1/2,j+1/2}=\overline{\left(\frac{\Delta\xi\Delta\eta}{mn}\right)}^{\xi\eta}_{i+1/2,j+1/2} \tag{165}$$

$A^{(\zeta),\mathrm{tot}}_{i+1/2,j+1/2}$ is the total (i.e. fluid plus land) area associated with the ζ-point at $(\xi_{i+1/2},\eta_{j+1/2})$. It is defined at all three types of ζ-points (fluid, boundary, and land). Also, using a procedure analogous to the one above, we can show that the RHS of (154) will converge to that of (150) as we consider progressively finer grids if

$$\xi^{(u)*}_{i+1/2,j}=\xi_{i+1/2}\quad\text{at all fluid } u\text{-points} \tag{166}$$

and if

$$\eta^{(u)*}_{i+1/2,j+1}-\eta^{(u)*}_{i+1/2,j}=\Delta\eta\left(\frac{A^{(\zeta)}}{A^{(\zeta),\mathrm{tot}}}\right)_{i+1/2,j+1/2} \tag{167}$$

Eqs. (160) and (166) show that the coordinates of the locations where $[\Delta s^{(u)*}_{\xi}(S_\xi/h)^*]_{i+1/2,j}$ and $[\Delta s^{(v)*}_{\eta}(S_\eta/h)^*]_{ij+1/2}$ in (18) and (19) must be evaluated (in order for $S^{(\zeta)}_{i+1/2,j+1/2}$ at near-boundary ζ-points to converge) are, respectively, $(\xi_{i+1/2},\eta^{(u)*}_{i+1/2,j})$ and $(\xi^{(v)*}_{ij+1/2},\eta_{j+1/2})$, where $\xi^{(v)*}_{ij+1/2}$ and $\eta^{(u)*}_{i+1/2,j}$ can be obtained using the recurrence relations (164) and (167). For most boundary configurations, these relations can be initialized by recalling that away from boundaries (i.e. at non-near-boundary u- and v-points), $\xi^{(v)*}_{ij+1/2}=\xi_i$ and $\eta^{(u)*}_{i+1/2,j}=\eta_j$. For example, consider a configuration in which a fluid–land boundary intersects the grid line $\eta=\eta_{j+1/2}$, and land is to the west of the point of intersection and fluid is to the east. To obtain the shifted ξ coordinates $\xi^{(v)*}_{ij+1/2}$ along this grid line, we first successively consider each fluid v-point to the east of the point of intersection until we find the first one that is not a near-boundary v-point (i.e. the first one that is far enough from the boundary to be surrounded by

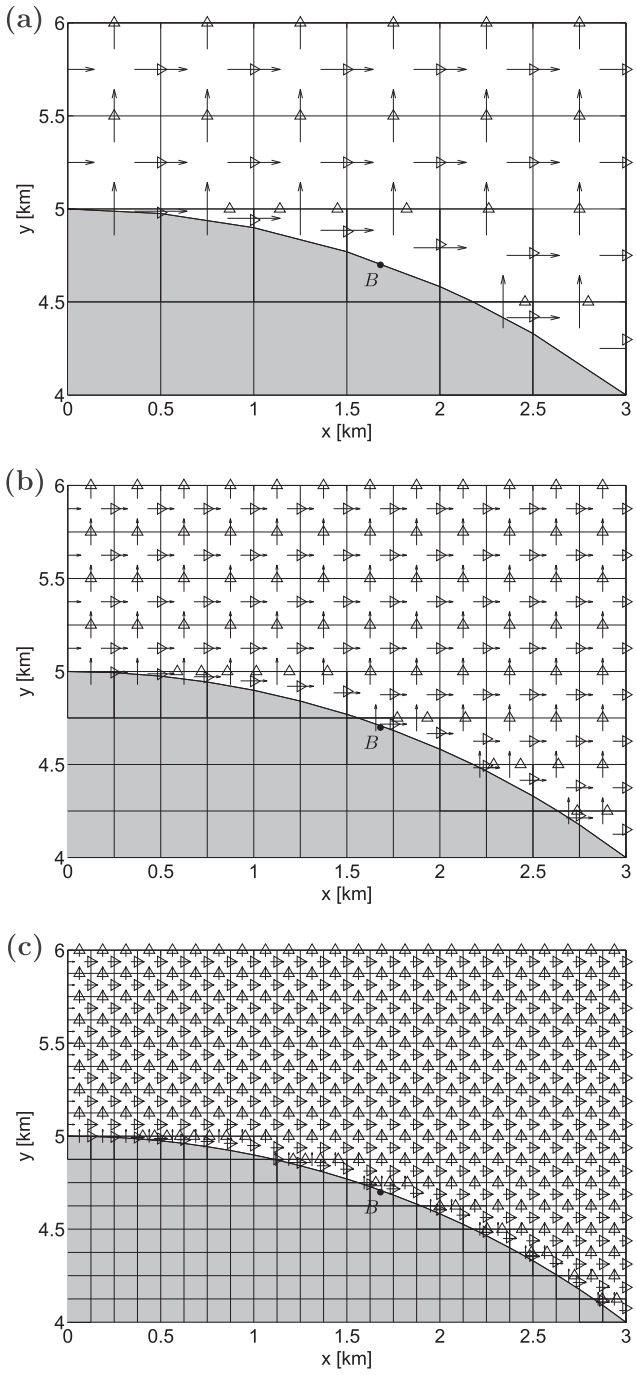

Fig. 12. u-points, v;-points, and the corresponding shifted locations $(\xi_{i+1/2}, \eta^{(u)*}_{i+1/2,j})$ and $(\xi^{(v)*}_{i,j+1/2}, \eta_{j+1/2})$ where the momentum forcings $[\Delta s^{(u)*}_{\xi}(S_{\xi}/h)^{*}]_{i+1/2,j}$ and $[\Delta s^{(v)*}_{\eta}(S_{\eta}/h)^{*}]_{i,j+1/2}$, respectively, are evaluated near a portion of the inner boundary of the northeastern quarter of the annulus used in TCs 7–10 in Section 7.2. The shaded regions are land and the clear regions are fluid. The horizontal arrows denote u-points, the vertical arrows denote v-points, the right pointing triangles denote the locations $(\xi_{i+1/2}, \eta^{(u)*}_{i+1/2,j})$, and the upward pointing triangles denote the locations $(\xi^{(v)*}_{i,j+1/2}, \eta_{j+1/2})$. These points and locations are shown on the $\Delta x = \Delta y = 500$ m Cartesian grid in (a), on the 250 m grid in (b), and on the 125 m grid in (c). Point B represents an arbitrary location on the boundary.

two fluid h-points). For such a v-point, $\xi^{(v)*}_{i,j+1/2} = \xi^{(v)}_{i,j+1/2} = \xi_i$. Substituting this value into (164) (with the i index reduced by one) and rearranging terms, we obtain $\xi^{(v)*}_{i-1,j+1/2}$. Next, we use (164) again (with the i index now reduced by two) to find $\xi^{(v)*}_{i-2,j+1/2}$. We repeat this procedure until we have found $\xi^{(v)*}_{i,j+1/2}$ corresponding to each near-boundary v-point along the grid line between the point of intersection with the boundary and the first non-near-boundary v-point to the east. If the locations of land and fluid are reversed (i.e. if there is fluid to the west of the point of intersection and land to the east), we start at the

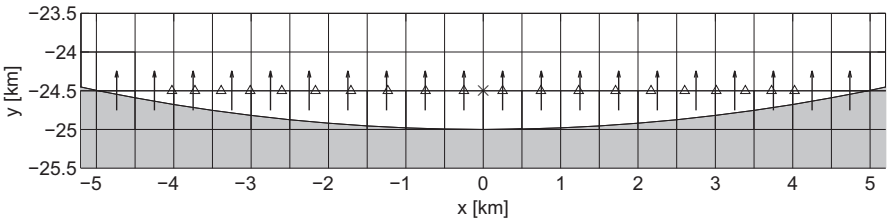

Fig. 13. v-points (denoted by vertical arrows) and the corresponding shifted locations $(\xi^{(v)*}_{i,j+1/2}, \eta_{j+1/2})$ (denoted by upward pointing triangles) along the last east–west grid line that intersects the southern portion of the outer boundary of the annulus on the $\Delta x = \Delta y = 500$ m grid used in TCs 7–10 in Section 7.2. The shaded region is land and the clear region is fluid. The grid line of interest is along $y = y_{1+1/2} = 24.5$ km. The near-boundary ζ-point along this grid line that has the largest area $A^{(\zeta)}_{i+1/2,j+1/2}$ is denoted by an "$\times$". For clarity, v-points and their corresponding shifted locations are shown only along the east–west grid line of interest while u-points and their corresponding shifted locations along north–south grid lines are not shown.

first non-near-boundary v-point to the west of the point of intersection (where we know that $\xi^{(v)*}_{i,j+1/2} = \xi^{(v)}_{i,j+1/2} = \xi_i$) and use (164) to successively calculate $\xi^{(v)*}_{i,j+1/2}$ at near-boundary v-points further east. We use an analogous procedure to obtain $\eta^{(u)*}_{i+1/2,j}$ at each near-boundary u-point. As an example, we show in Fig. 12 the locations of u- and v-points and the shifted locations where the momentum forcings are evaluated near a portion of the inner boundary of the northeastern quarter of the annulus on the $\Delta x = \Delta y = 500$ m, 250 m, and 125 m grids used in test cases (TCs) 7–10 in Section 7.2. Point B in these figures represents an arbitrary location on the boundary. Note that, as required in the derivation above, the shifted locations corresponding to the faces of the boundary box that encompasses point B approach B as the grid is refined.

The procedure described above for finding $\xi^{(v)*}_{i,j+1/2}$ and $\eta^{(u)*}_{i+1/2,j}$ does not work for near-boundary u- and v-points that are located along the last grid line that intersects a concave boundary (e.g. a bay). This is because in such cases, we do not encounter any non-near-boundary u- or v-points as we move away from the boundary and into fluid along the grid line; we encounter only near-boundary u- or v-points before finally reaching another boundary. For example, such a situation occurs along the first east–west grid line (i.e. grid line along which η is constant) north of the southern edge of the domain containing the annulus in TCs 7–10 in Section 7.2. This grid line defined by $y = -25$ km $+ \Delta y$ (with the southern edge of the domain lying along $y = -25$ km). Fig. 13 shows this grid line on the $\Delta x = \Delta y = 500$ m grid (so that in the figure, the grid line of interest is along $y = -24.5$ km). Note that all the fluid v-points along this grid line are near-boundary v-points because the row of grid boxes to the south of them are all boundary boxes. In such cases, we must somehow choose one near-boundary u- or v-point at which to set $\xi^{(v)*}_{i,j+1/2}$ or $\eta^{(u)*}_{i+1/2,j}$. We can then use the recursion relation (164) or (167) to find $\xi^{(v)*}_{i,j+1/2}$ or $\eta^{(u)*}_{i+1/2,j}$ at the remaining near-boundary u- or v-points along the grid line. In the PLS, the procedure we follow is to set $\xi^{(v)*}_{i,j+1/2}$ or $\eta^{(u)*}_{i+1/2,j}$ symmetrically around the near-boundary ζ-point that has the largest area $A^{(\zeta)}_{i+1/2,j+1/2}$ [given by (26)] out of all the near-boundary ζ-points along the grid line. As an example, assume that this near-boundary ζ-point has coordinates $(\xi_{i+1/2}, \eta_{j+1/2})$ and that as in Fig. 13, we are considering an east–west grid line (as opposed to a north–south one). In that figure, the near-boundary ζ-point having the largest $A^{(\zeta)}_{i+1/2,j+1/2}$ is denoted by an "$\times$". Then setting $\xi^{(v)*}_{i,j+1/2}$ and $\xi^{(v)*}_{i+1,j+1/2}$ symmetrically about $(\xi_{i+1/2}, \eta_{j+1/2})$ requires that the difference between $\xi_{i+1/2}$ and $\xi^{(v)*}_{i,j+1/2}$ be equal to the difference between $\xi^{(v)*}_{i+1,j+1/2}$ and $\xi_{i+1/2}$, i.e.

$$\xi_{i+1/2} - \xi^{(v)*}_{i,j+1/2} = \xi^{(v)*}_{i+1,j+1/2} - \xi_{i+1/2} \tag{168}$$

Rearranging this, we get

$$\xi^{(v)*}_{i+1,j+1/2} = 2\xi_{i+1/2} - \xi^{(v)*}_{i,j+1/2} \tag{169}$$

Substituting this into (164) and solving for $\xi^{(v)*}_{i,j+1/2}$, we obtain

$$\xi^{(v)*}_{i,j+1/2} = \xi_{i+1/2} - \frac{1}{2}\Delta\xi\left(\frac{A^{(\zeta)}}{A^{(\zeta),\mathrm{tot}}}\right)_{i+1/2,j+1/2} \tag{170}$$

With $\xi^{(v)*}_{i,j+1/2}$ now set, we can use (164) to calculate $\xi^{(v)*}_{i-1,j+1/2}$, $\xi^{(v)*}_{i-2,j+1/2}$, etc. for all the near-boundary v-points west of the one at $(i, j + 1/2)$ and to calculate $\xi^{(v)*}_{i+1,j+1/2}$, $\xi^{(v)*}_{i+2,j+1/2}$, etc. for all the near-boundary v-points east of it. In Fig. 13, the shifted locations obtained using this procedure are denoted by upward pointing triangles. The shifted η coordinates $\eta^{(u)*}_{i+1/2,j}$ along the last north–south grid line that intersects a concave boundary are obtained using an analogous procedure.

Finally, note that if a boundary profile appears jagged on a given grid (e.g. it alternates between being concave and convex from one grid box to the next), it is likely not worthwhile to find $\xi^{(v)*}_{i,j+1/2}$ and $\eta^{(u)*}_{i+1/2,j}$ for that boundary because evaluating the forcing terms at $\xi^{(v)*}_{i,j+1/2}$ and $\eta^{(u)*}_{i+1/2,j}$ is helpful only if the boundary is resolved enough to have a smooth profile. Thus, in such poorly resolved cases, it is sufficient to simply evaluate the momentum forcings at near-boundary u- and v-points exactly where u and v are defined (as is done in the UNPLS).

Appendix C. Error norms

Given an approximate scalar field $\phi(\xi,\eta)$ and its exact counterpart $\phi^{(e)}(\xi,\eta)$, we define the error $\Delta\phi$ in ϕ as follows:

$$\Delta\phi = \phi - \phi^{(e)} \tag{171}$$

The L_1, L_2, and L_∞ norms of $\Delta\phi$ are given by

$$\|\Delta\phi\|_1 = \frac{1}{A_f}\int_{\Omega_f} |\Delta\phi| ds_\xi\, ds_\eta = \frac{1}{A_f}\int_{\Omega_f} |\Delta\phi| dA \tag{172}$$

$$\|\Delta\phi\|_2 = \left[\frac{1}{A_f}\int_{\Omega_f} |\Delta\phi|^2 ds_\xi\, ds_\eta\right]^{1/2} = \left[\frac{1}{A_f}\int_{\Omega_f} |\Delta\phi|^2 dA\right]^{1/2} \tag{173}$$

$$\|\Delta\phi\|_\infty = \max_{(\xi,\eta)\in\Omega_f} |\Delta\phi| \tag{174}$$

Recall from Section 2 that Ω_f is the flow domain in the $\xi\eta$ plane (not including land bodies), and $ds_\xi = d\xi/m$ and $ds_\eta = d\eta/n$ are incremental physical distances along curves of constant η and ξ, respectively. In (172) and (173), A_f denotes the physical area of Ω_f, and $dA = ds_\xi ds_\eta$ is an infinitesimal portion of A_f. Thus, A_f is given by

$$A_f = \int_{\Omega_f} dA = \int_{\Omega_f} ds_\xi\, ds_\eta = \int_{\Omega_f} \frac{d\xi}{m}\frac{d\eta}{n} \tag{175}$$

We discretize (172)–(174) over fluid and boundary grid boxes as follows:

$$\|\Delta\phi\|_1 = \frac{1}{A_f}\times \sum_{\substack{\text{fld. \& bdy.}\\ h\text{-points}}} |(\Delta\phi)_{i,j}| A_{i,j}^{(h),\text{geom}} \tag{176}$$

$$\|\Delta\phi\|_2 = \left[\frac{1}{A_f}\times \sum_{\substack{\text{fld. \& bdy.}\\ h\text{-points}}} |(\Delta\phi)_{i,j}|^2 A_{i,j}^{(h),\text{geom}}\right]^{1/2} \tag{177}$$

$$\|\Delta\phi\|_\infty = \max_{\substack{\text{fld. \& bdy.}\\ h\text{-points}}} |(\Delta\phi)_{i,j}| \tag{178}$$

The total fluid area A_f appearing in (176) and (177) is obtained using the following discrete counterpart of (175):

$$A_f = \sum_{\substack{\text{fld. \& bdy.}\\ h\text{-points}}} A_{i,j}^{(h),\text{geom}} \tag{179}$$

In these expressions, $A_{i,j}^{(h),\text{geom}}$ is the geometric area of the fluid or boundary box at (i,j) [as opposed to the area $A_{i,j}^{(h)}$ associated with the box in the PLS given by (30)]. [Note that we could use $A_{i,j}^{(h)}$ instead of $A_{i,j}^{(h),\text{geom}}$ in (176), (177) and (179). We have tried both and have found that this choice does not have any discernible effect on the accuracy results obtained in Section 7.] $(\Delta\phi)_{i,j}$ in (176)–(178) is the error in ϕ evaluated at the fluid or boundary h-point at (i,j). The way $(\Delta\phi)_{i,j}$ is calculated depends on the quantity that ϕ represents. Here, we are interested in the case of ϕ representing h, u, v, ζ, or q. We calculate the errors in these quantities as follows:

$$(\Delta h)_{i,j} = h_{i,j} - (h^{(e)})_{i,j} \tag{180}$$

$$(\Delta u)_{i,j} = \hat{u}_{i,j} - (u^{(e)})_{i,j} \tag{181}$$

$$(\Delta v)_{i,j} = \hat{v}_{i,j} - (v^{(e)})_{i,j} \tag{182}$$

$$(\Delta\zeta)_{i,j} = \hat{\zeta}_{i,j} - (\zeta^{(e)})_{i,j} \tag{183}$$

$$(\Delta q)_{i,j} = \hat{q}_{i,j} - (q^{(e)})_{i,j} \tag{184}$$

In these, $\hat{u}_{i,j}$, $\hat{v}_{i,j}$, $\hat{\zeta}_{i,j}$, and $\hat{q}_{i,j}$ denote the values of u, v, ζ, and q at the fluid or boundary h-point at (i,j) obtained from neighboring u-, v-, and ζ-points, and $(h^{(e)})_{i,j}$, $(u^{(e)})_{i,j}$, $(v^{(e)})_{i,j}$, $(\zeta^{(e)})_{i,j}$, and $(q^{(e)})_{i,j}$ denote the exact values of h, u, v, ζ, and q at (i,j). In the STS, we obtain $\hat{u}_{i,j}$ at all fluid h-points by arithmetic averaging, i.e. $\hat{u}_{i,j} = \overline{u}^{\xi}_{i,j}$. In the PLS and UNPLS, we also set $\hat{u}_{i,j} = \overline{u}^{\xi}_{i,j}$ at fluid h-points, but at boundary h-points we obtain $\hat{u}_{i,j}$ by performing bilinear interpolation using u values from the four u-points closest to the h-point in consideration. We follow an analogous procedure to obtain $\hat{v}_{i,j}$. Finally, in all three boundary schemes, we calculate $\hat{\zeta}_{i,j}$ and $\hat{q}_{i,j}$ at all non-land h-points using area-weighted averaging, i.e.

$$\hat{\zeta}_{i,j} = \frac{\overline{(A^{(\zeta)}\zeta)_{i,j}}^{\xi\eta}}{\overline{(A^{(\zeta)})_{i,j}}^{\xi\eta}} \quad \text{and} \quad \hat{q}_{i,j} = \frac{\overline{(A^{(\zeta)}q)_{i,j}}^{\xi\eta}}{\overline{(A^{(\zeta)})_{i,j}}^{\xi\eta}} \tag{185}$$

Away from boundaries and in unstretched Cartesian coordinates (which is what we use in all the GRSs in Section 7), $\hat{\zeta}_{i,j}$ and $\hat{q}_{i,j}$ are equivalent to $\overline{\zeta}^{\xi\eta}_{i,j}$ and $\overline{q}^{\xi\eta}_{i,j}$. Note that (185) weighs $\zeta_{i+1/2,j+1/2}$ and $q_{i+1/2,j+1/2}$ values at boundary ζ-points less than those at fluid ζ-points because $A^{(\zeta)}_{i+1/2,j+1/2}$ at boundary ζ-points is smaller than at fluid ζ-points. In particular, in the PLS and UNPLS, if a boundary ζ-point has a very small area (i.e. if it is almost but not quite a land ζ-point), $\zeta_{i+1/2,j+1/2}$ and $q_{i+1/2,j+1/2}$ at that boundary ζ-point will not contribute much to the values of $\hat{\zeta}_{i,j}$ and $\hat{q}_{i,j}$ at neighboring boundary h-points. Note that we also use $\hat{u}_{i,j}$, $\hat{v}_{i,j}$, $\hat{\zeta}_{i,j}$, and $\hat{q}_{i,j}$ to generate the velocity, vorticity, and potential vorticity fields in the various figures in this paper.

We obtain the exact values $(h^{(e)})_{i,j}$ through $(q^{(e)})_{i,j}$ in (180)–(184) as follows. In the channel flow test cases (TCs) (TCs 1–6 in Section 7, all of which have analytic solutions), we simply evaluate the analytic solutions at the Cartesian coordinates of the fluid or boundary h-point at (i,j), i.e. $(x^{(h)}_{i,j}, y^{(h)}_{i,j})$, to obtain $(h^{(e)})_{i,j}$ through $(q^{(e)})_{i,j}$. In the annulus flow TCs (TCs 7–10 in Section 7, none of which have analytic solutions), we first use $(x^{(h)}_{i,j}, y^{(h)}_{i,j})$ to calculate the corresponding cylindrical coordinates of the fluid or boundary h-point. We then use bilinear interpolation in the $r\theta$ plane on the results of the "exact" simulation in cylindrical coordinates to obtain $(h^{(e)})_{i,j}$, $(u^{(e)}_r)_{i,j}$, $(u^{(e)}_\theta)_{i,j}$, $(\zeta^{(e)})_{i,j}$, and $(q^{(e)})_{i,j}$ at these cylindrical coordinates. Here, $(u^{(e)}_r)_{i,j}$ and $(u^{(e)}_\theta)_{i,j}$ are the exact values of the cylindrical components of the velocity. To obtain the Cartesian components $(u^{(e)})_{i,j}$ and $(v^{(e)})_{i,j}$ from $(u^{(e)}_r)_{i,j}$ and $(u^{(e)}_\theta)_{i,j}$, we use expressions (82) and (83).

In TCs 7–10, extrapolation is necessary near the boundaries of the annulus because some boundary h-points on the Cartesian grids lie between the boundary and the first h-point or u_θ-point within the flow on the cylindrical grid. At such locations, $(h^{(e)})_{i,j}$ and $(u^{(e)}_\theta)_{i,j}$ cannot be obtained by interpolation because they are defined at locations that are offset by half a grid box from the boundary (in the radial direction). To be able to use bilinear interpolation again in this situation, we first use quadratic extrapolation in the radial direction on the results of the "exact" simulation in cylindrical coordinates to obtain values of h and u_θ within land half a grid box beyond the boundaries of the annulus. For example, if the inner boundary is at $\xi_{1/2} = r_{1/2} = 5$ km, we use $h_{1,j}$, $h_{2,j}$, and $h_{3,j}$ (which are defined at $r_1 = 5$ km $+ \Delta r/2$, $r_2 = r_1 + \Delta r$, and $r_3 = r_2 + \Delta r$, respectively, where Δr is the radial grid size of the cylindrical grid) to extrapolate out to $r_0 = 5$ km $- \Delta r/2$ (which is a location within land) and obtain a value for $h_{0,j}$. We perform such extrapolations for all j on the cylindrical grid and at both the inner and outer boundaries of the annulus. We perform similar extrapolations with u_θ. We then use these extrapolated values along with the first set of h and u_θ values inside the flow to perform bilinear interpolation and obtain $(h^{(e)})_{i,j}$ and $(u^{(e)}_\theta)_{i,j}$ at those boundary h-points on the Cartesian grids that lie between the boundary and the first h-point or u_θ-point within the flow on the cylindrical grid.

Appendix D. Time step and stability

In this appendix, we discuss the stability of the STS, PLS, and UNPLS with respect to the time step Δt and the procedure we use to determine Δt for a given simulation.

Using a combined analytic and numerical approach, we have found [see Section 3.15 and Appendix H of [27]] that with an explicit time integration method, the maximum time step for stability of the original AL81 scheme (i.e. in the absence of land bodies) imposed by the Courant–Friedrichs–Lewy (CFL) stability condition is given by [from Eq. (3.335) of [27]]

$$\Delta t_{\max} = \mathrm{CFL}_{\max} \Big/ \max_{i,j} \left[a + b\left(\frac{b}{a+b}\right)^{0.4} \right]_{i,j} \tag{186}$$

where

$$a_{i,j} = \left[4c_g^2 \left(\frac{1}{\Delta s_\xi^2} + \frac{1}{\Delta s_\eta^2} \right) + f^2 \right]^{1/2}_{i,j}, \quad b_{i,j} = \left[\frac{|\overline{u}^{\xi}|}{\Delta s_\xi} + \frac{|\overline{v}^{\eta}|}{\Delta s_\eta} \right]_{i,j}, \tag{187}$$

$(c_g)_{i,j} = (g h_{i,j})^{1/2}$, $(\Delta s_\xi)_{i,j} = \Delta\xi / m_{i,j}$, $(\Delta s_\eta)_{i,j} = \Delta\eta / n_{i,j}$, $m_{i,j}$ and $n_{i,j}$ are the inverse scale factors m and n evaluated at grid box centers (ξ_i, η_j), and $\mathrm{CFL}_{\max}$ is a constant that depends on the choice of time integration method. For fourth-order Runge–Kutta (RK4) time integration, $\mathrm{CFL}_{\max} = 2\sqrt{2}$. Expression (186) predicts a value for $\Delta t_{\max}$ that is within a few percent of the actual value obtained by numerical testing. When land bodies are present, we find that (186) is still valid as long as the STS is used to approximate the boundaries. However, with the PLS, the presence of small boundary boxes imposes a more stringent CFL restriction on Δt. We attempted to obtain an expression analogous to (186) for the PLS (which would also apply to the UNPLS) but were not successful. In the absence of such an expression, we used trial-and-error to find $\Delta t_{\max}$ for the simulations with the PLS and UNPLS. We then multiplied $\Delta t_{\max}$ by a safety factor between 0.15 and 0.90 to obtain Δt, and we used this Δt not only for the PLS and UNPLS on a given Cartesian grid but also for the STS on that grid even though a larger Δt [as specified by (186)] could have been used for the STS. We did this so that a simulation with the STS on a given grid has the same temporal truncation error as the simulations with the PLS and UNPLS on that grid (although in practice, we have found that, at least with RK4, the truncation errors arising from the temporal discretization are much smaller than those from the spatial discretization, so the choice of Δt does not matter much as long as the integration is stable). Finally, note that (186) is valid for the simulations in cylindrical coordinates used to obtain the "exact" solutions in test cases (TCs) 7–10 because there are no boundary boxes in these simulations; there are only fluid and land boxes. Thus, for the cylindrical simulations, we first estimated $\Delta t_{\max}$ using (186) and then multiplied it by a safety factor of 0.40 for TCs 7–9 and 0.75 for TC 10 to obtain Δt.

Since with an explicit time integration method the CFL limit on Δt can be quite restrictive (specially for the PLS and UNPLS), we intend to implement an unconditionally stable implicit time integration method in our SWE model. Since the

model equations are nonlinear, this requires the use of an iterative sparse matrix solver. This in itself is an involved task, and it is further complicated by the fact that the boundaries can have arbitrary shapes and that the solution procedure is different at boundaries than within the fluid (i.e. a vorticity equation must be solved at boundary ζ-points, not a continuity and/or momentum equation). For this reason, we have left this task for a future publication.

Appendix E. Analytic solutions for one dimensional channel flows

Consider a channel of width w_{chan} aligned with the X axis of a Cartesian coordinate system $(\xi,\eta) = (X,Y)$ with $Y = 0$ denoting the centerline of the channel (so that the bottom wall is at $Y = -w_{\text{chan}}/2$ and the top wall is at $Y = w_{\text{chan}}/2$). This geometry is shown in Fig. 6. We will let U and V denote the velocity components in the X and Y directions, respectively. In order to be able to obtain analytic solutions for this geometry, we consider only one dimensional flows parallel to the channel walls, i.e. flows in which

$$\frac{\partial}{\partial X}(\ldots) = 0 \tag{188}$$

$$V = 0 \tag{189}$$

$$S_Y = 0 \tag{190}$$

Here, S_Y is the forcing in the Y direction. Also, for now, we assume that $f = 0$. The $f \neq 0$ case is considered later below. Then the SWEs (1)–(3) reduce to

$$\frac{\partial h}{\partial t} = 0 \tag{191}$$

$$\frac{\partial U}{\partial t} = \frac{S_X}{h} \tag{192}$$

$$\frac{\partial h}{\partial Y} = 0 \tag{193}$$

where S_X is the forcing in the X direction. In obtaining (191)–(193), we have also used the fact that $m = n = 1$ for a Cartesian coordinate system. From (191) and (193), we see that h has a constant, uniform value, i.e.

$$h = h_{\text{o}} \tag{194}$$

We now assume that S_X/h is given by

$$\frac{S_X}{h}(Y,t) = \left[(S_X/h)_{\text{ctr}} + \left\{(S_X/h)_{\text{top}} - (S_X/h)_{\text{bot}}\right\}\frac{Y}{w_{\text{chan}}} + 2\left\{(S_X/h)_{\text{top}} - 2(S_X/h)_{\text{ctr}} + (S_X/h)_{\text{bot}}\right\}\left(\frac{Y}{w_{\text{chan}}}\right)^2\right] \times T(t) \tag{195}$$

Note that this is a quadratic function of Y. Here, $(S_X/h)_{\text{bot}}$, $(S_X/h)_{\text{ctr}}$, and $(S_X/h)_{\text{top}}$ are the values of S_X/h at the bottom wall, channel centerline, and top wall, and $T(t)$ is the time-dependent part of the forcing. We choose the latter as

$$T(t) = \frac{1}{2}\left[\text{erf}\left(\frac{t-t_1}{t_0}\right) - \text{erf}\left(\frac{t-t_2}{t_0}\right)\right] \tag{196}$$

where erf(...) is the error function, $t_0 = 1000$ s, $t_1 = 5000$ s, and $t_2 = 10{,}000$ s. This choice for $T(t)$ corresponds to the presence of forcing between about 5000 s and 10,000 s. Substituting (195) and (196) into (192) and integrating the result from $t = 0$ to some generic time t, we obtain

$$U(Y,t) = U_{\text{o}}(Y) + \left[(S_X/h)_{\text{ctr}} + \left\{(S_X/h)_{\text{top}} - (S_X/h)_{\text{bot}}\right\}\frac{Y}{w_{\text{chan}}} + 2\left\{(S_X/h)_{\text{top}} - 2(S_X/h)_{\text{ctr}} + (S_X/h)_{\text{bot}}\right\}\left(\frac{Y}{w_{\text{chan}}}\right)^2\right] \times I(t) \tag{197}$$

where $U_{\text{o}}(Y)$ is the initial velocity profile and $I(t)$ is the time integral of $T(t)$. The latter is given by

$$I(t) = \frac{1}{2}t_0 \times \left[\frac{t-t_1}{t_0}\text{erf}\left(\frac{t-t_1}{t_0}\right) + \frac{1}{\sqrt{\pi}}\exp\left\{-\left(\frac{t-t_1}{t_0}\right)^2\right\} - \frac{t_1}{t_0}\text{erf}\left(\frac{t_1}{t_0}\right) - \frac{1}{\sqrt{\pi}}\exp\left\{-\left(\frac{t_1}{t_0}\right)^2\right\} - \frac{t-t_2}{t_0}\text{erf}\left(\frac{t-t_2}{t_0}\right) - \frac{1}{\sqrt{\pi}}\exp\left\{-\left(\frac{t-t_2}{t_0}\right)^2\right\} + \frac{t_2}{t_0}\text{erf}\left(\frac{t_2}{t_0}\right) + \frac{1}{\sqrt{\pi}}\exp\left\{-\left(\frac{t_2}{t_0}\right)^2\right\}\right] \tag{198}$$

We now choose $U_{\text{o}}(Y)$ to be a quadratic function of Y, i.e.

$$U_{\text{o}}(Y) = U_{\text{ctr}} + (U_{\text{top}} - U_{\text{bot}})\frac{Y}{w_{\text{chan}}} + 2(U_{\text{top}} - 2U_{\text{ctr}} + U_{\text{bot}})\left(\frac{Y}{w_{\text{chan}}}\right)^2 \tag{199}$$

where U_{bot}, U_{ctr}, and U_{top} are the values of U_o at the bottom wall, channel centerline, and top wall. Substituting this into (197) gives

$$U(Y,t) = \left[U_{ctr} + (U_{top} - U_{bot})\frac{Y}{w_{chan}} + 2(U_{top} - 2U_{ctr} + U_{bot})\left(\frac{Y}{w_{chan}}\right)^2\right] + \left[(S_X/h)_{ctr} + \left\{(S_X/h)_{top} - (S_X/h)_{bot}\right\}\frac{Y}{w_{chan}} + 2\left\{(S_X/h)_{top} - 2(S_X/h)_{ctr} + (S_X/h)_{bot}\right\}\left(\frac{Y}{w_{chan}}\right)^2\right] \times I(t) \quad (200)$$

Once w_{chan}, h_o, U_{bot}, U_{ctr}, U_{top}, $(S_X/h)_{bot}$, $(S_X/h)_{ctr}$, and $(S_X/h)_{top}$ are specified, Eqs. (189), (194), (198) and (200) completely determine the solution for the case without rotation.

Next, we consider the case with rotation, i.e. $f \neq 0$. We will assume here that f is a (nonzero) constant. In this case, we can obtain an analytic solution only if there is no forcing. Thus, we now assume that $S_X = 0$ [in addition to assuming that $\partial(\ldots)/\partial X = 0$, $V = 0$, and $S_Y = 0$]. Then Eqs. (1)–(3) reduce to

$$\frac{\partial h}{\partial t} = 0 \quad (201)$$

$$\frac{\partial U}{\partial t} = 0 \quad (202)$$

$$\frac{\partial h}{\partial Y} = -\frac{f}{g}U \quad (203)$$

From (201), (202) and (189) and the assumption that $\partial(\ldots)/\partial X = 0$, we see that h and U are not functions of t; they are only functions of Y. We now assume that the initial velocity profile $U_o(Y)$ is again given by (199). Then U must be given for all time by

$$U(Y) = U_{ctr} + (U_{top} - U_{bot})\frac{Y}{w_{chan}} + 2(U_{top} - 2U_{ctr} + U_{bot})\left(\frac{Y}{w_{chan}}\right)^2 \quad (204)$$

Substituting this into (203) and integrating the result from the bottom wall of the channel up to some generic Y, we obtain the following time-independent solution for $h(Y)$:

$$h(Y) = h_{bot} - \frac{f}{g}w_{chan} \times \left[\frac{U_{ctr}}{2}\left\{2\left(\frac{Y}{w_{chan}}\right) + 1\right\} + \frac{U_{top} - U_{bot}}{8}\left\{4\left(\frac{Y}{w_{chan}}\right)^2 - 1\right\} + \frac{U_{top} - 2U_{ctr} + U_{bot}}{12}\left\{8\left(\frac{Y}{w_{chan}}\right)^3 + 1\right\}\right] \quad (205)$$

Here, h_{bot} is the value of h at the bottom wall. Once w_{chan}, f, h_{bot}, U_{bot}, U_{ctr}, and U_{top} are specified, (189), (204) and (205) completely determine the (time-independent) solution for the case with rotation.

References

[1] G.S. Ketefian, M.Z. Jacobson, A mass, energy, vorticity, and potential enstrophy conserving lateral fluid–land boundary scheme for the shallow water equations, J. Comput. Phys. 228 (2009) 1–32.
[2] A. Arakawa, V.R. Lamb, A potential enstrophy and energy conserving scheme for the shallow water equations, Mon. Weather Rev. 109 (1981) 18–36.
[3] A. Adcroft, C. Hill, J. Marshall, Representation of topography by shaved cells in a height coordinate ocean model, Mon. Weather Rev. 125 (1997) 2293–2315.
[4] R.C. Pacanowski, A. Gnanadesikan, Transient response in a Z-level ocean model that resolves topography with partial cells, Mon. Weather Rev. 126 (1998) 3248–3270.
[5] Y. Lu, D.G. Wright, D. Brickman, Internal tide generation over topography: experiments with a free-surface z-level ocean model, J. Atmos. Ocean. Technol. 18 (2001) 1076–1091.
[6] D.M. Causon, D.M. Ingram, C.G. Mingham, G. Yang, R.V. Pearson, Calculation of shallow water flows using a Cartesian cut cell approach, Adv. Water Resour. 23 (2000) 545–562.
[7] J. Steppeler, H.-W. Bitzer, M. Minotte, L. Bonaventura, Nonhydrostatic atmospheric modeling using a z-coordinate representation, Mon. Weather Rev. 130 (2002) 2143–2149.
[8] R.L. Walko, R. Avissar, The ocean–land–atmosphere model (OLAM). Part II: Formulation and tests of the nonhydrostatic dynamic core, Mon. Weather Rev. 136 (2008) 4045–4062.
[9] M.P. Kirkpatrick, S.W. Armfield, J.H. Kent, A representation of curved boundaries for the solution of the Navier–Stokes equations on a staggered three-dimensional Cartesian grid, J. Comput. Phys. 184 (2003) 1–36.
[10] A. Biastoch, R.H. Käse, D.B. Stammer, The sensitivity of the Greenland–Scotland Ridge overflow to forcing changes, J. Phys. Oceanogr. 33 (2003) 2307–2319.
[11] E.D. Skyllingstad, H.W. Wijesekera, Large-eddy simulation of flow over two-dimensional obstacles: high drag states and mixing, J. Phys. Oceanogr. 34 (2004) 94–112.
[12] M.A. Spall, R.S. Pickart, Wind-driven recirculations and exchange in the Labrador and Irminger Seas, J. Phys. Oceanogr. 33 (2003) 1829–1845.
[13] A. Köhl, D. Stammer, Optimal observations for variational data assimilation, J. Phys. Oceanogr. 34 (2004) 529–542.
[14] A. Gnanadesikan, K.W. Dixon, S.M. Griffies, V. Balaji, M. Barreiro, J.A. Beesley, W.F. Cooke, T.L. Delworth, R. Gerdes, M.J. Harrison, I.M. Held, W.J. Hurlin, H.-C. Lee, Z. Liang, G. Nong, R.C. Pacanowski, A. Rosati, J. Russell, B.L. Samuels, Q. Song, M.J. Spelman, R.J. Stouffer, C.O. Sweeney, G. Vecchi, M. Winton, A.T. Wittenberg, F. Zeng, R. Zhang, J.P. Dunne, GFDL's CM2 global coupled climate models. Part II: The baseline ocean simulation, J. Climate 19 (2006) 675–697.

[15] D. Menemenlis, I. Fukumori, T. Lee, Atlantic to Mediterranean sea level difference driven by winds near Gibraltar Strait, J. Phys. Oceanogr. 37 (2007) 359–376.
[16] R. Sadourny, A. Arakawa, Y. Mintz, Integration of the nondivergent barotropic vorticity equation with an icosahedral-hexagonal grid for the sphere, Mon. Weather Rev. 96 (1968) 351–356.
[17] K.W. Morton, P.L. Roe, Vorticity-preserving Lax–Wendroff-type schemes for the system wave equation, SIAM J. Sci. Comput. 23 (2001) 170–192.
[18] T.D. Ringler, D.A. Randall, A potential enstrophy and energy conserving numerical scheme for solution of the shallow-water equations on a geodesic grid, Mon. Weather Rev. 130 (2002) 1397–1410.
[19] T.D. Ringler, D.A. Randall, The ZM grid: an alternative to the Z grid, Mon. Weather Rev. 130 (2002) 1411–1422.
[20] L. Bonaventura, T. Ringler, Analysis of discrete shallow-water models on geodesic delauney grids with C-type staggering, Mon. Weather Rev. 133 (2005) 2351–2373.
[21] M. Sommer, P. Névir, A conservative scheme for the shallow-water system on a staggered geodesic grid based on Nambu representation, Quart. J. Roy. Meteor. Soc. 135 (2009) 485–494.
[22] R. Salmon, L.D. Talley, Generalizations of Arakawa's Jacobian, J. Comput. Phys. 83 (1989) 247–259.
[23] B. Perot, Conservation properties of unstructured staggered mesh schemes, J. Comput. Phys. 159 (2000) 58–89.
[24] R. Salmon, A general method for conserving energy and potential enstrophy in shallow-water models, J. Atmos. Sci. 64 (2007) 515–531.
[25] R. Salmon, A shallow water model conserving energy and potential enstrophy in the presence of boundaries, J. Mar. Res. 67 (2009) 1–36.
[26] A. Arakawa, Computational design for long-term numerical integration of the equations of fluid motion: two-dimensional incompressible flow. Part I, J. Comput. Phys. 1 (1966) 119–143.
[27] G.S. Ketefian, Development and Testing of a 2-D Potential Enstrophy Conserving Ocean Model and a 3-D Potential Enstrophy Conserving, Nonhydrostatic, Compressible Atmospheric Model, Ph.D. Dissertation, Stanford University, December 2006. <http://www.stanford.edu/group/efmh/gsk/ketefian_thesis.pdf>.
[28] F. Mesinger, Horizontal advection schemes of a staggered grid – an enstrophy and energy-conserving model, Mon. Weather Rev. 109 (1981) 467–478.